POLITECNICO
MILANO 1863

Politecnico di Milano

Department of Civil and Environmental Engineering

Master's degree in Ingegneria per l'Ambiente e il Territorio
Environmental and Land Planning Engineering

Quantification of the spatio-temporal variability of ozone damage on winter wheat productivity in northern Italy using ERA5 reanalysis data

Lorenzo Barzon
10659882

Academic year
2023/24

Supervisor
Prof. **Giovanni Lonati**

Co-Supervisor
Prof. **Paola Crippa**

Acknowledgement

I would like to express my deep gratitude to all the people who allowed me to get this far and who contributed to the realization of this thesis.

First, I would like to thank my family for supporting me throughout my degree, both psychologically and financially.

I want to thank Federico Cucci for accompanying me on this journey from the beginning and for never leaving me alone.

I then thank Professor Lonati for giving me the opportunity to develop my thesis abroad and Professor Crippa for hosting me in her working group at the University of Notre Dame. Thanks also to all the members of the group for welcoming me with open arms.

I thank Professor Gerosa and Pierluigi Guaita for introducing me to the problem of ozone for vegetation and providing me with the necessary material to start developing this thesis.

Finally, I thank Dario Moccia for keeping me company both during the months spent in the United States and during the writing of my thesis.

Abstract

Tropospheric ozone is a potent oxidant, negatively affecting vegetation by causing physiological oxidative stress at the cellular level, reducing plant growth, and, at high concentrations, inducing visible foliar injuries (chlorosis and necrosis of leaves, premature aging of leaves) and, due to decreased photosynthesis, yield reductions in crops and horticultural species. Research has shown that wheat particularly sensitive to ozone damage. The biological effects of ozone are closely related to the actual dose absorbed through stomata of plants, and for this reason a stomatal flux-based metric, the Phytotoxic Ozone Dose above a detoxification threshold of 6 $nmol \cdot m^{-2} \cdot s^{-1}$, was used to estimate wheat yield reduction. The selected study domain is centered on the Lombardy region (Italy), characterized by complex topography. The study was aimed at estimating, through a dual-sink big-leaf model, the seasonal POD_6 for winter wheat for the period 2015-2019, using data of air temperature, relative humidity, precipitation, wind speed, global radiation and O_3 concentration retrieved from the ERA5 reanalysis dataset. After determining that the ozone data provided by ERA5 consistently underestimate O_3 concentrations compared to observed values, a Random Forest model was developed to obtain O_3 estimates using ERA5 meteorological parameters as inputs. The results obtained show a significant variability in POD_6 values between different years, with the average values for the entire domain varying between 1.67 and 2.43 $mmol \cdot m^{-2}$ PLA (Plant Leaf Area), corresponding to a reduction in yield of 6.4% and 9.2% respectively. These differences can be explained by analyzing the values of meteorological parameters year by year.

L'ozono troposferico è un potente ossidante, che influisce negativamente sulla vegetazione provocando uno stress ossidativo fisiologico a livello cellulare, riducendo la crescita delle piante e, ad alte concentrazioni, inducendo lesioni fogliari visibili (clorosi e necrosi delle foglie, invecchiamento precoce delle foglie) e, a causa diminuzione della fotosintesi, riduzione della resa delle colture e delle specie orticole. La ricerca ha dimostrato che il grano è particolarmente sensibile ai danni dell'ozono. Gli effetti biologici dell'ozono sono strettamente correlati alla dose effettiva assorbita attraverso gli stomi delle piante, e per questo motivo è stato deciso di utilizzare una metrica basata sul flusso stomatico, la dose di ozono fitotossico (POD) al di sopra di una soglia di disintossicazione di 6 $nmol \cdot m^{-2} \cdot s^{-1}$, per stimare la riduzione della resa del grano. L'area di studio selezionata è centrata sulla regione Lombardia (Italia), caratterizzata da una topografia complessa. Lo studio è stato finalizzato a stimare, attraverso un "dual-sink big-leaf model", il POD_6 stagionale del grano invernale per il periodo 2015-2019, utilizzando i dati di temperatura dell'aria, umidità relativa, precipitazione, velocità del vento, radiazione globale e concentrazione di O_3 del set di dati di rianalisi ERA5. Dopo aver constatato che i dati di ozono forniti da ERA5 sottostimano costantemente le concentrazioni di ozono rispetto ai valori osservati, è stato sviluppato un modello "Random Forest" per ottenere stime di O_3 utilizzando i parametri meteorologici di ERA5 come input. I risultati ottenuti mostrano una significativa variabilità dei valori di POD_6 tra gli anni considerati nello studio, con valori medi per l'intero dominio che variano tra 1,67 e 2,43 $mmol \cdot m^{-2}$ PLA (Plant Leaf Area), corrispondenti ad una riduzione della resa rispettivamente del 6,4% e del 9,2%. Queste differenze possono essere spiegate analizzando i valori dei parametri meteorologici anno per anno.

Table of Contents

List of Figures

List of Tables

1. Introduction

1.1 - Effects of Ozone on Vegetation

Ozone (O_3) is a pale blue gas with a pungent odor, toxic to living organisms, and unstable in nature. At ground level (and more in general, in the troposphere), O_3 forms mainly through photochemical reactions between nitrogen oxides (NO_X), volatile organic compounds (VOCs) and methane (Monks et al., 2014), processes favored by high temperatures and solar radiation. This makes ozone a secondary pollutant, with its precursors generated largely by industrial combustion and processes that use or produce volatile chemicals, such as solvents and fuels.
Ozone is removed from the troposphere through chemical destruction in the atmosphere and deposition on surfaces, including vegetation (Schultz et al., 2017). Local O_3 pollution levels and its atmospheric lifetime vary depending on concentrations of precursor molecules from local and long-range sources, as well as meteorological factors like radiation, temperature, and humidity (Lefohn et al., 2018). As a result, changes in weather conditions can significantly affect ozone concentrations near ground level (Coates et al., 2016; Cox and Chu, 1996).

Ozone pollution is a significant concern for vegetation, with its damaging effects on crop yields, food security, and ecosystem health well-documented. Surface O_3 levels have risen dramatically (by approximately 60–100%) since the industrial revolution (Vingarzan, 2004; Sitch et al., 2007), driven by increased emissions of CH_4, VOCs, and NO_X. Changes in meteorological conditions, such as rising temperatures, exacerbate the problem by promoting ozone formation. This rise in tropospheric O_3 is a growing concern for global crop yields, with negative impacts expected to persist and pressure food security (Mills et al., 2018; Ainsworth et al., 2020). Mitigating these effects by reducing precursor emissions and developing ozone-tolerant crop varieties is essential, especially as climate change exacerbates the problem. Ozone has been a major concern for European vegetation since the 1970s (Guderian, 1985).

Tropospheric O_3 is a potent oxidant, negatively affecting vegetation by causing physiological oxidative stress at the cellular level (Jolivet et al., 2016), reducing plant growth, and, at high concentrations, inducing visible foliar injuries (chlorosis and necrosis of leaves, premature aging of leaves) and, due to decreased photosynthesis, yield reductions in crops and horticultural species (Avnery et al., 2011; Emberson et al., 2018). These detrimental effects render O_3 the most hazardous pollutant for crop yields (Emberson et al., 2018).
When present in high concentrations in the proximity of crops, ozone enters plant leaves through stomatal pores during gas exchange processes. Once inside the leaf, ozone, being one of the most reactive oxidants known (Audran et al., 2018), rapidly dissolves in the aqueous apoplast (the intercellular space filled with fluid) where it generates reactive oxygen species (ROS, Agathokleous et al. 2020; Foyer et al. 2020), including superoxide (O_2^-), singlet oxygen ($^1[O_2]$), hydroperoxide (O_2H), and hydroxyl radicals ($OH^\bullet$). These ROS disrupt cellular homeostasis, damaging cell membranes, proteins, and DNA (by inducing gene alterations).
The primary mechanism of ozone damage starts with its reaction with the cell walls of leaf mesophyll cells. ROS produced from ozone exposure can cause lipid peroxidation, leading to the breakdown of cell membranes. This, in turn, impairs the plant's ability to maintain water and nutrient balance, triggering a series of physiological responses aimed at repairing damage. However, these defense responses, which include the activation of antioxidant systems such as ascorbic acid (AA) and glutathione, are energy-intensive and lead to reduced photosynthetic efficiency.

As reported by Goumenaki et al. (2021), analyzing the scientific literature relating to plant physiological responses it can be deduced that ozone tolerance in plants is primarily governed by the composition of the cell wall matrix surrounding leaf mesophyll cells, particularly the levels, regeneration rate, and redox status of ascorbic acid (AA) in the apoplast (Sanmartin et al. 2003; Yendrek et al. 2015). AA helps mitigate ozone-induced oxidative stress by quenching ROS and regulating defense-related gene expression (Noctor et al. 2018). The dynamics of AA catabolism and its transfer from the cytosol are critical for determining plant responses to ozone (Barnes et al. 2002; Vainonen and Kangasjärvi 2015), with genetic studies identifying these traits as key for crop tolerance (Frei et al. 2010; Feng et al. 2010). Ascorbate levels are influenced by biosynthesis, recycling, degradation, and transport within cells, and environmental factors like light directly regulate these pathways (Foyer et al. 2020; Ntagkas et al. 2018). Several studies have shown a correlation between higher apoplastic AA levels and increased O_3 tolerance (e.g. Turcsànyi et al. 2000; Padu et al. 2005). Manipulation of AA content and redox status through transgenic methods has further supported its role in O_3 defense (Sanmartin et al. 2003; Ueda et al. 2015). Rather than just the AA content, it is likely the regulation of AA in the apoplast that modulates responses to ozone-induced oxidative stress (Zechmann 2018).

Ozone-induced ROS also interfere with photosynthesis by damaging chloroplasts, the organelles responsible for converting light energy into chemical energy. This damage leads to a reduction in chlorophyll content, impairing the plant's ability to absorb light and produce carbohydrates. As photosynthesis declines, plants experience a reduction in carbon fixation, leading to slower growth rates and lower biomass accumulation (Gillespie et al. 2015). The ROS accumulation also accelerates leaf senescence, further reducing the plant's ability to carry out photosynthesis over time. In addition to directly affecting cellular structures, ozone exposure triggers shift in gene expression. Plants respond to oxidative stress by upregulating genes involved in repair and defense mechanisms, including those associated with the production of antioxidants and proteins that protect cellular structures. However, this shift comes at a cost, diverting resources from growth and reproduction to stress mitigation. Prolonged exposure to high O_3 concentrations leads to chronic stress, which can result in reduced flowering, seed production, and overall crop yield and quality.

One of the hallmark effects of ozone exposure is the phenomenon known as "stomatal sluggishness". Normally, stomata respond to environmental factors like light, humidity, and CO_2 levels to regulate gas exchange and water loss. However, ozone exposure alters the stomatal response, reducing the plant's ability to close stomata efficiently. This condition increases ozone uptake during the day and reduces water-use efficiency (Emberson, 2020), making plants more vulnerable to drought and other environmental stressors. Stomatal sluggishness can persist through the night (Hoshika et al. 2016; Grulke and Heath 2020), exacerbating water loss and further impairing plant health.

Research has shown that wheat (Feng et al., 2009; Mills et al., 2007) and soybean (Osborne et al., 2016; Broberg et al., 2020) are particularly sensitive to ozone damage. Field experiments worldwide (e.g., Singh et al., 2017; Hayes et al., 2020) have demonstrated significant yield reductions due to ozone exposure. Global analyses reveal that current ambient O_3 levels reduce wheat yields by approximately 7% (conservative estimates), with similar reductions in other sensitive crops (Tai et al., 2021). In regions with high ozone pollution, grain yield improvements have been observed when ambient ozone is filtered (Pleijel et al., 2018), providing direct evidence of the pollutant's harmful effects on vegetation.

The impact of O_3 on agriculture is compounded by interactions with other environmental factors, such as temperature and precipitation. While these or other variables (e.g., the carbon fertilization effect, CFE) may affect crop growth, ozone exposure consistently leads to negative outcomes (Shindell, 2016), including chlorosis and necrosis, stunted growth, and diminished yields. Moreover, different crop varieties show varying responses to ozone exposure (Biswas et al., 2009; Osborne et al., 2016), introducing uncertainty in assessing the long-term impacts of O_3 pollution on food security.

As suggested by reports published by ICP Vegetation on the effects of O_3 on vegetation, including food security (Mills et al., 2011), carbon sequestration (Harmens & Mills, 2012), ecosystem services and biodiversity (Mills et al., 2013), ozone damage is not limited to crops but extends to ecosystems, including forests, grasslands, and horticultural species (Avnery et al., 2011). Long-term exposure to high O_3 concentrations leads to shifts in gene expression and cellular metabolism in plants, resulting in reduced growth, impaired carbon allocation between roots and shoots, and decreased productivity. These changes affect ecosystem services, such as carbon sequestration, biodiversity, and forage quality for livestock. The negative impacts on water-use efficiency due to stomatal sluggishness also increase the vulnerability of plants to abiotic (e.g., droughts and frost) and biotic (e.g., diseases and pests) stresses.

1.2 - Metric for Damage Assessment

As reported by Guaita et al. (2023), in recent decades numerous studies have aimed to establish empirical relationships between the levels of exposure to ozone and the biological damage they cause to plants (Emberson, 2020). Particularly noteworthy are the contributions from North America's National Crop Loss Assessment Network (NCLAN, Heck et al., 1988) and Europe's ICP-Vegetation program (Long-Range Transboundary Air Pollution Convention, 2017). These early efforts helped define O_3 dose-response relationships between ozone concentrations and yield reduction using indices based on cumulative exposure, such as M7 (mean 7-hour daytime concentration), M12 (mean 12-hour daytime concentration) and AOT40 (Accumulated Ozone over a Threshold of 40 ppb). However, subsequent research has shown that the biological effects of O_3 are more closely related to the actual dose absorbed through stomata (the O_3 flux), rather than the mere exposure to atmospheric ozone concentrations (Emberson et al., 2000; Mills et al., 2011).

Exposure indices based on the ozone concentration above the leaf surface such as AOT40 are still widely used because they provide a straightforward way to estimate yield losses or growth reductions for a variety of species (Lesser et al., 1990; Mills et al., 2007). An example of this is the European Union, which currently assesses the impacts of O_3 on vegetation using the AOT40 indicator, which measures accumulated O_3 concentrations above 40 ppb from May to July.
These indices rely solely on atmospheric O_3 concentration data, which are readily available from monitoring networks, models, and satellites. As a result, metrics like AOT40 can be applied in situations where meteorological or vegetation-specific data needed for calculating flux-based metrics are lacking or in regions where climatic or water restrictions to stomatal O_3 flux are not expected. However, this metric does not account for plant stress caused by hydrological conditions, such as water deficits, that commonly occur during ozone episodes. The failure to consider stomatal behavior and environmental conditions limits the accuracy of the AOT40 metric for developing precise dose-response relationships, leading to uncertainty in estimating O_3 impacts on agricultural yields and the economic analysis of such impacts.

To address these limitations, a stomatal flux-based metric, POD_Y (Emberson et al., 2000), was proposed in the early 2000s by the expert group IPC-Vegetation, working under the Air Convention and the Working Group on Effects (WGE). Phytotoxic Ozone Dose above a threshold Y, defined by Mills et al. (2011) as the accumulated stomatal O_3 flux above the detoxification threshold Y during a specified time or growth period, considers the amount of O_3 absorbed by the plant through leaf pores, reflecting how environmental factors like temperature, humidity, soil moisture, and plant phenology influence stomatal behavior. When exposed to hot and dry conditions, for example, plants tend to close their stomata to reduce water loss, thereby reducing O_3 uptake and this, consequently, mitigates potential damage. The DO_3SE (Deposition of O_3 for Stomatal Exchange) model was developed to estimate stomatal flux by accounting for such variables and is used to calculate species-specific POD_Y values (Büker et al., 2012; Emberson et al., 2000, 2001, 2007).

Various studies suggest that the relationship between ozone effects and exposure improves when considering the plant's defense mechanisms. A portion of the absorbed O_3 is detoxified within the plant, mitigating its overall impact (Mills et al., 2011). This detoxification capacity, which varies by species, is accounted for through an hourly Y flux cut-off in POD_Y calculations. The detoxification threshold Y for instantaneous stomatal ozone flux differs among species, with values of 1 $nmol \cdot m^{-2} \cdot s^{-1}$ for forest trees and 6 $nmol \cdot m^{-2} \cdot s^{-1}$ for winter wheat (LRTAP Convention, 2017). Y statistically represents the plant's O_3 detoxification capacity based on antioxidants such as ascorbate (Ditzengremel et al., 2008). Feng et al. (2016) found that variations in O_3 sensitivity among wheat genotypes were related to differences in antioxidant defense capacity.

Although POD_Y and similar metrics require complex inputs such as water vapor pressure deficit (VPD), stomatal conductance, deposition velocity, and other environmental factors, making them more challenging to compute (Emberson et al., 2000; Mills et al., 2011), growing evidence indicates that O_3 flux-based metrics are more accurate than concentration-based ones like AOT40 for predicting O_3 effects on vegetation. Stomatal O_3 flux has been shown to correlate more strongly with plant damage than ambient O_3 concentration (Mills et al., 2011; Paoletti et al., 2019). For instance, Hoshika et al. (2018a) found that visible O_3 injury in poplar leaves was better explained by POD_Y, and further research demonstrated that including water availability in stomatal O_3 flux calculations improved the accuracy of O_3 exposure assessments for oak species (Hoshika et al., 2018b). Similarly, epidemiological studies on southern European trees found POD_Y to be a better predictor of O_3 damage than AOT40 (Sicard et al., 2020).

Flux-based dose-response relationships have proven more robust than those based solely on concentration (UNECE, 2017), as they account for factors such as the vertical distribution of O_3 within the crop canopy and the phenology and physiology of plants, which depend on climate and meteorological conditions (Mills et al., 2018). Stomatal conductance, for example, is tightly regulated by soil water availability, and dry, sunny conditions that favor high O_3 concentrations also lead to stomatal closure, reducing O_3 flux and limiting damage (Emberson et al., 2000). Furthermore, the timing of O_3 exposure within the plant's growth cycle also plays a critical role, as crops exhibit varying sensitivities to O_3-induced cellular damage and altered carbon allocation depending on the growth stage (Heath and Taylor, 1997). The inclusion of these physiological and environmental factors in flux-based metrics, such as POD_Y, makes them more effective in predicting O_3 impacts on plant health.

Large-scale studies have demonstrated the advantages of using POD_Y in risk assessments, particularly for crops like wheat, where POD_Y has shown a stronger correlation between observed effects on grain yield and O_3 dose (Pleijel et al., 2007). The development of these flux-based metrics has significantly influenced European emission reduction strategies aimed at improving air quality by incorporating critical levels (CLs) for O_3, which mark thresholds above which vegetation damage is expected (LRTAP Convention, 2017; Mills et al., 2011). By synthesizing data from O_3 flux-based dose-response relationships (DRRs) derived from field experiments, CLs have been established to predict the onset of O_3 damage (LRTAP Convention, 2017). These CLs, formulated by the United Nations Convention on Long Range Transboundary Air Pollution, have become essential policy tools for identifying areas in Europe where O_3 levels exceed critical thresholds, thus guiding emission reduction strategies across the region to mitigate the adverse effects of O_3 on vegetation. The critical level for winter wheat, as identified by the LRTAP Convention (2017), is defined as an accumulated ozone flux of 1.3 mmol $O_3 \cdot m^{-2}$ PLA, which corresponds to a 5% loss in grain yield.

1.3 - Study Objectives

Following Guaita et al. (2023), the selected study domain encompasses the Lombardy region in northern Italy, with boundaries at 8.2°W to 11.55°E and 44.2°S to 47°N. Lombardy has a temperate climate, ranging from continental subhumid to suboceanic axeric (Botti, 2018), and is characterized by complex topography. The region's surface area is nearly equally divided between plains, which cover approximately 47% of the territory, and mountainous areas, which represent around 40%. The remaining 12% is composed of hilly terrain. Lombardy has an average elevation of 279 meters above sea level (asl) and reaches a maximum elevation of 4020 meters asl.
Agricultural activity is predominantly located in the Po Valley, in the center of the domain and in valley floors, while forests dominate the highland areas up to approximately 1800 meters asl. The primary crops grown in the region include cereals, such as maize and wheat, as well as various vegetables. During the 2018–2022 period, an average of 16.5% of Lombardy's cropland dedicated to cereals was cultivated with winter wheat (*Triticum aestivum*), making it the second most widely grown cereal crop after maize (ISTAT, 2023).

The estimation of O_3 deposition fluxes on vegetation involves applying a resistance analogy to describe the various deposition pathways. Models for calculating ozone fluxes typically incorporate dry deposition models, which were first developed in the 1980s to estimate the deposition velocities of different chemical compounds, driven by concerns about acid rain (e.g., Regional Acid Deposition Model (RADM) - Wesely, 1989; Acid Deposition and Oxidant Model (ADOM) - Venkatram et al., 1988). These early models relied on prognostic meteorological data (Walcek et al., 1986) with coarse spatial resolutions (Sheih et al., 1986; Wesely & Lesht, 1989) ranging from 20×20 km^2 to 120×120 km^2 and temporal resolutions from 1 to 6 hours. Baldocchi et al. (1987) introduced a big-leaf model to assess dry deposition on vegetation, which was later used by Hicks et al. (1987) to estimate deposition of various compounds on a small network of vegetation sites.

A key development in ozone risk assessment occurred with the work of Emberson et al. (2000), who produced the first continental map of stomatal O_3 fluxes for wheat and beech across Europe using a single big-leaf dry deposition scheme. This model utilized input data from the European Monitoring and Evaluation Program (EMEP), with a 6-hour temporal resolution and a spatial resolution of 150 × 150 km^2. Subsequent studies by Simpson et al. (2007), Mills et al. (2011), and Tang et al. (2014) improved upon these models by producing maps with higher spatial resolutions (50 km and 40 km).

Advances in computational power and the availability of higher-resolution meteorological data for Chemical Transport Models (CTMs) enabled the generation of regional maps of Phytotoxic Ozone Dose with finer spatial resolutions, such as 6×6 km^2 (De Marco et al., 2016) and 5×5 km^2 (Watanabe et al., 2016; Wang et al., 2022). Other examples include continental POD maps for forests produced by Anav et al. (2016) at a resolution of 12×12 km^2 for Europe and by De Marco et al. (2020) at a resolution of 8×8 km^2 for Asia.
Additionally, Nussbaum et al. (2003) utilized ground-based meteorological and O_3 data to calculate ozone stomatal flux for arable crops and pastures, with a spatial resolution of 1×1 km^2 and a temporal resolution of 3 hours. In a recent study, Guaita et al. (2023) estimated O_3 yield loss risk for winter wheat in Lombardy during the 2017 growing season by spatializing meteorological and ozone concentration data from regional networks. They applied the POD_6 metric using a dual-sink big-leaf model and analyzed how different spatial and temporal resolutions (ranging from 1×1 to 50×50 km^2, and from 1-hour to 6-hour intervals) affect O_3 risk estimates in a region with complex topography, aiming to identify the coarsest resolution capable of detecting ozone damage hotspots.

Following Guaita et al. (2023), this study focuses on estimating ozone damage to winter wheat, a model crop for O_3 risk assessment at the European level, with a robust experimental foundation for specific O_3 dose-response functions (Pleijel et al., 2022). The primary objectives of this research are:

- To estimate the risk of O_3-induced yield loss for winter wheat in the Lombardy region (Italy) using meteorological data from the ERA5 reanalysis product, with metrics calculated through a dual-sink big-leaf model

- To assess if and how different spatial resolutions (~30×30 km^2 and 1×1 km^2) influence the estimate of ozone damage, both in terms of reduction of agricultural yield and in terms of economic loss

- To analyze the impact of meteorological conditions on O_3 uptake by winter wheat by assessing ozone damage during the 2015–2019 growing seasons

2. Input Data

Calculating ozone fluxes, which necessitates the use of a resistance analogy to describe deposition pathways, and estimating the biological damage to plants caused by ozone uptake through stomata involve the acquisition of several input parameters. These parameters include atmospheric and environmental variables such as air temperature, wind speed, relative humidity, incoming short-wave radiation, and precipitation. Additionally, ozone concentrations are required, as these directly influence the amount of ozone that plants are exposed to and subsequently absorb.
Soil characteristics, specifically in terms of soil field capacity and wilting point, are also essential inputs. Field capacity refers to the amount of water content retained in the soil after excess water has drained away, and the soil has become saturated. The wilting point represents the minimal soil moisture level at which plants can no longer extract water, which is crucial for understanding the water stress conditions of plants and their subsequent ozone uptake rates.
Furthermore, land use data play a critical role in these calculations, as they provide information on the distribution of vegetation in the study domain. Specifically, knowing the fraction of cropland within each grid node is necessary to assess the potential exposure and response of crops to ozone, allowing for more accurate modeling of biological impacts of ozone on vegetation.

To ensure the quality of the reanalysis data, a validation approach was employed, involving a direct comparison of the model-generated values with measurements obtained from specific monitoring stations located within the study domain. These monitoring stations, distributed throughout the area of interest, provide high-quality observational data that serve as a benchmark for evaluating the reliability and accuracy of the reanalysis output. By comparing the modeled data with actual measurements, it is possible to assess the performance of the reanalysis models in capturing key atmospheric and land-surface parameters. This comparison allows for the identification of any biases or discrepancies in the model outputs, which can then be addressed through model adjustments or calibration.
For the selection of the measuring stations to be considered in the comparison with the reanalysis data, it was decided to set a minimum completeness threshold equal to 80% of the data available on an annual basis.

2.1 - Data from Reanalysis Products

Climate reanalyses integrate historical observations with models to produce consistent time series of various climate variables. These reanalyses are among the most widely used datasets in the geophysical sciences, offering a comprehensive depiction of the observed climate and its evolution over recent decades. The data are provided on three-dimensional grids at sub-daily intervals, ensuring detailed temporal and spatial resolution.

A climate reanalysis offers a numerical description of the recent climate by merging models with observations. It includes estimates of atmospheric parameters, such as air temperature, pressure, and wind speed at various altitudes, along with surface parameters like rainfall, soil moisture content, ocean-wave height, and sea-surface temperature. These estimates are produced for all locations on Earth and cover extensive temporal periods, often extending back several decades or more.

Reanalysis involves the combination of model data with observations collected globally, creating a consistent and comprehensive dataset using the principles of physics. This approach, known as data assimilation, is based on the methodology employed by numerical weather prediction centers, where every so many hours (12 hours at ECMWF) a previous forecast is optimally combined with newly available observations to produce a new best estimate of the state of the atmosphere, referred to as an analysis, from which an updated and improved forecast is issued. While reanalysis follows the same principles, it operates at a reduced resolution to accommodate the provision of datasets spanning several decades in the past. Unlike operational forecasts, reanalysis does not have the constraint of issuing timely forecasts, allowing for more extensive collection and incorporation of observations, including reprocessed historical data, which enhances the overall quality of the reanalysis product.

The European Centre for Medium-Range Weather Forecasts (ECMWF) regularly utilizes its advanced forecast models and data assimilation systems to “reanalyse” archived observations, thereby generating global datasets that describe the recent history of the atmosphere, land surface, and oceans. The reanalysis process requires specific methodological developments to ensure the highest possible temporal consistency, which can be compromised by biases in models and observations, as well as by the continuously evolving observational systems.
Current research efforts at ECMWF are focused on developing consistent reanalyses of the coupled climate system. This includes the atmosphere, land surface, ocean, sea ice, and the carbon cycle, with datasets extending back a century or more. Another key area of research involves improving the management of systematic model biases, which can significantly affect the accuracy of reanalysis products. Furthermore, this work involves the incorporation, preparation, and evaluation of newly available climate observations, ranging from early in-situ surface measurements made by meteorological observers to modern high-resolution satellite datasets. New generations of reanalyses also benefit from improved versions of existing observations, including the latest available reprocessed satellite records provided by space agencies.

- ERA5

ERA5 represents the latest climate reanalysis product developed by ECMWF, providing hourly data on numerous atmospheric, land-surface, and sea-state parameters, along with estimates of uncertainty. The ERA5 data, accessible through the Climate Data Store, are provided on regular latitude-longitude grids at a 0.25°×0.25° resolution. Atmospheric parameters (including ozone concentration values) are available on 137 model levels and 37 interpolated pressure levels. The ERA5 dataset extends back to 1940 and is continually updated, with data available up to five days behind real-time, providing a comprehensive dataset spanning the last eight decades. This dataset is the fifth generation of ECMWF's atmospheric reanalysis products for global climate and weather, following the progression from the FGGE reanalysis of the 1980s to the ERA-15, ERA-40, and most recently, ERA-Interim reanalysis.

The ERA5 dataset comprises a single high-resolution realization (hourly, 31 km – one-quarter of the spatial resolution of the operational model), referred to as “reanalysis” or “HRES”, and a lower-resolution (62 km), ten-member ensemble, referred to as “ensemble” or “EDA”. While the ensemble is primarily used in the data assimilation procedure, it also provides an estimate of relative, random uncertainty as a by-product.

ERA5 is produced using four-dimensional variational (4D-Var) data assimilation and model forecasts within CY41R2 of ECMWF's Integrated Forecast System (IFS), featuring 137 hybrid sigma-pressure (model) levels in the vertical, extending up to a top level of 0.01 hPa. Atmospheric data are available on these model levels and are also interpolated to 37 pressure levels (consistent with those used in ERA-Interim), 16 potential temperature levels, and 1 potential vorticity level by FULL-POS (a software doing post-processing on different kind of vertical levels) in the IFS. Additionally, surface or single-level data are provided, encompassing two-dimensional parameters such as precipitation, 2-meter temperature, top-of-atmosphere radiation, and vertical integrals over the entire atmospheric depth. The IFS's atmospheric model is coupled with a land-surface (or soil) model (HTESSEL), which generates parameters including 2-meter temperature and soil temperatures, as well as an ocean wave model (WAM), whose parameters are also categorized as surface or single-level data.

Table 2.1 and *Table 2.2* report the parameters acquired from the ERA5 dataset needed to estimate the damage caused by ozone to vegetation, together with their description (as provided by ECMWF). Being interested in surface values for crop damage estimation, the ozone values downloaded from the ERA5 dataset on hybrid sigma-pressure levels are the data at model level 137 (the one closest to the Earth's surface).

Table 2.1 - ERA5 hourly data on single levels

Parameter	UoM	Description
10m u-component of wind	$m \cdot s^{-1}$	Eastward component of the 10m wind. It is the horizontal speed of air moving towards the east, at a height of ten meters above the surface of the Earth, in meters per second.
10m v-component of wind	$m \cdot s^{-1}$	Northward component of the 10m wind. It is the horizontal speed of air moving towards the north, at a height of ten meters above the surface of the Earth, in meters per second.
2m dew point temperature	K	Temperature to which the air, at 2 meters above the surface of the Earth, would have to be cooled for saturation to occur. It is a measure of the humidity of the air. 2m dew point temperature is calculated by interpolating between the lowest model level and the Earth's surface, taking account of the atmospheric conditions.
2m temperature	K	Temperature of air at 2m above the surface of land, sea or inland waters. 2m temperature is calculated by interpolating between the lowest model level and the Earth's surface, taking account of the atmospheric conditions.
Surface pressure	Pa	Pressure (force per unit area) of the atmosphere at the surface of land, sea and inland water. It is a measure of the weight of all the air in a column vertically above a point on the Earth's surface.
Surface solar radiation downwards	$J \cdot m^{-2}$	Amount of solar (or shortwave) radiation that reaches a horizontal plane at the surface of the Earth. This parameter comprises both direct and diffuse solar radiation. Radiation from the Sun is partly reflected back to space by clouds and particles in the atmosphere (aerosols) and some of it is absorbed. The rest is incident on the Earth's surface (represented by this parameter). To a reasonably good approximation, this parameter is the model equivalent of what would be measured by a pyranometer (an instrument used for measuring solar radiation) at the surface. This parameter is accumulated over a particular time period which depends on the data extracted. For the reanalysis, the accumulation period is over the 1 hour ending at the validity date and time. The ECMWF convention for vertical fluxes is positive downwards.
Total precipitation	m	Accumulated liquid and frozen water, comprising rain and snow, that falls to the Earth's surface. It is the sum of large-scale precipitation and convective precipitation. Large-scale precipitation is generated by the cloud scheme in the ECMWF IFS. The cloud scheme represents the formation and dissipation of clouds and large-scale precipitation due to changes in atmospheric quantities (such as pressure, temperature and moisture) predicted directly by the IFS at spatial scales of the grid box or larger. Convective precipitation is generated by the convection scheme in the IFS, which represents convection at spatial scales smaller than the grid box. This parameter does not include fog, dew or the precipitation that evaporates in the atmosphere before it lands at the surface of the Earth. This parameter is accumulated over a particular time period which depends on the data extracted. For the reanalysis, the accumulation period is over the 1 hour ending at the validity date and time.

Table 2.2 - ERA5 hourly data on model levels

Parameter	UoM	Description
Ozone mass mixing ratio	$kg \cdot kg^{-1}$	Mass of ozone per kilogram of air. In the ECMWF IFS, there is a simplified representation of ozone chemistry (including representation of the chemistry which has caused the ozone hole). Ozone is also transported around in the atmosphere through the motion of air.

2.2 - Land Use

Land use data were obtained from the land cover classification map issued by Copernicus (ICDR, Louvain and Defourny, 2023), which is provided at a spatial resolution of 0.3×0.3 km^2. For consistency with the datasets for elevation, wilting point and field capacity, the land use data were rescaled to a resolution of 1×1 km^2.

The dataset offers global maps that categorize the land surface into 22 distinct classes, which are defined in accordance with the United Nations Food and Agriculture Organization's (UN FAO) Land Cover Classification System (LCCS). To ensure continuity, these land cover maps are aligned with the series of global annual land cover (LC) maps from the 1990s to 2015, developed under the European Space Agency (ESA) Climate Change Initiative (CCI).

The production of this dataset involved classifying the entire Medium Resolution Imaging Spectrometer (MERIS) Full and Reduced Resolution archive from 2003 to 2012 into a unique 10-year baseline LC map. This baseline was then adjusted retrospectively and prospectively (back- and up-dated) using change detection methodologies. Specifically, changes were detected from the Advanced Very-High-Resolution Radiometer (AVHRR) time series from 1992 to 1999, the SPOT-Vegetation (SPOT-VGT) time series from 1998 to 2012, and the PROBA-Vegetation (PROBA-V) and Sentinel-3 OLCI (S3 OLCI) time series from 2013 onward.

Each domain grid node within this dataset has been assigned a value ranging from 0 to 1 based on the percentage of cropland it contains, with a value of 1 indicating that the entire area within the grid node is occupied by cropland.

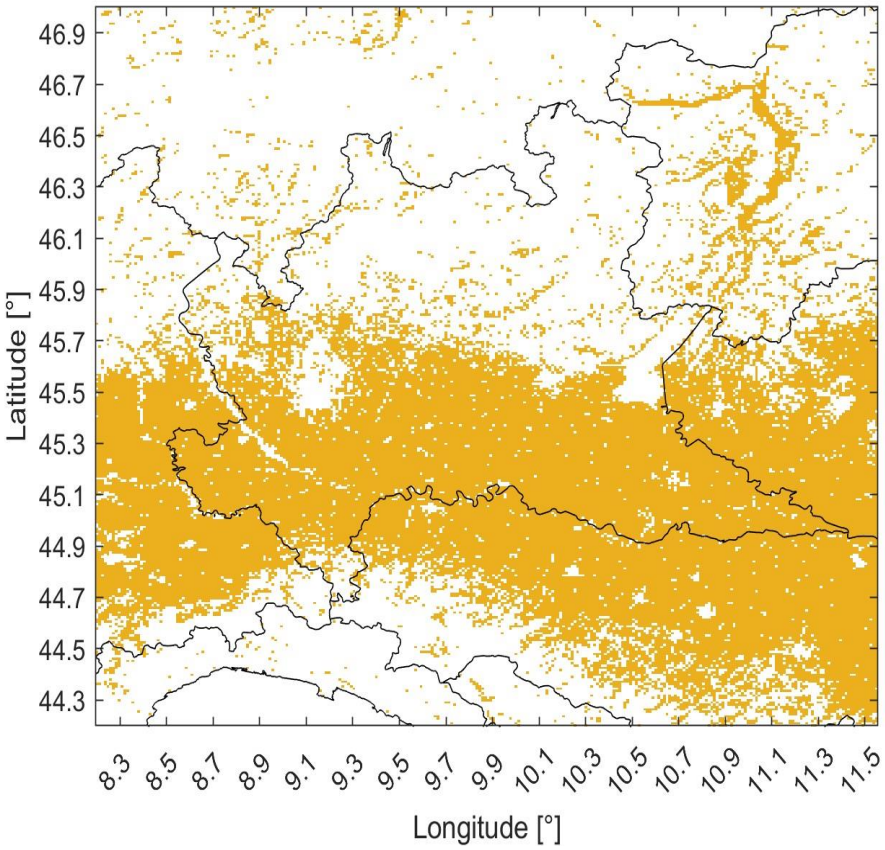

Figure 2.1 - Land use data for year 2017
(only the nodes with a fraction of cultivated land other than zero are represented)

2.3 - Field Capacity and Wilting Point

Soil field capacity and wilting point data were obtained from the EU-SoilHydroGrids version 1.0, a comprehensive dataset that provides high-resolution soil-related values at a 1×1 km^2 spatial resolution. The multilayered European Soil Hydraulic Database (EU-SoilHydroGrids ver1.0) was developed using European pedotransfer functions (EU-PTFs) as described by Tóth et al. (2015). These functions were derived from soil information sourced from SoilGrids250m and aggregated 1 km (Hengl et al., 2017) datasets.

The EU-SoilHydroGrids ver1.0 dataset covers a range of soil hydraulic parameters:

- Saturated water content
- Water content at field capacity and wilting point
- Saturated hydraulic conductivity
- Mualem-van Genuchten parameters for the description of moisture retention
- Unsaturated hydraulic conductivity curves

The development of the EU-PTFs (Tóth et al., 2015) was based on training data from the European Hydropedological Dataset (EU-HYDI; Weynants et al., 2013). EU-HYDI is an extensive collection comprising data from 29 institutions across 18 European countries and includes information on taxonomical, chemical, and physical soil properties from more than 18,000 soil samples. The pedotransfer functions were calibrated using soil data of 134 to 6,074 samples and validated on 57 to 2,357 samples, depending on the specific soil hydraulic property being assessed (Tóth et al., 2015).

SoilGrids provides the most detailed information on soil properties with complete continental coverage of Europe. This dataset incorporates soil taxonomical, physical, and chemical data across seven soil depths, recorded at a 250 m resolution (Hengl et al., 2017). The soil properties utilized for the calculation of soil hydraulic properties included: clay, silt, and sand content (mass %), organic carbon content (g kg^{-1}), bulk density (kg m^{-3}), pH in water and depth to bedrock (cm) measured at depths of 0, 5, 15, 30, 60, 100, and 200 cm. In accordance with the EU-PTFs used for calculations (Tóth et al., 2015), the first four depths (≤30 cm) are classified as topsoil, while the remaining depths are treated as subsoil.

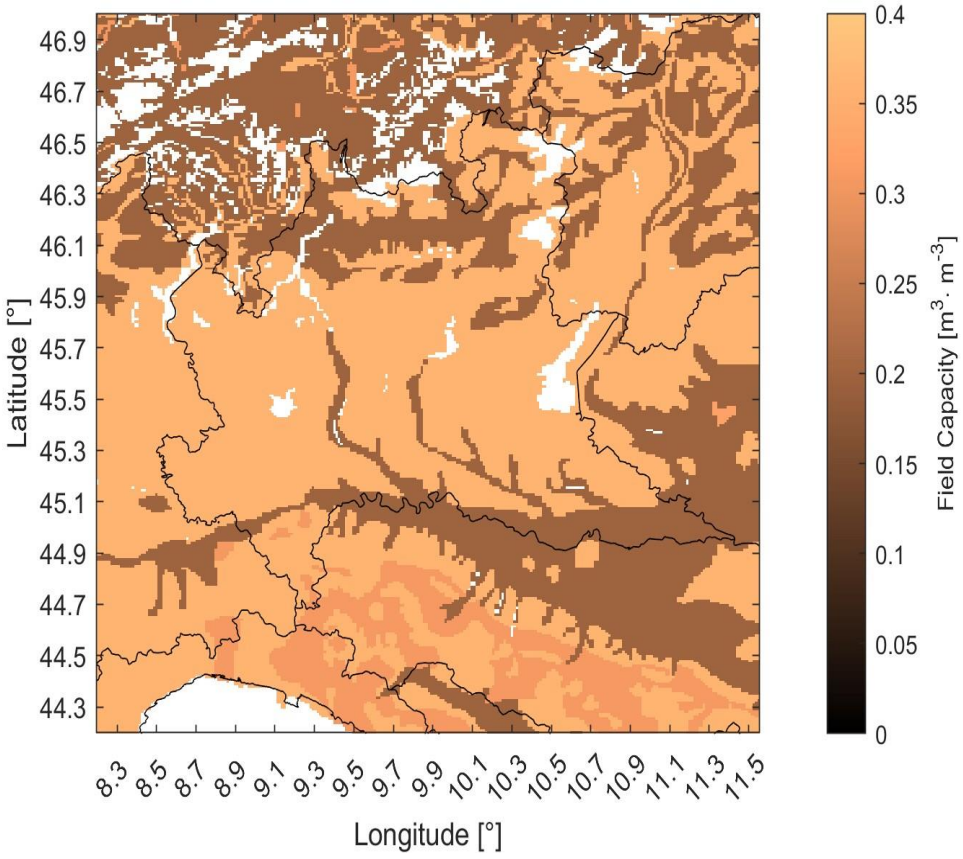

Figure 2.2 - Spatial distribution of soil field capacity data in the domain

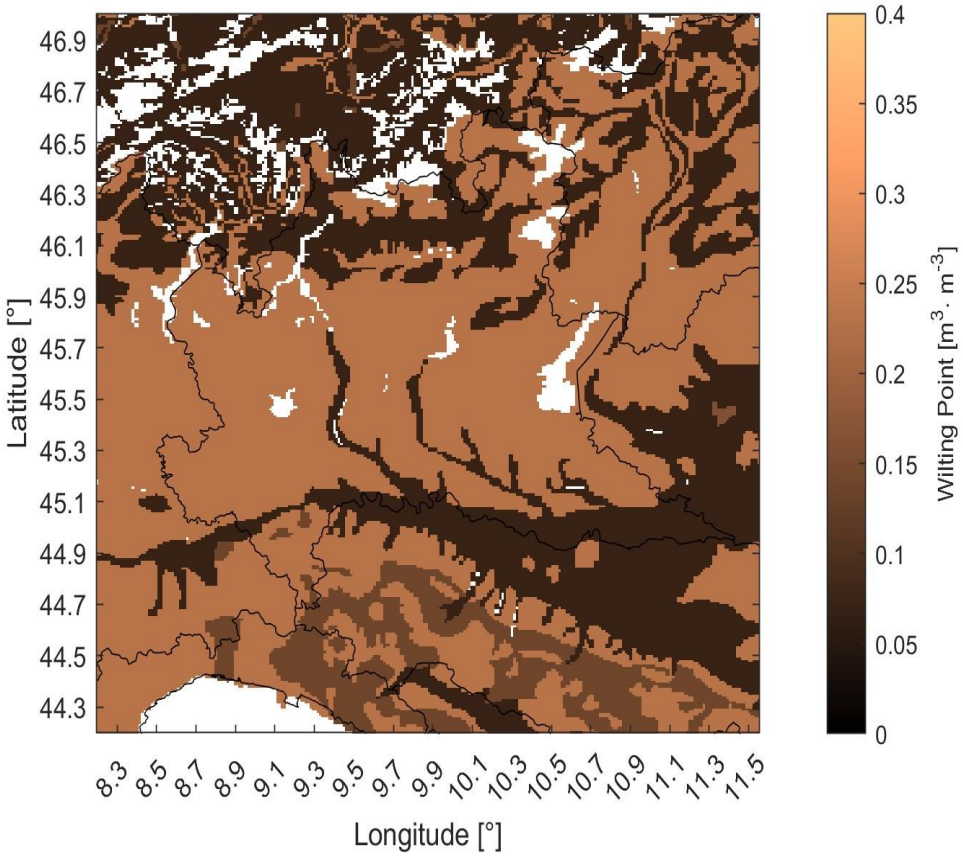

Figure 2.3 - Wilting point map obtained from EU-SoilHydroGrids ver1.0

2.4 - Elevation Data

GTOPO30 is a global Digital Elevation Model (DEM) characterized by a horizontal grid spacing of 30 arc seconds, which corresponds to approximately 1 kilometer at mid-latitude. The dataset was derived from a combination of raster and vector sources of topographic information.

The development of GTOPO30 was completed in late 1996, following a three-year collaborative effort spearheaded by the U.S. Geological Survey's Center for Earth Resources Observation and Science (EROS). The project received support, both in terms of funding and source data, from several organizations, including the National Aeronautics and Space Administration (NASA), the United Nations Environment Programme/Global Resource Information Database (UNEP/GRID), the U.S. Agency for International Development (USAID), the Instituto Nacional de Estadística y Geografía (INEGI) of Mexico, the Geographical Survey Institute (GSI) of Japan, Manaaki Whenua Landcare Research of New Zealand, and the Scientific Committee on Antarctic Research (SCAR).

GTOPO30 is a global dataset covering the full extent of latitude (from 90 degrees south to 90 degrees north) and the full extent of longitude (from 180 degrees west to 180 degrees east). The DEM is composed of 21,600 rows and 43,200 columns, with each grid cell measuring 30 arc seconds (0.008333 degrees) in both latitude and longitude. The horizontal coordinate system is based on decimal degrees of latitude and longitude, referenced to the WGS84 datum. The vertical measurements represent elevation in meters above mean sea level. In the dataset, ocean areas have been masked as "no data" and have been assigned a value of – 9999.

The GTOPO30 (Global 30 Arc-Second Elevation) dataset can be accessed through EarthExplorer, where users can search, preview, and download data under the Digital Elevation category.

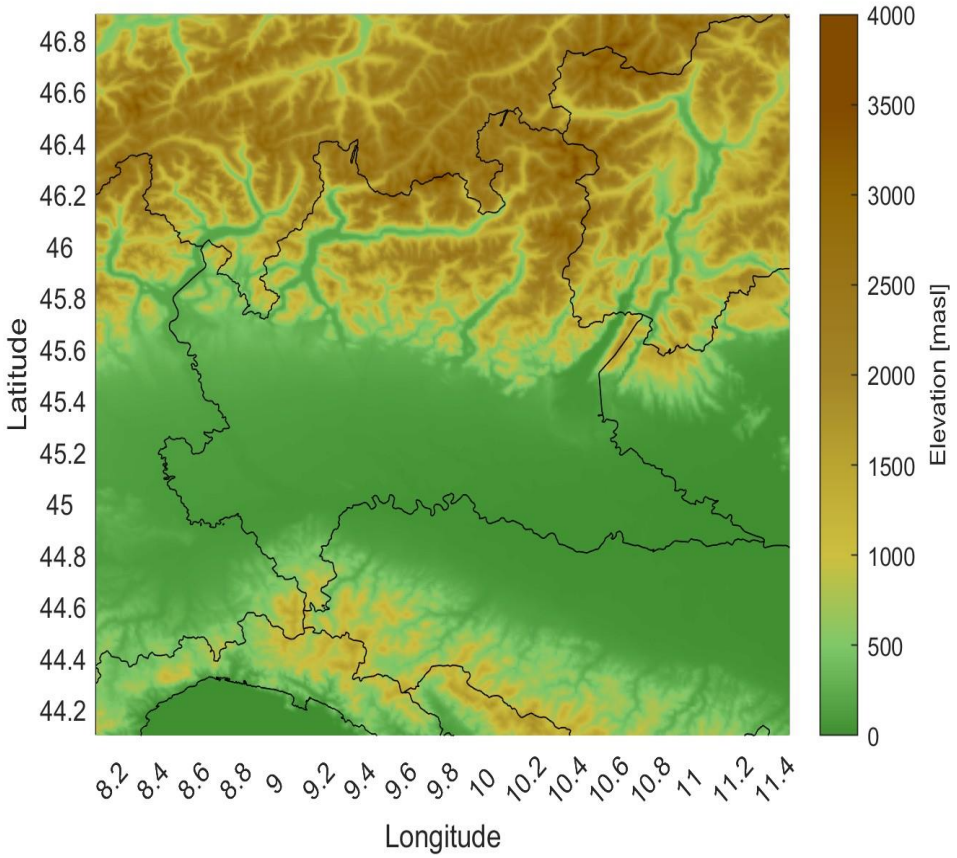

Figure 2.4 - DEM map at 1 km resolution

2.5 - Observed Meteorological Parameters

The observed data relating to temperature, wind speed, relative humidity, incident short-wave radiation and precipitation were retrieved from the ARPA (Regional Environmental Protection Agency) Lombardia sensor network. The station data collected by the Regional Meteorological Detection Network (Rete Regionale di Rilevamento Meteorologico) of ARPA Lombardia can be consulted and downloaded free of charge by accessing the "Data Access" ("Accesso ai dati") page of the ARPA Lombardia website.

The reason why it was decided to consider only the monitoring network of Lombardy (and not those of the other regions included in the domain) is that the data download operations, if performed manually, are very time-consuming. For example, in the ARPA Lombardia portal it is possible to simultaneously select a maximum of seven parameters, not necessarily from the same station, for a period not exceeding one year, while for requests over longer periods it is necessary to select only one sensor at a time (i.e. a parameter from a single station). On the other hand, when downloading data from ARPA Piemonte, it is possible to select a maximum of three stations or parameters per request.

To download the meteorological data from the sensors located in Lombardy, a package for the R software was used. The package, named “ARPALData” and developed by Maranzano & Algieri (2024), contains functions for the automatic retrieval, management and analysis of air quality and weather data from the open database of Lombardy Region. Data are collected by ARPA Lombardia through its ground monitoring network. Data quality (e.g. missing values, exported values, graphical mapping) has been checked involving members of the ARPA Lombardia's office for air quality control. The package makes available observations since 1989 (for weather) and 1968 (for air quality) and are updated with daily frequency by the regional agency.

Within the monitoring network there are sensors capable of measuring the following parameters:

- Cumulative precipitation (mm)
- Temperature (°C)
- Relative humidity (%)
- Global radiation (W/m^2)
- Wind speed (m/s)
- Wind direction (direction of origin in degrees clockwise from North)
- Hydrometric level (cm)
- Snow depth (cm)
- Wind speed and direction (m/s and degrees from North) for gusts

Wind speed and direction are measured at 3 meters height while all other variables are measured at 2 meters above the ground.

The sensors have a sub-hourly detection frequency (typically one measurement every 10 minutes), but it is also possible to download aggregated data. The temporal aggregations with which the data are provided include hourly averages and daily averages (the latter obtained by calculating the arithmetic mean of the 24-hourly averages for the day). An exception is made for precipitation, for which the data provided correspond to hourly and daily accumulations instead of hourly and daily averages. The data always refer to standard time (UTC+1). The time of the data is “standard time” and refers to observations obtained up to the indicated time.

As declared by ARPA Lombardia, the data available for download from ARPA Lombardia website are consistent with those in the meteorological database of ARPA Lombardia and are subject to daily and periodic checks and verifications.

To compare the observed data with the ERA5 values, it was decided to download the raw sensor data (i.e. the non-aggregated ones), which were then processed to calculate the hourly mean values. For each hour, the average was determined by taking all the data collected during that hour and computing their mean. For example, the average temperature for 4 am was calculated by averaging all the temperature readings recorded from 4:00 am to 4:50 am.

Table 2.3 – Average number of measuring stations used for each parameter, minimum, average and maximum distance between two adjacent stations

Parameter	Number of stations	Minimum, average and maximum distance between two adjacent stations [km]		
Precipitation	195	1.2	6.5	37
Temperature	185	0.9	6.7	37
Relative humidity	145	2.2	7.8	25.7
Global radiation	75	2.3	10.1	34
Wind speed	112	1.5	8.1	25.9

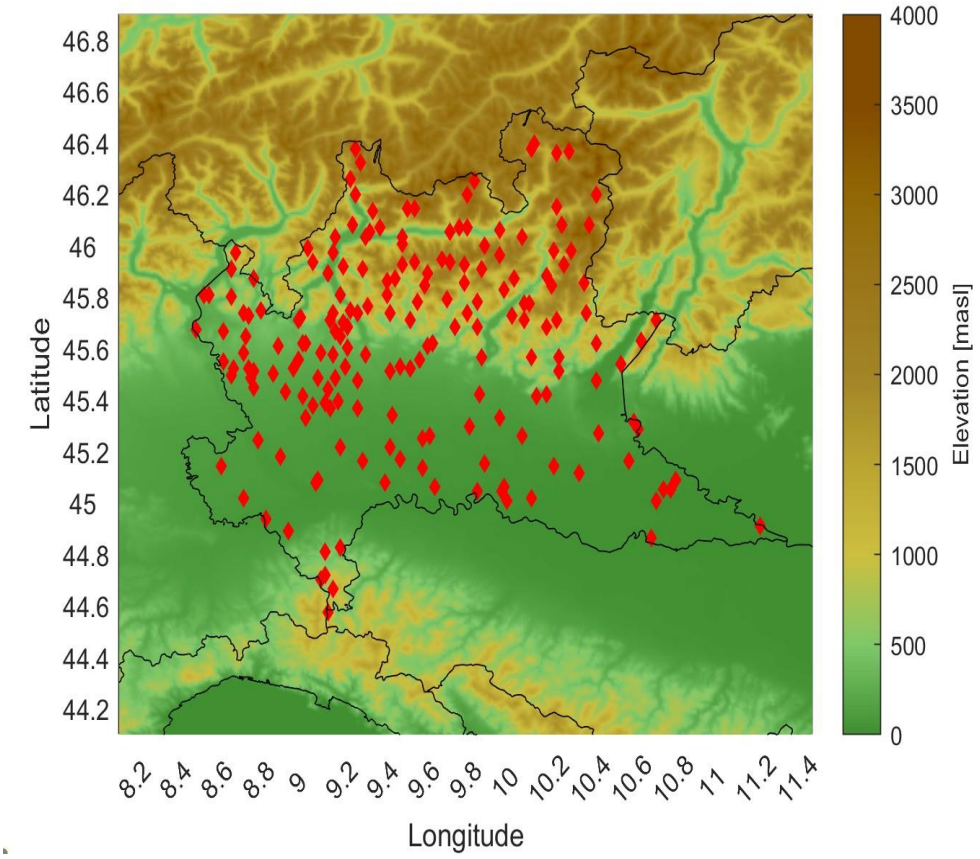

Figure 2.5 - Spatial distribution of precipitation measurement stations for the year 2015

2.6 - Measured Ozone Concentrations

The ground-based ozone concentration data used in this study were obtained from the Air Quality Download service, managed by the European Environment Agency (EEA). This database collects data provided by regional environmental agencies, which collect measurements through ground monitoring stations. Specifically, at these measuring stations ozone concentrations are measured at a height of 3 meters above the ground surface.

The framework for air quality data reporting in Europe (Air Quality e-Reporting) is established under Directive 2008/50/EC of the European Parliament and the Council of May 21st, 2008, concerning ambient air quality and cleaner air for Europe. This directive extends and builds upon earlier initiatives for reciprocal data exchange on air quality, as established by European Decisions 75/441/EEC, 82/549/EEC, and 97/101/EC.
Central to the air quality monitoring infrastructure is the European Air Quality (AQ) Portal, a digital platform that supports the Air Quality e-Reporting system. This system is a key initiative of the European Commission (EC), managed and supervised by the European Environment Agency (EEA), with support from the European Topic Centre on Human Health and the Environment (ETC/HE).

The EU Air Quality Directive provides explicit criteria for the siting of monitoring stations. These stations are strategically located in urban, suburban, and rural areas to capture pollution originating from various sources, including traffic, industrial activities, and general background pollution. The distribution and number of monitoring stations are subject to variation based on two key factors:

- Pollutant specificity: not all pollutants are consistently measured at all stations. For instance, measuring ozone at traffic-heavy locations is often deemed unnecessary. The EU Air Quality Directive prescribes criteria for the number of pollutants to be monitored, depending on pollution levels in the area.

- Temporal changes: the number of stations may vary over time due to operational reasons. Stations may be decommissioned if they no longer represent the area’s pollution characteristics, while new stations may be established in regions where pollution levels are anticipated to rise.

Under the EU Air Quality Directive, air quality monitoring is conducted via specialized monitoring stations that adhere to rigorous technical specifications concerning location, equipment, and measurement protocols. These specifications ensure the acquisition of comparable and high-quality data. A monitoring station typically consists of a small shelter housing various instruments for pollutant measurement. Air samples are drawn through inlets located on the shelter's exterior and directed to the instruments inside. Measurements are conducted either hourly or daily throughout the year, depending on the pollutant and the measurement technique employed. In the case of ozone concentration data, sampling is performed once per hour.

Table 2.4 - Number of O_3 measuring stations, minimum, average and maximum distance between two adjacent stations

Parameter	Year	Number of stations	Minimum, average and maximum distance between two adjacent stations [km]		
Ozone	2015	39	1.8	22.9	64.5
	2016	45	1.8	21.7	62.3
	2017	45	1.8	23.3	62.3
	2018	43	1.8	23	62.3
	2019	42	1.8	22.9	79.8

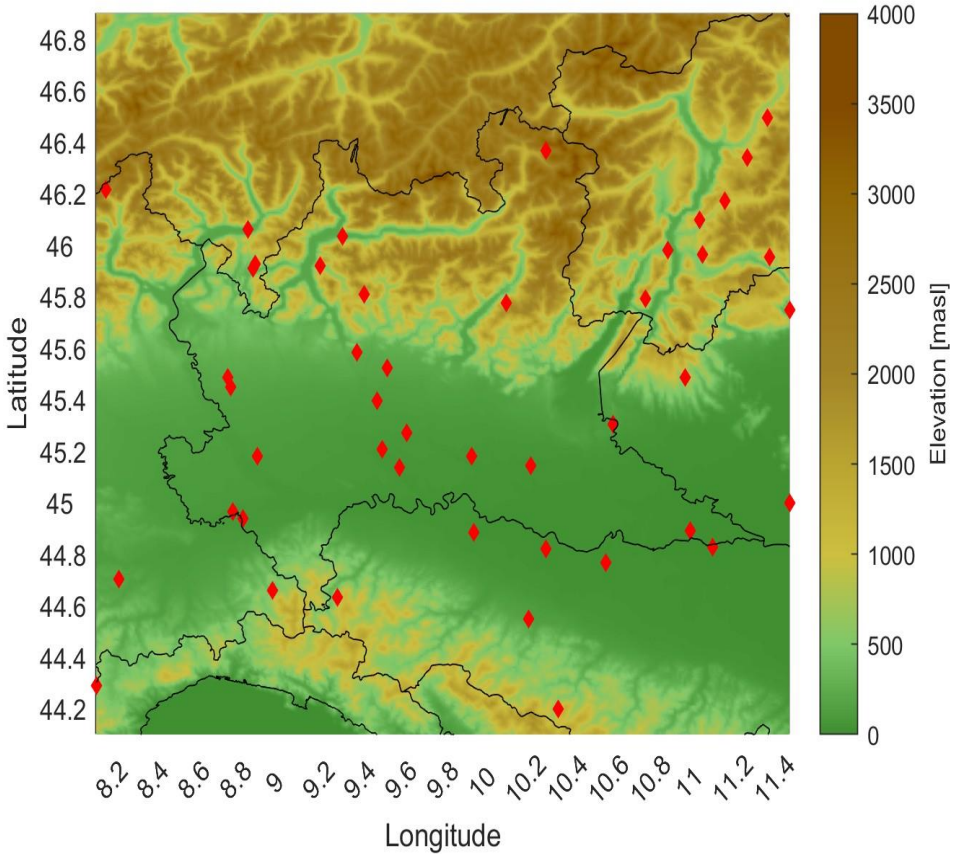

Figure 2.6 - Ozone measurement stations within the domain for the year 2016

2.7 - Data Conversion and Processing

Temperature and dewpoint temperature data provided by the ERA5 reanalysis product are expressed in Kelvin. To express these values into degrees Celsius (unit of measurement for temperature that will be used in the following), it is necessary to apply the conversion between the two different temperature scales, as reported in Eq. (2.1).

$$\mathrm{T\,[°C]} = \mathrm{T\,[K]} - 273.15 \tag{2.1}$$

Ozone values defined as mass mixing ratio (i.e., mass of ozone per kilogram of air) can be converted into concentrations in terms of parts per billion by volume (ppb_v) by applying the ideal gas law (also called general gas equation), assuming that the real gasses (ozone and air) behave like an ideal gas.

$$p \cdot V = n \cdot R \cdot T \tag{1.2}$$

where p is the absolute pressure of the gas, V is the volume of the gas, n is the number of moles of the gas (and so the amount of substance of gas), R is the ideal (or universal) gas constant and T is the absolute temperature of the gas.

Considering the definition of parts per billion by volume (the fraction of volume of gas occupied by a component multiplied by 10^9) and referring to the ideal gas law reported in Eq. (2.2), it is possible to derive a relation that allows to convert concentrations expressed as mass mixing ratio into ppb_v:

$$\mathrm{ppb_{v,O_3}} = \frac{V_{O_3}}{V_{air}} \cdot 10^9 = \frac{n_{O_3}\frac{RT}{p}}{n_{air}\frac{RT}{p}} \cdot 10^9 = \frac{kg_{O_3}}{kg_{air}} \cdot \frac{\frac{1}{M_{O_3}}\frac{RT}{p}}{\frac{1}{M_{air}}\frac{RT}{p}} \cdot 10^9 = MMR_{O_3} \cdot \frac{M_{air}}{M_{O_3}} \cdot 10^9 \tag{2.3}$$

where n (in moles) has been expressed as the ratio between the total mass of the gas m (in kilograms) and the molar mass of the gas M (in kilograms per mole) and MMR is the acronym of mass mixing ratio.

Taking into account that the molar mass of ozone is 48 $g \cdot mol^{-1}$ and assuming that air is dry and approximating its molecular weight to 29 $g \cdot mol^{-1}$, Eq. (2.3) can be written as follows:

$$\mathrm{ppb_{v,O_3}} = MMR_{O_3}\left[kg_{O_3} \cdot kg_{ry\,air}^{-1}\right] \cdot \frac{0.029\left[kg_{dry\,air} \cdot mol^{-1}\right]}{0.048\left[kg_{O_3} \cdot mol^{-1}\right]} \cdot 10^9 \tag{2.4}$$

ERA5 reanalysis (hourly data)

- Total precipitation

  Unit of measurement: m of water equivalent per hour

  Accumulations are over the hour (the processing period) ending at the validity date/time

$$\text{tp (total precipitation over the one hour ending at forecast step)}[\text{mm}] = \text{tp}\,[\text{m}] \cdot 1000 \qquad (2.5)$$

- Surface Solar Radiation (SSR)

  Unit of measurement: $J \cdot m^{-2}$

  Accumulations are over the hour (the processing period) ending at the forecast step

$$\text{SSR (average flux over the one hour ending at forecast step)}\,[\text{W} \cdot \text{m}^{-2}] = \frac{\text{SSR}\,[\text{J} \cdot \text{m}^{-2}]}{3600\,[\text{s}]} \qquad (2.6)$$

The ozone concentrations provided by the ARPA measuring stations are expressed in $\mu g \cdot m^{-3}$ (micrograms per cubic meter). To convert these values to parts per billion (by volume), it is necessary to apply the formula reported in Eq. (2.7).

$$C_{ppb}\,[ppb_v] = C_{\mu gm-3} \cdot \frac{R \cdot T}{p} \cdot \frac{1}{M_{O_3}} \cdot 10^3 \qquad (2.7)$$

where T is the air temperature (in K), M_{O3} is the molar mass of ozone (= 48 $g \cdot mol^{-1}$), $C_{\mu gm-3}$ is the concentration of ozone in $\mu g \cdot m^{-3}$, p is the air pressure (expressed in Pa) and R is the universal gas constant (= 8.314472 $J \cdot mol^{-1} \cdot K^{-1}$).

Given the two orthogonal components of wind provided by ERA5, the zonal wind u (eastward component) and the meridional wind v (northward component), horizontal 10m wind speed for each time step can be calculated through Eq. (2.8).

$$\left|\vec{V}\right|\,[\text{m} \cdot \text{s}^{-1}] = \sqrt{u^2 + v^2} \qquad (2.8)$$

For ERA5 hourly data on single level the parameter relative humidity (RH) is not available. However, temperature (T) and dew point temperature (T_d) at 2 meters are given, and, combining these two parameters, it is possible to calculate relative humidity at the same height.

Relative humidity can be defined as the ratio between the actual water vapor pressure e and the equilibrium vapor pressure over a plane of water e_s (often called saturation vapor pressure)

$$\text{RH}\,[\%] = 100 \cdot \frac{e}{e_s} \qquad (2.9)$$

Considering the definition of dew point temperature (i.e., the temperature to which an air particle at initial temperature T and pressure P must be cooled isobarically to become saturated), it is possible to write a direct relationship between the actual and saturation vapor pressure. This expression is reported in Eq. (2.10).

$$e_s(T_d) = e(T) \tag{2.10}$$

To express RH in terms of T and T_d, it is at first necessary to define an equation to express the dependence of e_s on temperature. One of the most widely used empirical expressions is the so-called Magnus equation. Eq. (2.11) reports the formula as proposed by Tetens (1930).

$$\log_{10} e = \frac{t \cdot u}{t + v} + w \tag{2.11}$$

where t indicates the temperature (in °C), w is a constant (set to 0.7858 for e_s in mbar), u and v are parameters that assume different values depending on whether the saturation vapor pressure is calculated over a plane surface of pure water (u = 7.5, v = 237.3 °C) or pure ice (u = 9.5, v = 265.5 °C). Following Murray (1967), the Tetens' equation has been modified to obtain an expression more convenient for the computation of e_s.

$$e_s\ [\mathrm{Pa}] = a\ [\mathrm{Pa}] \cdot \exp\left(\frac{b \cdot T}{c + T}\right) \tag{2.12}$$

where the air temperature T is expressed in °C, a = 610.78 Pa is a constant term, the parameter c corresponds to the term v in the Tetens' equation (and so c = 265.5 °C for temperatures below 0 °C and c = 237.3 °C for temperature above 0 °C) and b is calculated from the parameter u with the formula $b = u \cdot \ln 10$. Over ice, b assumes the value 21.8746, while over water b = 17.2694.

By substituting Eq. (2.12) in Eq. (2.10), it is possible to obtain an equation that expresses T_d as a function of the ambient vapor pressure e and temperature T:

$$T_d\ [°\mathrm{C}] = \frac{c \cdot \ln\left(\frac{e}{a}\right)}{b - \ln\left(\frac{e}{a}\right)} \tag{2.13}$$

Combining Eq. (2.13) and Eq. (2.9), an expression that allows the conversion of RH to T_d is obtained:

$$T_d\ [°\mathrm{C}] = \frac{c \cdot \left[\ln\left(\frac{RH}{100}\right) + \frac{b \cdot T}{c + T}\right]}{b - \ln\left(\frac{RH}{100}\right) - \frac{b \cdot T}{c + T}} \tag{2.14}$$

By rearranging Eq. (2.14) so that RH is written as a function of T and T_d, it is possible to calculate relative humidity from ERA5 temperature and dew point temperature data:

$$RH\ [\%] = 100 \cdot \exp\left(\frac{b \cdot c \cdot (T_d - T)}{(c + T) \cdot (c + T_d)}\right) = 100 \cdot \frac{\exp\left(\frac{b \cdot T_d}{c + T_d}\right)}{\exp\left(\frac{b \cdot T}{c + T}\right)} \tag{2.15}$$

In order to compare the ozone data from the ERA5 dataset (referred to model level 137, the closest to the Earth's surface) with measured concentrations at ground level, it is essential to apply a deposition scheme that allows to estimate the reanalysis data at the height at which sensors measure O_3 concentrations. This process requires the calculation of the actual geometric height at which ERA5 ozone values are provided and it is therefore necessary to convert model level 137 to geometric height. This conversion is achieved by making use of the hydrostatic assumption and requires the following variables: air temperature on vertical level 137 (ta), specific humidity on model level 137 (hus), air temperature at the surface (tas), specific humidity at the surface (huss), pressure at the surface (sp). Temperature values are expressed in K, specific humidity is in $kg_{H2O} \cdot kg_{air}^{-1}$ and pressure is in Pa.

Since specific humidity is not available as a surface parameter in the ERA5 dataset, it was calculated from the dew point temperature and 2 m temperature data using Eq. (2.16). Temperature was used to estimate the saturation vapor pressure (e_s, Eq. (2.12)) and temperature and dew point temperature were implemented in Eq. (2.15) to determine the relative humidity.

$$q\left[kg_{H_2O} \cdot kg_{air}^{-1}\right] = \frac{0.622 \cdot e}{P - e + 0.622 \cdot e} \tag{2.16}$$

where the actual vapor pressure is calculated as

$$e\,[Pa] = e_s(T) \cdot RH/100 \tag{2.17}$$

According to ECMWF User Documentation, the pressure on model levels (p_{ml}) is given by the mean of the pressures on the model half levels immediately above and below ($p_{half,above}$ and $p_{half,below}$). This means that the pressure on model levels is in the middle of the layers defined by the model half levels.

$$p_{ml}\,[Pa] = \frac{p_{half,above} + p_{half,below}}{2} \tag{2.18}$$

with the model half-level pressure defined as $p_{half}\,[Pa] = a + b \cdot sp$.

where a and b are coefficients defining the model levels (meaning that every model level has its own a and b values) and sp is the surface pressure. In particular, to calculate $p_{half,below}$ the a and b coefficients assume the values 0 and 1 (corresponding to model level 137), while for $p_{half,above}$ a = 0 and b = 0.997630 (values defining model level 136).

The parameter b typically has a value close to or equal to 1 at the surface and gradually decreases moving away from the surface, while a starts near 0 at the surface and increases with altitude. a is measured in the same pressure units as sp and b is dimensionless. The formula to calculate p_{ml} indicates that the sigma levels (i.e., model levels that follow the terrain) correspond closely to the surface pressure near the ground and, as altitude increases, these sigma levels become more aligned with fixed pressure levels. In many models, b eventually becomes zero, indicating that from this point upwards, the model levels correspond exactly to "horizontal" pressure levels.
This relationship allows for the construction of a vertical profile from the actual pressure coordinates of the model levels and the corresponding temperature values (ta). Additionally, the surface temperature (tas) and surface pressure (sp) values are included in this series.

Once the actual pressures corresponding to the model levels are calculated, the hydrostatic equation is employed to determine the geometric height corresponding to each model level.

$$dp = \rho \cdot g \cdot dz = \left(\frac{p}{RT}\right) \cdot g \cdot dz$$

$$\frac{R_d \cdot T_v}{g \cdot p} \cdot dp = dz \tag{2.19}$$

where p represents pressure, R_d is the specific gas constant of dry air (=287 $J \cdot kg^{-1} \cdot K^{-1}$), T_v is the virtual temperature, and g is the acceleration due to gravity.

It is important to note that the difference in gravitational acceleration between high altitudes and sea level is minimal; for example, at 9000 meters, the acceleration is approximately 9.77 $m \cdot s^{-2}$. This small difference means that for height calculations near the ground, incorporating geopotential height adjustments is not necessary.

The virtual temperature T_v is calculated as:

$$T_v = T \cdot (1 + 0.609133 \cdot q) \tag{2.20}$$

From Eq. (2.20), the virtual temperature profile is obtained by linear interpolation, and the hydrostatic equation is integrated between the surface pressure and the pressure value of the desired model level (the closest to the ground). This integration yields the geometric height corresponding to model level 137 (right hand side of Eq. (2.19)). The average geometric height to which the ozone data provided by ERA5 refers is equal to 9.88 meters (average taken considering the hourly values for the entire domain for the period 2015-2019).

After having estimated, on an hourly basis, the actual height to which the ERA5 ozone data refer ($z_{ERA5,act}$), it is possible to determine the values at the sampling height of the monitoring stations (z_{mO3}) by applying a deposition scheme. Being interested in quantifying the transfer of ozone between the two heights $z_{ERA5,act}$ and z_{mO3}, the resistive network used to model the O_3 deposition process is constituted only by one term, the atmospheric resistance $R_{aH}(z_1, z_2)$ for the transfer of a scalar quantity (such as O_3) between two heights z_1 and z_2 (with $z_1 < z_2$). The definition and calculation of this resistance are detailed in *Subsection 4.4.3*, Eq. (4.52).

To estimate the ozone concentration at the measurement height of the sensors, $O_3(z_{mO3})$, a formula structurally similar to Eq. (4.63), which is used to calculate O_3 values at the canopy height, is applied. However, in this case, the formulation is simplified by omitting the quasi-laminar resistance for ozone transfer (R_{bO3}) and the surface resistance to ozone deposition ($R_{surf,O3}$). This adjustment allows to focus solely on the atmospheric resistance between $z_{ERA5,act}$ and z_{mO3}, ensuring an accurate estimation of ozone concentrations at the monitoring station height, without the influence of ground-level processes related to the presence of crops.

2.8 - Observations and Reanalysis Data Comparison

To assess the reliability and accuracy of the reanalysis data, a comparison with ground-measured parameters has been performed. Considering that a simplified representation of ozone chemistry is used in the ECMWF IFS and in view of the crucial role of ozone values in the assessment of crop damage caused by this oxidizing agent, the validation of O_3 concentrations provided by ERA5 is of particular importance.

The evaluations reported in this *Section* were made keeping in mind that when comparing model parameters with measured data, observations are often local and refer to a specific point in space and time, rather than representing averages over a model grid box. This consideration is especially true for wind speed values, because wind observations vary on small space and time scales and are affected by the local terrain, vegetation and buildings that are represented only on average in the ECMWF Integrated Forecasting System.

Being interested in assessing the impact that different spatial resolutions have on O_3 risk estimates, comparisons were made between measured values and reanalysis data scaled to different grid resolutions. Specifically, ERA5 data was rescaled to a spatial resolution of 1 km. The choice of a resolution of 1 km was made considering Guaita et al. (2023) results, according to which the coarser resolution runs (25×25 $km^2$and 50×50 km^2) were unable to detect O_3 hotspots, and to align with the available resolution of land use, soil field capacity, and wilting point data.
To perform the spatial re-gridding of reanalysis data (i.e., adjusting the model values to the desired resolution), a simple resampling method was employed. This procedure involved bilinear interpolation to adjust the original data to a finer grid. While this approach introduces some uncertainty, as the more accurate method would involve using the reanalysis data as boundary conditions in a regional climate model, it provides a reasonably good approximation of the data at the desired resolution without requiring complex processing operations.

When comparing model data with observations, it is essential to select appropriate statistical metrics that can effectively quantify the agreement between the two. The choice of metrics should capture different aspects of the comparison, such as accuracy, bias, and variability, to provide a comprehensive evaluation of model performance with respect to measured data.

The metrics used to assess the quality of the ERA5 reanalysis dataset are:

- Root Mean Square Error

  RMSE is a widely used metric that quantifies the average magnitude of errors between model predictions and observations. It is defined as the square root of the average squared differences between predicted and observed values:

$$\mathrm{RMSE} = \sqrt{\frac{1}{n} \cdot \sum_{i=1}^{n} (P_i - O_i)^2} \tag{2.21}$$

  where P_i are the predicted values, O_i are the observations and n is the number of data points. RMSE is sensitive to large errors due to the squaring of differences, making it particularly useful when large deviations from observations are of concern. It provides a single measure of overall model accuracy.

- Mean Bias

  MB quantifies the average difference between model predictions and observations, and it is defined as:

$$MB = \frac{1}{\mathrm{n}} \cdot \sum_{\mathrm{i}=1}^{\mathrm{n}} (\mathrm{P_i} - \mathrm{O_i}) \tag{2.22}$$

  This metric indicates whether the model systematically overestimates or underestimates the observed values. A positive MB suggests overestimation, while a negative MB suggests underestimation. Mean Bias helps in understanding the direction of the error.

- Correlation Coefficient

  r measures the strength and direction of the linear relationship between model predictions and observations:

$$\mathrm{r} = \frac{\sum_{\mathrm{i}=1}^{\mathrm{n}} (\mathrm{P_i} - \overline{\mathrm{P}}) \cdot (\mathrm{O_i} - \overline{\mathrm{O}})}{\sqrt{\sum_{\mathrm{i}=1}^{\mathrm{n}} (\mathrm{P_i} - \overline{\mathrm{P}})^2 \cdot \sum_{\mathrm{i}=1}^{\mathrm{n}} (\mathrm{O_i} - \overline{\mathrm{O}})^2}} \tag{2.23}$$

  where $\overline{\mathrm{P}}$ and $\overline{\mathrm{O}}$ are the means of the predicted and observed values, respectively.
  The correlation coefficient assesses how well the model captures the variability in the observations. A high r value (close to 1 or -1) indicates that the model predictions have a strong linear relationship with the observations.

When two or more measuring stations are located within the same grid cell of the domain at a given resolution, the comparison is made by averaging the hourly data from all the stations in that cell. This means that for each hour, the average of the measurements from the different stations is calculated and used for comparison with the reanalysis data.

To make the results of the comparison easier to understand, it was decided to present the metric values as annual averages across the entire domain. Instead of displaying individual data points or station-specific results, the metrics are calculated for the entire area of interest and then spatially averaged for each year. This approach provides a clearer overview of the overall trends and patterns over time, simplifying the interpretation of how the reanalysis data compares with the observed measurements on an annual basis.

2.8.1 - Surface Meteorological Parameters

Table 2.5 - Spatially averaged metric values at 31 km resolution for the period 2015-2019

Parameter	RMSE	MB	r
Precipitation*	16.4	-0.86	0.03
Temperature	2.3	0.28	0.98
Relative humidity	12.2	0.63	0.84
Global radiation	82.7	1.12	0.94
Wind speed	1.3	-0.19	0.48

Table 2.6 - Observations and model data comparison at 1 km resolution

Parameter	RMSE	MB	r
Precipitation*	15.9	-0.84	0.04
Temperature	2.8	0.03	0.97
Relative humidity	13.9	0.40	0.81
Global radiation	88.3	2.04	0.94
Wind speed	1.4	-0.14	0.45

* Given the great temporal variability of precipitation values, it was decided to calculate the metrics considering the daily average values instead of hourly values

Comparing the results obtained at the two spatial resolutions, it can be concluded that the hourly ERA5 data relating to meteorological parameters are representative of the quantities measured on the ground and that the re-gridding technique based on bilinear interpolation does not introduce significant uncertainties in the spatial distribution of the values of these meteorological parameters. From this comparison with the observed data, it can be stated that ERA5 provides a reliable estimate for the hourly values of the meteorological parameters considered, with greater uncertainties on precipitation data (possibly due to a different temporal distribution of rainfall events between observed data and model values) and wind speed.

2.8.2 - Ozone Data

Table 2.7 – Comparison results for O_3 at different spatial resolutions

Parameter	Year	RMSE	MB	r
30×30 km²				
Ozone	2015	28.9	17.2	-0.11
	2016	27.7	16.9	-0.21
	2017	27.9	13.7	-0.42
	2018	29.8	17.8	-0.52
	2019	29.7	17.5	-0.44
1×1 km²				
Ozone	2015	29.4	17.8	-0.12
	2016	28.3	17.6	-0.22
	2017	28.2	14.2	-0.42
	2018	30.2	18.4	-0.51
	2019	30.1	18.2	-0.43

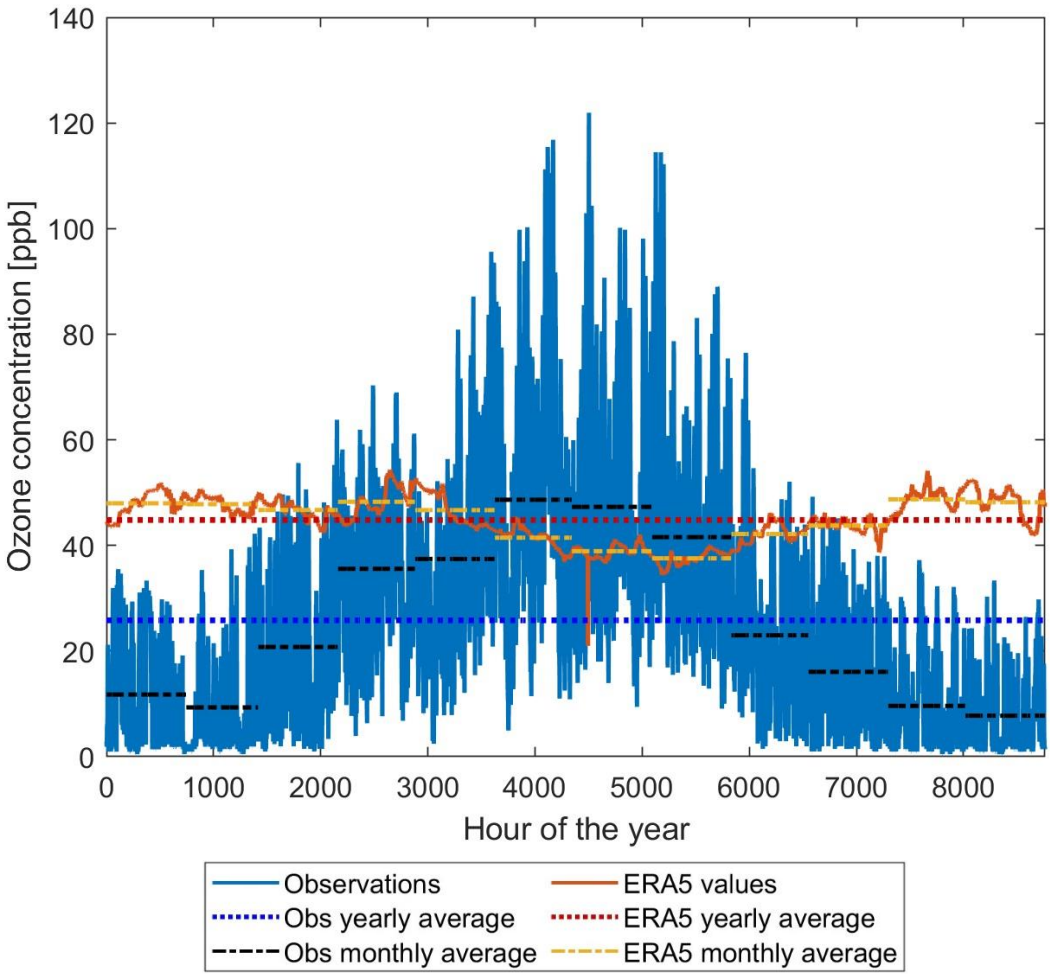

Figure 2.7 – Annual profile of O_3 concentrations for a reference monitoring station (year 2017)

Comparison results show that the simplified representation of ozone chemistry in the ECMWF Integrated Forecasting System (IFS) is unable to capture the temporal variability of ground-based ozone data.

3. Random Forest Model for Ozone Estimation

After determining that the O_3 data provided by the ERA5 reanalysis product is not reliable for assessing the potential damage ozone can inflict on vegetation, due to a consistent underestimation of O_3 concentrations compared to observed values, it became necessary to develop an alternative approach. Specifically, it was decided to create a predictive model aimed at estimating accurate ozone levels using the meteorological data available from the ERA5 dataset as a starting point.
The rationale behind this decision is to leverage the more accurate and extensive meteorological information from ERA5 to build a model that can better capture the complex relationships between meteorological conditions and ozone concentrations. This model would then be capable of providing more reliable estimates of ozone concentrations, which are critical for assessing the environmental and ecological impacts of ozone in terms of its potential to cause harm to vegetation. The new approach is expected to correct for the biases in the ERA5 ozone data and provide a more accurate tool for O_3 risk assessment.

3.1 - Model Selection and Description

Ground-monitoring stations are unable to directly provide continuous spatial distributions of O_3 concentration across large regions (Shi et al., 2018). Spatial interpolation methods, such as inverse distance weighting (Berman et al., 2015) and Kriging (Adam-Poupart et al., 2014; Guaita et al., 2023), allow for the estimation of continuous O_3 concentrations. However, these interpolated distributions may not accurately represent O_3 levels in localized areas due to the limited number of monitoring stations. Additionally, uneven station distribution, complex terrain, and abrupt changes in altitude introduce further uncertainty into O_3 assessment (Stahl et al., 2006).

Chemical transport models (CTMs), such as GEOS-Chem, CMAQ, and CAMx, are widely used for estimating ground-level O_3 concentrations. However, these models are constrained by high computational demands, relatively low spatial resolution, and uncertainties in emission inventories. Statistical models, on the other hand, offer a more computationally feasible alternative for estimating O_3 pollution, requiring fewer parameters to be collected.

Over the past decade, numerous methods have been developed for adjusting ozone levels based on meteorological conditions, aimed at forecasting, trend analysis, and investigating the mechanisms behind ozone variation. Both mechanistic and statistical modeling techniques have been applied to predict ambient O_3 concentrations.
Mechanistic models simulate the life cycle of air pollutants, including formation, emission, transport, and disappearance in numerical way, though their performance depends heavily on the availability and quality of input data (Han et al., 2008). In contrast, statistical models, such as multiple linear regression (MLR) and artificial neural networks (ANN), require fewer input parameters and have been widely used to predict ozone levels based on photochemical and meteorological variables (Biancofiore et al., 2015; Taylan, 2018). In addition to these approaches, decision tree models (e.g., Naveen et al., 2023) and random forest models (e.g., Wang et al., 2022) have been employed to predict ozone concentrations at varying spatial and temporal resolutions. Several comparative studies have also been conducted, such as Loya et al. (2012), who explored decision trees and neural networks for ozone prediction, and Juarez et al. (2022), who evaluated different machine learning techniques for forecasting tropospheric O_3 levels.

For this study, a random forest model was selected due to several key advantages. First, random forests are highly effective in handling nonlinear relationships and can capture complex interactions between meteorological parameters and O_3. Second, they offer robustness against overfitting by averaging the predictions of multiple decision trees trained on different data subsets. Furthermore, random forests provide higher accuracy compared to simpler statistical models and can manage missing data without significant performance degradation. These characteristics make the random forest model well-suited for predicting ozone concentrations in areas with limited or unevenly distributed monitoring data.

Random forests, also known as random decision forests, are an ensemble learning technique extensively employed in tasks such as classification, regression, and other related applications. This method operates by generating multiple decision trees during the training phase and then aggregating their predictions to enhance accuracy and mitigate the risk of overfitting. In the context of regression tasks, the final prediction produced by a random forest is determined by averaging the predictions from the individual trees (Ho, 1998). A key advantage of random forests is their ability to counteract the tendency of decision trees to overfit to their training data (Hastie et al., 2008).

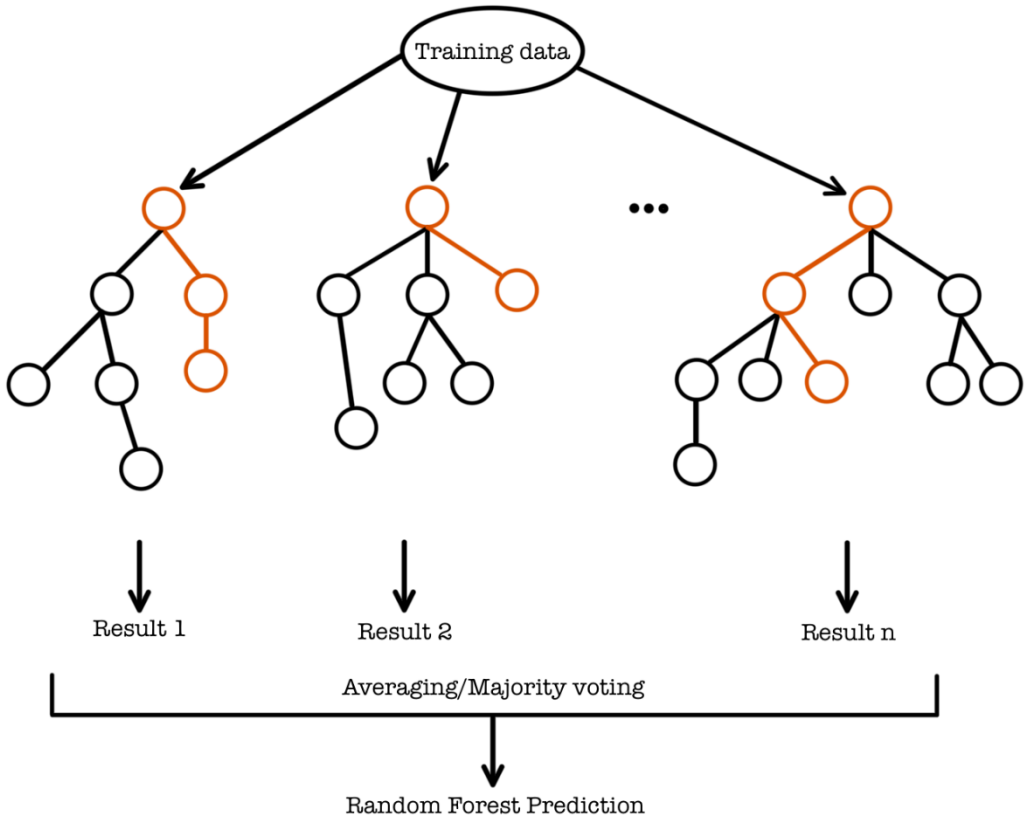

Figure 3.1 - Visual representation of a Random Forest

Decision tree learning is a supervised learning methodology utilized across statistics, data mining, and machine learning (Wu et al., 2008). Within this framework, decision trees, either for classification or regression, function as predictive models to infer conclusions from a set of observations. Specifically, when the target variable is continuous, the resulting trees are referred to as regression trees. The primary objective is to develop a model that accurately predicts the value of a target variable based on several input variables, eventually capturing complex interactions between them.
The fundamental principle underlying decision trees involves partitioning the input data, initially forming the root node of the tree, into subsets, which become the child nodes (or successor children). This partitioning is conducted recursively on each derived subset, guided by specific criteria known as splitting rules (Shalev-Shwartz et al., 2014). The resulting tree structure consists of nodes that each represent a decision based on the input features. This recursive process continues until a stopping criterion is met, such as when all observations at a node share the same target variable value, or when further splitting no longer enhances the predictive power of the model. This approach, known as the top-down induction of decision trees (TDIDT; Quinlan, J.R, 1986), exemplifies a greedy algorithm and is the most prevalent strategy for constructing decision trees from data (Rokach, L. et al., 2005).
Despite their intuitive nature and ease of interpretation, decision trees are prone to overfitting the training data, particularly when they are grown excessively deep. This overfitting manifests as a low bias but high variance, where the model captures highly specific (and irregular) patterns in the training data that do not generalize well to unseen data.

Random forests address the issue of high variance by averaging the predictions of multiple deep decision trees, each trained on different portions of the same training dataset (Hastie et al., 2008). This averaging process reduces variance at the cost of a modest increase in bias and a reduction in interpretability, but it typically results in a significant improvement in overall model performance.
The training algorithm for random forests incorporates the techniques of bootstrap aggregating (or bagging) and feature bagging to train individual decision trees. During bagging, multiple subsets of the training data are generated by sampling with replacement, meaning that some data points may appear multiple times in a subset, while others may be excluded entirely. Each subset is then used to train a separate decision tree. Additionally, feature bagging involves considering only a random subset of features at each split in the tree, further increasing the diversity among the trees.
This process produces a collection of decision trees, each with slight variations due to the differing training data and feature subsets, thereby reducing the correlation between trees, which in turn decreases the variance of the model and reduces overfitting.
Once all trees are trained, predictions for new samples X’ are obtained by averaging the outputs of the individual regression trees on X’. This ensemble method generally yields higher accuracy and robustness compared to a single decision tree, albeit with some loss in interpretability.

The use of bootstrapping contributes to improved model performance by decreasing variance without increasing bias. While a single tree's predictions are highly sensitive to noise within its training set, the averaged predictions across multiple trees are not, provided the trees are not strongly correlated. Training multiple trees on a single dataset without modification would result in highly correlated trees or potentially identical trees if the training algorithm is deterministic. Bootstrap sampling serves to decorrelate the trees by exposing them to different training subsets.

In practice, random forests typically consist of a few hundred to several thousand trees, depending on the size and characteristics of the training set. The optimal number of trees has been determined through k-fold cross-validation (with k = 6) and by analyzing the Out-of-Bag (OOB) error, which is computed as the mean prediction error for each training sample x_i, using only the trees that did not include x_i in their bootstrap sample (James et al., 2013). Given its definition, the OOB error functions as an internal validation mechanism for random forests, eliminating the need for a separate validation set. The results of the cross-validation and Out-of-Bag (OOB) error analysis indicated that the optimal number of trees for the random forest model is 100. Increasing the number of trees beyond this threshold led to longer computation times without providing substantial improvements in error reduction. Therefore, 100 trees were chosen as the most efficient balance between model performance and computational cost.

3.2 - Definition of Input Parameters

Meteorological conditions significantly influence ambient ozone concentrations, but identifying the primary atmospheric factor affecting ozone levels is challenging (Jiang et al. 2008; Salazar-Ruiz et al. 2008). This complexity arises because meteorological and ozone data strongly interact, often masking or exaggerating their individual effects.

Milanchus et al. (1998) suggest that a combination of solar radiation and specific humidity best explains the seasonal variations in ozone levels, while temperature and dew point depression are key factors in explaining short-term ozone fluctuations. Similarly, Tsakiri et al. (2010) identified solar radiation as the dominant atmospheric factor influencing ozone time series. This is due to the fact that ozone is produced through the photolysis of nitrogen dioxide and since solar radiation is the primary driver of photochemical reactions, the seasonality of ozone formation is closely linked to solar radiation patterns. As a result, ambient ozone concentrations peak during hot, sunny summer episodes characterized by low ventilation, which is caused by weak winds and limited vertical mixing (Biancofiore et al., 2015). Conversely, precipitation and high relative humidity reduce ozone levels by lowering the efficiency of photochemical production and increasing wet deposition (García et al., 2011). Atmospheric circulation plays a crucial role in dispersing ozone and its precursors, which is why wind speed and direction are strongly correlated with ambient ozone concentrations (García et al., 2011; Biancofiore et al., 2015).

Based on these insights, several meteorological variables were selected as predictors for the random forest model, using data from the ERA5 reanalysis dataset. The selected parameters include surface temperature, 10m wind speed, surface relative humidity, surface pressure, solar radiation, and total precipitation. Due to the dynamic nature of ozone formation, transport, and depletion, the model was designed to predict O_3 concentration at time t utilizing both current meteorological data and data from preceding hours. The optimal number of time-lagged values for each parameter was determined through an iterative approach.
To account for seasonal variability, a separate random forest model was trained for each month over the five-year period analyzed in this study. To estimate ozone concentrations across the entire domain, each model used as the response variable a vector containing aggregated O_3 data from all monitoring stations in the training set. The corresponding meteorological variables were used as predictors, all aggregated into a 2D matrix.

Although aggregating data from multiple stations results in the loss of spatial information, this limitation was addressed by including additional variables such as elevation, land use, latitude, and longitude in the model's predictors. These variables were incorporated for several reasons:

- Elevation: changes in altitude can significantly affect ozone distribution due to variations in temperature, pressure, and atmospheric dynamics. Higher altitudes generally experience lower air pressure, which influences the vertical mixing of air masses and ozone transport. Including elevation allows the model to capture the effects of terrain-induced ozone variations, especially in areas with complex topography, where ozone concentrations can differ greatly between valleys and elevated regions.
- Land Use: land use type (e.g., urban, agricultural, forested areas) is crucial for ozone prediction because different land cover types contribute differently to ozone production and removal. Urban areas, for instance, may have higher levels of ozone precursors such as nitrogen oxides (NO_x) from traffic and industrial sources, while forested areas might exhibit different patterns due to vegetation emissions (biogenic VOCs). Including land use data helps the model better capture the spatial heterogeneity of ozone distribution.
- Latitude and Longitude: these geographic coordinates were included to account for potential spatial patterns in ozone distribution across the domain. Latitude can capture north-south gradients in solar radiation, which influence photochemical reactions that produce ozone. Longitude helps capture potential east-west patterns, which may result from regional climate variations, prevailing winds, or proximity to specific ozone precursor sources such as industrial zones or densely populated areas. By incorporating latitude and longitude, the model can better represent these geographic trends and spatial variations across the domain.

Together, these spatial parameters – elevation, land use, latitude, and longitude – allow the model to more accurately account for both localized and large-scale spatial variations in ozone concentrations, improving its overall predictive capabilities.

3.3 - Evaluation of Model Performance

The predictive performance of the Random Forest model was evaluated using a combination of out-of-bag (OOB) error analysis and traditional performance metrics calculated on a test dataset. Given the limited availability of observations, due to the small number of available measuring stations in the domain, only a small subset of stations (4-6) was excluded from the training set for test purposes, which inherently restricted the sample size for performance evaluation.

During training, the Out-of-Bag (OOB) error was used as an internal validation measure. Since Random Forest uses bootstrapping to generate multiple training subsets by sampling with replacement, approximately one-third of the data is left out in each bootstrap iteration. This Out-of-Bag data serves as a pseudo-validation set, allowing for an unbiased and reliable estimation of the model's predictive performance without requiring a separate validation set. The OOB error provides an overall indication of how well the model generalizes to unseen data.

Table 3.1 - Average OOB error evaluated on an annual basis starting from monthly values

	2015	**2016**	**2017**	**2018**	**2019**
OOB error	3.25	3.18	3.40	3.29	3.27

To further assess the model's predictive ability, the trained Random Forest was tested on the independent test dataset. The following performance metrics were calculated on this dataset:

- Root Mean Squared Error (RMSE): This metric was used to measure the average magnitude of the prediction errors, providing an indication of how closely the model's predictions matched the observed values.
- Mean Bias (MB): The mean bias quantified the average tendency of the predictions to either overestimate or underestimate the actual ozone concentrations. A near-zero bias indicates that the model predictions do not systematically lean toward over- or under-prediction.
- Correlation Coefficient (r): This statistic assessed the strength and direction of the linear relationship between the predicted and observed values. A correlation coefficient close to 1 suggests a strong positive relationship (and so agreement) between the model outputs and actual measurements.
- Adjusted R-squared: This metric was used to quantify the proportion of variance in the observed data that is explained by the model, while adjusting for the number of predictors used. The adjusted R^2 accounts for the complexity of the model and provides a more accurate assessment of the model's explanatory power, particularly in cases with a small test dataset, ensuring that additional predictors do not artificially inflate the performance measure.

Table 3.2 - Spatial averages of performance metrics evaluated on an annual basis for the test dataset

Parameter	**Year**	**RMSE**	**MB**	r	Adjusted R^2
Ozone	2015	6.68	-3.33	0.96	0.73
	2016	5.08	-1.95	0.95	0.79
	2017	5.37	-1.68	0.94	0.83
	2018	7.78	-1.05	0.93	0.75
	2019	7.71	-1.95	0.94	0.75

Given the limited number of available measuring stations within the domain, the model's performance estimation was constrained by the small size of the test dataset. This limited sample size presents challenges in terms of generalizing the results, but the combination of OOB error analysis and detailed evaluation using robust metrics provided a comprehensive understanding of the Random Forest model's predictive capabilities. Despite the small sample, these metrics offered valuable insights into the model's ability to generalize to unseen data and provided confidence in its predictive capabilities across the domain.

The comparison proposed in *Figure 3.2* shows how the Random Forest model is able to take into account the variations over time in the measured ozone values, while the ERA5 data are not able to capture the daily and seasonal variability of O_3 concentrations.

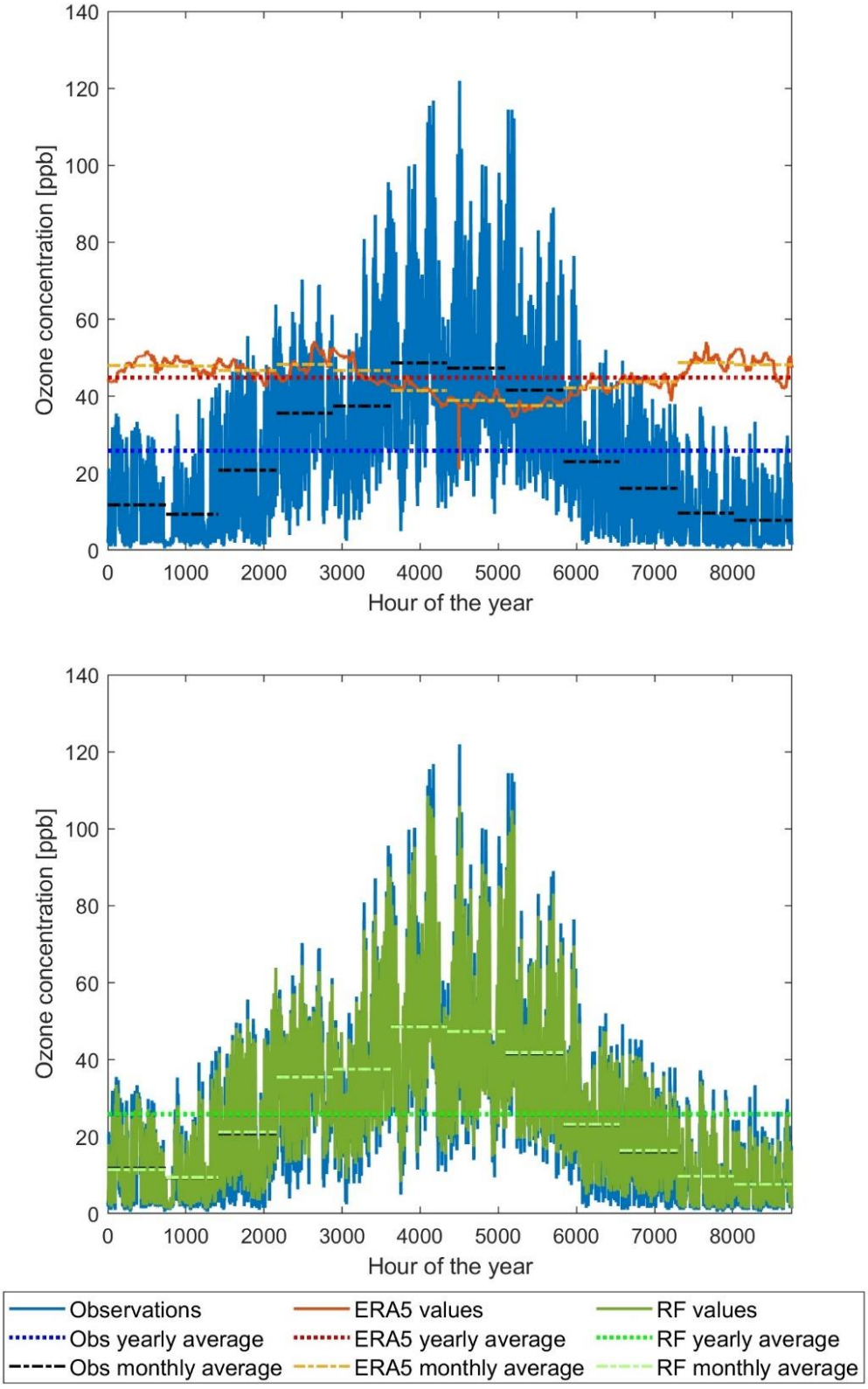

Figure 3.2 - Comparison of O_3 concentration profiles for a reference monitoring station for the year 2017

Table 3.3 - Spatial averages of metrics evaluated year by year considering all measurement stations

Parameter	Year	RMSE	MB	r	Adjusted R^2
Ozone	2015	3.48	-0.03	0.99	0.97
	2016	3.36	-0.02	0.98	0.97
	2017	3.57	-0.02	0.98	0.97
	2018	3.48	-0.03	0.98	0.96
	2019	3.42	-0.01	0.98	0.97

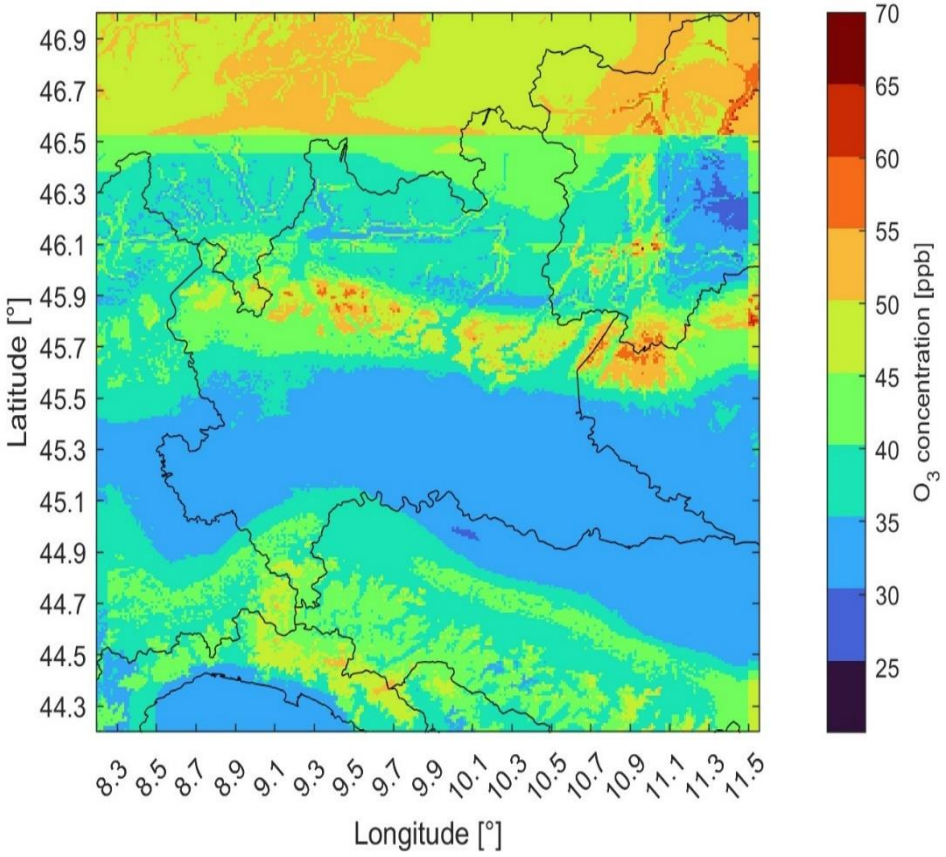

Figure 3.3 - Map of 24-hour average O_3 concentrations for the period April-June 2018

4. Dry deposition model

The hourly maps of surface temperature (°C), water vapor pressure (kPa), incoming shortwave radiation ($W \cdot m^{-2}$), and wind speed ($m \cdot s^{-1}$) obtained from ERA5 data, together with ozone (O_3) concentration values (ppb) calculated using the linear regression model described in *Chapter 3*, served as inputs for a dual-sink big leaf dry deposition model. This model estimates the Phytotoxic Ozone Dose over a detoxification threshold of 6 $nmol \cdot m^{-2} \cdot s^{-1}$ (POD_6), a flux-based metric commonly used to estimate ozone risk for crops.

The model consists of five interconnected modules:

1. The *Plant phenology Module* simulates crop growth and phenology using thermal time calculated from the sowing date (October 15th; Baruth et al., 2016). It predicts daily leaf area index (LAI), surface area index (SAI), root depth (R_d), canopy height (h_c), and the start and end dates of the ozone accumulation period. This module is critical as it determines the growth stages and physiological development of the crop, impacting how the plant interacts with environmental factors throughout the growing season.

2. The *Light Module*, that calculates photosynthetically active radiation (PAR) reaching sunlit and shaded parts of the canopy, is based on the Weiss and Norman method (Weiss & Norman, 1985). This method partitions the PAR into direct and diffuse components and estimates the amount of PAR absorbed by sunlit (LAI_{sun}) and shaded (LAI_{shad}) leaves. This is essential for accurate modelling of photosynthesis and stomatal conductance, as light availability is a primary driver of these processes.

3. The *Stomatal conductance Module* uses the Jarvis algorithm (Jarvis, 1976) to calculate at first the stomatal conductance for water of a single leaf of the crop in the upper part of the canopy ($g_{s,W}$) and, subsequently, the stomatal conductance to ozone ($g_{act,O3}$). As reported in the Mapping Manual UN/ECE (LRTAP Convention, 2017), to estimate the stomatal conductance, the module considers the effect of several environmental factors: temperature, light, plant phenology (due to the natural decline of stomatal conductance during plant growth), ozone (which causes stomatal damage due to its oxidizing behavior), vapor pressure deficit and plant available water. The module calculates the actual stomatal conductance for water by considering the maximum stomatal conductance to water ($g_{max,W}$) and applying limiting functions for each environmental factor. These functions, respectively f_{temp}, f_{light}, f_{phen}, f_{O3}, f_{VPD} and f_{PAW}, describe the reduction in stomatal conductance due to suboptimal conditions.

4. The *Atmosphere Module* scales ozone concentration from "measurement" height to top canopy height, $O_3(h_c)$, and then, through a dry deposition resistive network, computes ozone stomatal flux F_{sO3} (as done, for example, by the DO_3SE model; Emberson et al., 2000), and water fluxes (using the Penman-Monteith equation (Monteith, 1965), subsequently used in the *Soil Module*). Since $O_3(h_c)$ depends on atmospheric stability, turbulence, and the magnitude of dry ozone deposition in the canopy, the *Atmosphere Module* includes the estimation of the following atmospheric parameters: friction velocity (u*), atmospheric stability (using Monin-Obukhov Similarity Theory), atmospheric resistance for heat, water, and ozone transfer (R_{aH}) and quasi-laminar resistances for heat (R_{bH}), water (R_{bW}), and ozone (R_{bO3}) transfer, and in-canopy resistance (R_{inc}). These calculations are critical for understanding how ozone is transported and deposited in the canopy.

5. The *Soil Module* simulates soil water content dynamically through a bucket model, considering rain, intercepted precipitation by the crop, crop transpiration, soil evaporation, and evaporation from wet plant surfaces. This module ensures that the water availability for the crop is accurately modelled, which is essential for understanding plant water stress and its impact on stomatal conductance.

This comprehensive dual-sink big leaf dry deposition model integrates several environmental factors and physiological processes to estimate the flux of ozone through stomata. Thermal time drives the *Plant phenology Module*, which in turn influences the *Light Module*. The *Stomatal conductance*, *Atmosphere* and *Soil Modules* dynamically interact one with each other at each hourly timestep, by receiving as input respectively the output of the previous module, like in a cycle. The process continues in each grid node of the domain until the reference crop has reached maturity.
These interactions between modules ensure dynamic and accurate simulation of ozone deposition and its impact on crop health. The detailed consideration of phenology, light absorption, stomatal conductance, atmospheric conditions, and soil water content provides a robust framework for understanding and predicting the effects of ozone on crop productivity.

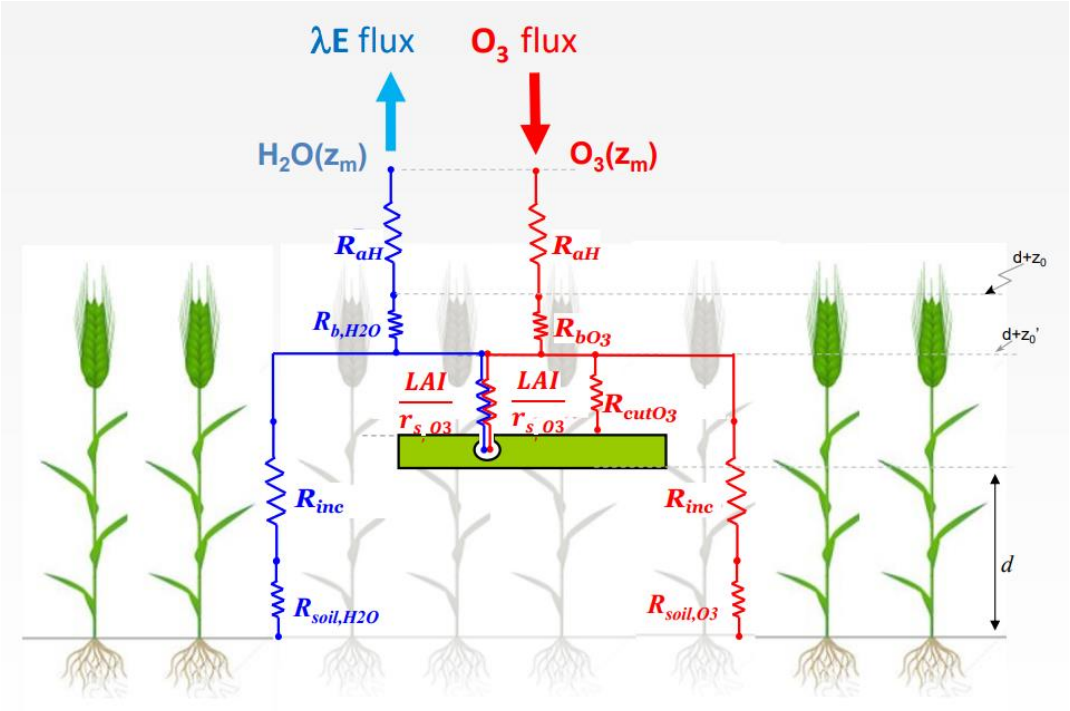

Figure 4.1 – Resistive network used to compute ozone concentration at the top of the canopy and to estimate water loss from the crop field (from Guaita et al., 2023)

4.1 - Plant phenology Module

This module uses thermal time, which accumulates the daily difference between average air temperature and a base temperature T_0 (species-specific). The plant development stages are expected to occur when thermal time reaches specific thresholds; in fact, studies have shown that thermal time controls phenological phases and plant development (Campbell & Norman, 1998). The module predicts key phenological events and attributes, such as Leaf Area Index (LAI, m^2 leaf · m^{-2} soil), Surface Area Index (SAI, m^2 plant surface · m^{-2} soil), root depth (R_d, m), and canopy height (h_c, m), which are essential for other modules to function accurately.

Thermal time (TT) at a certain day of the year (Day-Of-Year, DOY) is defined as the cumulated difference, day by day, from the sowing day (DOY_{sow}) up to the DOY of interest, between the average daily temperature T_i^* (°C) and a plant dependent base temperature (indicated as T_0, expressed in °C) specific of the considered crop; for wheat, T_0 = 0 °C.

$$\mathrm{TT_{sow}(DOY)\ [°C\ day]} = \sum_{i=\mathrm{DOY_{sow}}}^{\mathrm{DOY}} \max(T_i^* - T_0, 0) \tag{4.1}$$

The Mapping Manual UN/ECE (LRTAP Convention, 2017) provided the threshold values that relate thermal time values and wheat development stages. In this table, TT is expressed from January 1st of the year and not from the sowing day, which is usually 2–3 months before for winter wheat; for this reason, the threshold values of the Mapping Manual were converted to the respective ones expressed from the sowing day (DOY_{sow}), fixed on October 15th (Baruth et al., 2016).

$$\mathrm{TT_{sow}\ [°C\ day]} = \mathrm{TT_{1J}\ [°C\ day]} + 561 \tag{4.2}$$

where 561 is the average thermal time experienced by wheat from sowing to January 1st. This value has been estimated calculating TT from DOY_{sow} to January 1st in every cell of the domain containing wheat (determined with the land use map).

Table 4.1 shows the TT thresholds of the phenological phases for winter wheat expressed starting from the sowing date, together with the corresponding LAI values of the green leaves. The thermal time progressions for LAI have been taken from González-Fernández, et al. (2013), Zhang et al. (2018). Phenological observations in the area confirmed the present harvesting parametrization (Vignudelli & Gizzi, 2017).

Table 4.1 - Thermal time thresholds (from the sowing date) for wheat phenological phases. LAI and SAI values at each stage are also reported

Phenological phase	**TT threshold [°C day]**	**LAI value [m^2 leaf · m^{-2} soil]**	**SAI value [m^2 plant surface · m^{-2} soil]**
Emergence	$TT_1 = 370$	$LAI_1 = 0.1$	$SAI_1 = 0.14$
Tillering	$TT_2 = 530$	$LAI_2 = 0.3$	$SAI_2 = 0.43$
Stem elongation	$TT_3 = 900$	$LAI_3 = 4.5$	$SAI_3 = 6.39$
Flag leaf emergence (i.e., start of O_3 accumulation period)*	$TT_{Astart} = 1425$	$LAI_{Astart} = 6$	$SAI_{Astart} = 8.52$
Phenological phase f_2	$TT_{A2} = 1725$	$LAI_{A2} = 6$	$SAI_{A2} = 8.52$
Phenological phase f_3	$TT_{A3} = 2150$	$LAI_{A3} = 4.2$	$SAI_{A3} = 7.01$
Harvest (i.e., end of O_3 accumulation period)*	$TT_{Aend} = 2325$	$LAI_{Aend} = 0$	$SAI_{Aend} = 6.39$

* The ozone stomatal flux is computed at each timestep during the grain filling period, i.e. from anthesis (TT_{Astart}) to harvest (TT_{Aend}). In this sense, the start and end dates of the ozone accumulation period are particularly crucial for calculating POD_6, as they determine the exposure window for the crop.

Given the LAI and SAI values listed in *Table 4.1*, it is possible to define functions to predict the LAI and SAI values of green leaves at each thermal time, LAI(TT) and SAI(TT). The predicting functions have been created by interpolating the TT values with LAI and SAI values of *Table 4.1* with a first order spline. Adopting the same approach used to create the DO_3SE model (Emberson et al., 2000), values for SAI were obtained considering a constant ratio between LAI and SAI equal to 1.42. After reaching the phenological phase f_2 (i.e., when SAI begins to decline), SAI does not follow this ratio anymore and it is assumed to decline linearly until the harvest, reaching 75% of its maximum value.

In the *Plant phenology Module*, other two parameters directly related to the development stage reached by the plant at a certain DOY are calculated; these two parameters are the root depth (R_d) and the height reached by the crop's canopy (h_c).

Rooting depth normally increases rapidly from the seeding depth to a crop-specific maximum ($R_{d,max}$). In many crops, the maximum is usually attained well before physiological maturity (Borg and Grimes, 1986). Following Williams et al. (1989), R_d has been defined as a function of heat units (through the Heat Unit Index) and potential root zone depth, as reported in Eq. (4.3)

$$\mathrm{R_d(HUI)\ [m]} = \min(\mathrm{R_{d,max}}, 2.5 \cdot \mathrm{R_{d,max}} \cdot \mathrm{HUI}) \qquad (4.3)$$

where the maximum root depth $R_{d,max}$ has been set to 1 m (Fan et al., 2016) and the Heat Unit Index (HUI) is given by $\mathrm{HUI} = \mathrm{TT}/\mathrm{TT_{A_{end}}}$.

Assuming that the wheat height growth is proportional to the SAI value reached at a specific DOY, h_c (i.e., the height of the canopy at day DOY) can be defined as a fraction of the maximum plant height $h_{c,max}$ (set to 1 m for wheat).

$$h_c(\mathrm{SAI})\ [\mathrm{m}] = \mathrm{SAI}/\mathrm{SAI}_{\max} \cdot h_{c,\max} \tag{4.4}$$

According to this definition of canopy height, the plant reaches its maximum height when SAI assumes its maximum value SAI_{max}.

4.2 - Light Module

The *Light Module* employs the Weiss and Norman method (Weiss & Norman, 1985) to estimate direct and diffuse photosynthetically active radiation (PAR) from measured global radiation. Following this approach, near-infrared radiation is not considered, since leaves absorb very little radiation in this waveband (Bonan, 2019) compared to PAR. Photosynthetically active radiation designates the spectral range (wave band) of solar radiation from 400 to 700nm which is absorbed by chlorophyll pigment, and so that photosynthetic organisms are able to use for the process of photosynthesis.
The method calculates at first potential direct and diffuse PAR, and then estimates the actual PAR reaching the canopy. Subsequently, the PAR absorbed by sunlit and shaded canopy portions are estimated; these values will be fundamental in the next calculations, because the actual amount of solar radiation intercepted by the canopy influences not only photosynthesis but also the stomatal aperture of sunlit and shaded leaves (and so stomatal conductance), and water evaporation from the below-canopy soil.

At first, the solar (or shortwave) radiation values obtained from the reanalysis dataset (Q_{sw}, in $W \cdot m^{-2}$) are converted into actual total photosynthetically active radiation ($PAR_{tot,act}$, in $W \cdot m^{-2}$). This can be done assuming that 45% of the global radiation from sunlight falls under photosynthetically active radiation and supports the process of photosynthesis:

$$\mathrm{PAR}_{\mathrm{tot,act}}\ [\mathrm{W} \cdot \mathrm{m}^{-2}] = 0.45 \cdot \mathrm{Q}_{\mathrm{sw}} \tag{4.5}$$

To estimate the amount of PAR absorbed by sunlit and shaded portions of the canopy, it is required to partition $PAR_{tot,act}$ into direct and diffuse radiation.
According to the method developed by Weiss and Norman (Weiss & Norman, 1985), in order to estimate direct and diffuse PAR from the total radiation data firstly it is necessary to determine the photosynthetically active radiation that potentially reaches the Earth's surface at a specific latitude as direct beam and diffuse radiation (values called potential direct and diffuse PAR, $PAR_{dir,pot}$ and $PAR_{diff,pot}$). Eq. (4.6) and Eq. (4.7) report the formulations used to estimate these two parameters. Knowing these values, the measured to potential PAR ratio (PAR_{ratio}) is calculated with Eq. (4.9) and, finally, using Eqs. (4.12) and (4.13), the actual values of direct PAR ($PAR_{dir,act}$) and diffuse PAR ($PAR_{diff,act}$) can be estimated.

$$\mathrm{PAR_{dir,pot}\ [W \cdot m^{-2}]} = 600 \cdot \exp\left(-0.185 \cdot \left(\frac{P}{P_0}\right) \cdot m_{oa}\right) \cdot \sin B \quad (4.6)$$

$$\mathrm{PAR_{diff,pot}\ [W \cdot m^{-2}]} = 0.4 \cdot (600 - \mathrm{PAR_{dir,pot}}) \cdot \sin B \quad (4.7)$$

where B (° over the horizon) is the solar elevation angle, $m_{oa}\ [\mathrm{adim}] = 1/\sin B$ is the adimensional optical mass of the atmosphere, P (Pa) is the air pressure obtained from the reanalysis product, P_0 (Pa) is the sea-level pressure (= 101,325 Pa), 600 ($W \cdot m^{-2}$) is the average amount of visible PAR available at the top of the atmosphere (obtained by applying Eq. (4.5) to the solar constant G_{SC}, = 1320 $W \cdot m^{-2}$), 0.185 is the extinction coefficient of light for clear atmosphere and 0.4 is the fraction of intercepted direct PAR that is transformed into diffuse radiation by the surface.

The solar altitude (or elevation) is used, together with the azimuth angle, to identify the position of the Sun in the sky. B is defined as the angular distance between the center of the apparent disk of the Sun and a horizontal plane and can be estimated using the expression reported in Eq. (4.8).

$$\sin B = \cos L \cdot \cos\delta \cdot \cos H + \sin L \cdot \sin\delta \quad (4.8)$$

where L is the latitude of the location, δ is the solar declination (the angle, in degrees, between the line connecting the Earth and Sun centers and the equatorial plane at the solar noon) and H is the hour angle (in degrees), symbolically expressed as H = ±0.25 · number of minutes from local solar noon, where the + sign applies to afternoon hours and the − sign to morning hours.

δ is a function of the day of the year and varies from +23° 17' on June 21st to −23° 17'on December 21st. The hour angle of a point on the Earth's surface, defined as the angle between the meridian plane (containing Earth's axis and the zenith) and the hour circle (containing Earth's axis and the location of interest), is zero at local noon and increases in magnitude by $\pi/12$ (15 degrees) for every hour before or after noon.

To estimate the solar elevation for each hour of the year, the MATLAB function "Vectorized Solar Azimuth and Elevation Estimation", developed by Koblick D.C. (2024), was adopted. This function, given as input UTC date and time, geodetic latitude, longitude and altitude of the site, allows to predict the azimuth and elevation of the Sun within 1 degree.

In order to determine the measured to potential PAR ratio (PAR_{ratio}), it is necessary to know the actual total PAR ($PAR_{tot,act}$) and the potential total PAR ($PAR_{tot,pot}$) values. The first parameter has already been calculated with Eq. (4.5), while $PAR_{tot,pot}$ can be obtained by summing the potential direct and diffuse PAR values defined in Eqs. (4.6) and (4.7).

$$\mathrm{PAR_{ratio}\ [adim]} = \min\left(0.9, \frac{\mathrm{PAR_{tot,act}}}{\max\left(\mathrm{PAR_{tot,pot}},\ \mathrm{PAR_{tot,act}}\right)}\right) \quad (4.9)$$

The PAR_{ratio} (that has been capped at 0.9 for domain reasons) is used in Eq. (4.10) and Eq. (4.11) to estimate the fractions of total actual PAR that constitute direct ($f_{PAR,dir}$) and diffuse ($f_{PAR,diff}$) PAR. These values can then be utilized to calculate the actual values of direct PAR ($PAR_{dir,act}$) and diffuse PAR ($PAR_{diff,act}$), as described in Eqs. (4.12) and (4.13).

$$f_{PAR,dir}\,[adim] = \frac{PAR_{dir,pot}}{PAR_{tot,pot}} \cdot \left(1 - \left(\frac{0.9 - PAR_{ratio}}{0.7}\right)^{\frac{2}{3}}\right) \quad (4.10)$$

$$f_{PAR,diff}\,[adim] = 1 - f_{PAR,dir} \quad (4.11)$$

$$PAR_{dir,act}\,[W \cdot m^{-2}] = f_{PAR,dir} \cdot PAR_{tot,act} \quad (4.12)$$

$$PAR_{diff,act}\,[W \cdot m^{-2}] = f_{PAR,diff} \cdot PAR_{tot,act} \quad (4.13)$$

As proposed by Norman (1982), a spherical distribution of leaf angle within the canopy is assumed. Complying to this hypothesis, it is possible to estimate the direct and diffuse PAR reaching sunlit and shaded green leaves (PAR_{sun} and PAR_{shad}, respectively) by applying Eqs. (4.14) and (4.15).

$$PAR_{shad}\,[W \cdot m^{-2}] = PAR_{diff,act} \cdot \exp(-0.5 \cdot LAI^{0.7}) + 0.07 \cdot PAR_{dir,act} \cdot (1.1 - 0.1 \cdot LAI) \cdot \exp(-sinB) \quad (4.14)$$

$$PAR_{sun}\,[W \cdot m^{-2}] = PAR_{dir,act} \cdot 0.8 \cdot \cos(\gamma_l) \cdot \frac{1}{sinB} + PAR_{shad} \quad (4.15)$$

where γ_l is the leaf angle (assumed to be equal to 60°).

Finally, in the *Light Module*, the sunlit and shaded LAI of the canopy are estimated. This is achieved by adopting the formulations suggested by Norman (1982), reported in Eq. (4.16) and Eq. (4.17).

$$LAI_{sun}\left[m_{leaf}^2 \cdot m_{soil}^{-2}\right] = \left(1 - \exp\left(-0.5 \cdot \frac{LAI}{sinB}\right)\right) \cdot 2sinB \quad (4.16)$$

$$LAI_{shad}\left[m_{leaf}^2 \cdot m_{soil}^{-2}\right] = LAI - LAI_{sun} \quad (4.17)$$

4.3 - Stomatal conductance Module

According to the method proposed by Jarvis (1976), the regulation of stomatal conductance (parameter that controls plant's evapotranspiration and ozone uptake) by environmental factors (like leaf temperature and vapor pressure deficit) can be expressed adopting a multiplicative approach. The module applies dimensionless functions (f_i) representing light, temperature, vapor pressure deficit (VPD), plant available water (PAW), ozone, and phenology effects on stomatal conductance to the species-specific maximum stomatal conductance for water ($g_{max,W}$). Each function modifies $g_{max,W}$ based on current environmental conditions, and this allows to obtain an estimate of the actual stomatal conductance for water ($g_{act,W}$). The module then converts $g_{act,W}$ to ozone stomatal conductance ($g_{act,O3}$) using a diffusivity ratio (Massman, 1998), which is then used in the resistive network of the *Atmosphere Module*.

Adopting the empirical Jarvis approach (Jarvis, 1976), hourly values of stomatal conductance are obtained by applying the multiplicative expression reported in Eq. (4.18).

$$g_{s,W}\ [\text{mmol} \cdot \text{m}^{-2}\ \text{PLA} \cdot \text{s}^{-1}] = g_{max,W} \cdot \min(f_{phen}, f_{O_3}) \cdot f_{light} \cdot \max(f_{min}, f_{temp} \cdot f_{VPD} \cdot f_{PAW}) \qquad (4.18)$$

where $g_{max,W}$ (mmol·m^{-2} PLA·s^{-1}) is the leaf maximum stomatal conductance to water flux (parameter determined by the genetics of the plant) and f_{phen}, f_{O3}, f_{light}, f_{min}, f_{temp}, f_{VPD} and f_{PAW} are dimensionless functions, defined on a set of plant-species specific parameters, that describe the water stomatal conductance dependence on different environmental variables for a given plant species.
All dimensionless functions assume values between 0 and 1, and, as a consequence, the resulting $g_{s,W}$ is a fraction of $g_{max,W}$. Complying with the recommendations provided by the Mapping Manual UN/ECE (LRTAP Convention, 2017), the values for the parameters needed to estimate $g_{s,W}$ for the case of winter wheat are reported in *Table 4.2*. In addition, also the expressions used to estimate the hourly values of the limiting functions f_{phen}, f_{light}, f_{temp}, f_{VPD}, f_{PAW} and f_{O3} are taken from the Mapping Manual.

In view of the fact that the crop canopy is partly shaded and partly sunlit, Eq. (4.18) has to be computed twice: at first using PAR_{sun} (Eq. (4.15)) to obtain the PPFD for the sunlit portion of the canopy and then using PAR_{shad} (Eq. (4.14)). By adopting this approach, it is possible to estimate the stomatal conductance for the sunlit canopy, $g_{sW,sun}$, and the shaded part of the canopy, $g_{sW,shad}$. The actual stomatal conductance for water, $g_{act,W}$, is then calculated by weighting $g_{sW,sun}$ and $g_{sW,shad}$ for the respective portions of LAI, LAI_{sun} and LAI_{shad}.

$$g_{act,W}\ [\text{mmol} \cdot \text{m}^{-2}\ \text{PLA} \cdot \text{s}^{-1}] = \frac{g_{sW,sun} \cdot LAI_{sun} + g_{sW,shad} \cdot LAI_{shad}}{LAI} \qquad (4.19)$$

Finally, the actual stomatal conductance for ozone, $g_{act,O3}$, is obtained by multiplying $g_{act,W}$ by the ratio between the diffusivities of ozone and water in air (Massman, 1998). The values assumed by the two diffusion coefficients in standard temperature and pressure conditions are reported in *Table 4.3*.

$$g_{act,O_3}\ [\text{mmol} \cdot \text{m}^{-2}\ \text{PLA} \cdot \text{s}^{-1}] = \frac{D_{O_3,STP}}{D_{W,STP}} \cdot g_{act,W} = 0.66 \cdot g_{act,W} \qquad (4.20)$$

Table 4.2 - Parameters for winter wheat (Triticum aestivum) employed in the Jarvis' algorithm

Symbol	Value	Description
$g_{max,W}$	825 mmol $H_2O \cdot m^{-2}$ PLA$\cdot s^{-1}$	Leaf maximum stomatal conductance for water
$light_a$	0.0105	Increasing rapidity of the f_{light} function
T_{opt}	26 °C	Optimal temperature for stomatal opening (f_{temp} = 1)
T_{min}	12 °C	Minimum temperature below which f_{temp} assumes the f_{min} value
T_{max}	40 °C	Maximum temperature above which f_{temp} assumes the f_{min} value
VPD_{max}	1200 Pa	VPD below which f_{VPD} assumes its maximum value (=1)
VPD_{min}	3200 Pa	VPD above which f_{VPD} assumes its minimum value f_{min}
ΣVPD_{crit}	8000 Pa	Diurnal threshold above which stomata cannot open if humidity rises
PAW_t	50 %	Threshold below which f_{PAW} starts to decrease
a_{O3}	14	Parameter for f_{O3}
b_{O3}	8	Parameter (exponent) for f_{O3}
A_{start}	875 °C day*	Start of anthesis, i.e. start of the accumulation period
A_{mid}	1075 °C day*	Mid-anthesis
A_{end}	1775 °C day*	End of the accumulation period
p_a	0.3	Fraction of g_{max} at A_{start}
p_e	0.7	Fraction of g_{max} at p_3
p_1	875 °C day*	TT when f_{phen} reaches maximum
p_2	1175 °C day*	TT when f_{phen} stops being maximum
p_3	1600 °C day*	TT when f_{phen} is p_e

* Following the methodology adopted by González-Fernández, et al. (2013), thermal time values are expressed with respect to January 1st, while the Mapping Manual UN/ECE (LRTAP Convention, 2017) provides values relating to the mid-anthesis period.

The phenological function (f_{phen}) is a piecewise linear function, divided into 6 segments, used to describe how stomatal conductance evolves during the different growth phases of the crop. The definition of f_{phen}, reported in Eq. (4.21), is based on the formula provided by the Mapping Manual UN/ECE (LRTAP Convention, 2017), but its validity has been extended back in time to take into account the process of early evapotranspiration.

$$\begin{aligned}
&\text{For } TT < A_{start} && f_{phen} = \frac{p_a}{A_{start}} \cdot TT \\
&\text{For } A_{start} \le TT < p_1 && f_{phen} = p_a + \frac{1 - p_a}{p_1 - A_{start}} \cdot (TT - A_{start}) \\
&\text{For } p_1 \le TT < p_2 && f_{phen} = 1 \\
&\text{For } p_2 \le TT < p_3 && f_{phen} = 1 + \frac{p_e - 1}{p_3 - p_2} \cdot (TT - p_2) \\
&\text{For } p_3 \le TT < A_{end} && f_{phen} = p_e + \frac{-p_e}{A_{end} - p_3} \cdot (TT - p_3) \\
&\text{For } TT \ge A_{end} && f_{phen} = 0
\end{aligned} \qquad (4.21)$$

where thermal time is expressed with respect to January1st. The constants must respect the following condition: $A_{start} \le p_1 \le p_2 \le p_3 \le A_{end}$ (eventually, each of them may collapse on one of the closest ones, as long as continuity holds)

The light function (f_{light}) is used to describe the dependence of stomatal conductance on solar irradiance, expressed as photosynthetic photon flux density PPFD (μmol·m^{-2}·s^{-1}). The Photosynthetic Photon Flux Density measures the light that arrives at the crop canopy in the PAR zone and is defined as the amount of light that actually reaches a plant within the PAR region or the number of photosynthetically active photons that fall on a given surface (e.g., the canopy of a crop) each second and is expressed in μmol·m^{-2}·s^{-1}. PAR values can be converted to PPFD values by applying a multiplication factor of 4.57 (Sager & Tibbits, 1997): $\text{PPFD}\ [\mu\text{mol} \cdot \text{m}^{-2} \cdot \text{s}^{-1}] = 4.57 \cdot \text{PAR}$.
f_{light}, defined in Eq. (4.22), has the shape of a saturation-like curve, where the maximum is reached asymptotically at high irradiance values. The rapidity of the initial increase is regulated by the parameter $light_a$ (adim).

$$f_{light} = 1 - \exp\left(-light_a \cdot PPFD\right) \qquad (4.22)$$

By using PAR_{sun} and PAR_{shad} coming from the *Light Module* (Eqs. (4.15) and (4.14), respectively) in the f_{light} function, stomatal conductance of sunlit and shaded portions of the canopy are calculated, contributing to the actual stomatal conductance to water $g_{act,W}$. The latter is converted in the actual stomatal conductance to ozone ($g_{act,O3}$), which is then used in the resistive network of the following *Atmosphere Module*.

The temperature function (f_{temp}) aims to describe the dependence of the stomatal conductance on the air temperature T (°C). This function reaches its maximum when the air temperature is optimal for the specific plant species (T_{opt}), while it is set to its minimum (f_{min}) when air temperature drops below T_{min} or increases above T_{max} (species-specific parameters).

$$f_{temp} = \max\left(f_{min}, \frac{T - T_{min}}{T_{opt} - T_{min}} \cdot \left(\frac{T_{max} - T}{T_{max} - T_{opt}}\right)^{b}\right) \tag{4.23}$$

where $b = \frac{T_{max} - T_{opt}}{T_{opt} - T_{min}}$

The VPD function (f_{VPD}) describes the g_w dependence on air humidity, expressed as vapor pressure deficit VPD (Pa), i.e. the departure of the actual vapor pressure from the saturation point. According to its definition, reported in Eq. (4.24), f_{VPD} assumes its maximum value when VPD is below VPD_{max}, reaches its minimum value when VPD is above VPD_{min} and declines linearly when VPD increases from VPD_{max} to VPD_{min}.
Starting from the observation that stomata that have suffered high VPD conditions during a day no longer increase stomatal conductance during the same day even if air humidity increases, Uddling et al. (2004) suggested to modify the usage of the f_{VPD} function as follows: when the cumulated value of VPD from dawn (ΣVPD) to the current hour of the day exceeds the critical threshold ΣVPD_{crit}, then the value of the VPD function is capped to 92% of the f_{VPD} value of the previous hour (Uddling et al., 2004). The Uddling scheme for f_{VPD} has been adopted during the implementation of the dry deposition model described in this *Chapter*.

$$f_{VPD} = \min\left(1, \max\left(f_{min}, f_{min} + (1 - f_{min}) \cdot \frac{VPD_{min} - VPD}{VPD_{min} - VPD_{max}}\right)\right) \tag{4.24}$$

The PAW function (f_{PAW}) is used to take into account the stomatal conductance dependence on soil humidity, expressed in terms of Plant Available Water (PAW, in %). PAW is defined as the soil available water content with respect to the maximum water holding capability of the soil and is calculated using the expression reported in Eq. (4.81). f_{PAW} is 1 as long as PAW is above the threshold value PAW_t and declines linearly to zero below it.

$$f_{PAW} = \begin{cases} 1 + \frac{PAW - PAW_t}{PAW_t} & \text{if } PAW < PAW_t \\ 1 & \text{if } PAW \geq PAW_t \end{cases} . \tag{4.25}$$

The ozone function (f_{O3}) purpose is to represent the decline of g_W following early senescence of leaves due to ozone uptake.

$$f_{O_3} = \frac{1}{1 + \left(\frac{POD_0}{a_{O_3}}\right)^{b_{O_3}}} \tag{4.26}$$

where POD_0 (nmol·m^{-2} PLA) is the phytotoxic ozone dose assumed by leaves up to the previous hour. The definition of this parameter is shown in Eq. (4.27).

$$POD_0\ [\text{nmol} \cdot \text{m}^{-2}\ \text{PLA}] = \sum_{i=0}^{t} F_{s,O_3,i} \cdot 3600 \tag{4.27}$$

where $F_{s,O3,i}$ (nmol·m^{-2} PLA·s^{-1}) is the ozone stomatal flux for an uppermost leaf of unitary LAI (LAI = 1) calculated at hour i from the beginning of the ozone accumulation period. The steps required to calculate $F_{s,O3}$ are described in *Subsection 4.4.4*, and Eqs. (4.64) and (4.65) report the formulas necessary to estimate this parameter.

4.4 - Atmosphere Module

This module calculates various thermodynamic parameters and the atmospheric stability indicators using established equations and defines a resistive network in order to scale hourly wind speed and ozone concentration values to canopy height and compute ozone fluxes and evapotranspiration. The implementation of a resistive network is critical for accurate flux calculations, as it allows to describe ozone deposition pathways and water evaporation and transpiration phenomena. The module calculates the atmospheric resistance for scalar (i.e., heat, water and ozone) transfer between different heights (R_{aH}) and the quasi-laminar resistances for heat (R_{bH}), water (R_{bW}), and ozone (R_{bO3}) transfer.
Table 4.3 lists the values of all the constants used in this *Section*.

Table 4.3 - Value of constants used in the Atmosphere Module

Symbol	Value	Description
κ	0.41	Von Kármán constant
Pr	0.70673	Prandtl number
g	9.8067 $m \cdot s^{-2}$	Gravitational acceleration
M_{dry}	29 $g \cdot mol^{-1}$	Molar mass of dry air
M_W	18 $g \cdot mol^{-1}$	Molar mass of water
R	8.314472 $J \cdot mol^{-1} \cdot K^{-1}$	Universal gas constant
$D_{W,STP}$	0.2178 $cm^2 \cdot s^{-1}$	Diffusion coefficient of water in air at T = 0 °C and P = 1atm
$D_{O3,STP}$	0.1444 $cm^2 \cdot s^{-1}$	Diffusion coefficient of ozone in air at T = 0 °C and P = 1atm
$D_{H,STP}$	0.18055 $cm^2 \cdot s^{-1}$	Diffusion coefficient of heat in air at T = 0 °C and P = 1atm
$c_{p,std}$	1004.8 $J \cdot kg^{-1} \cdot K^{-1}$	Specific heat of dry air
γ	67 $Pa \cdot K^{-1}$	Psychrometric constant

The height at which meteorological parameters are defined (in the following called “measurement” height), together with surface type and canopy height, affect a variety of atmospheric parameters and, therefore, the values estimated in the resistive network. For example, roughness length and displacement height values are directly related to the canopy height h_c: according to the studies performed by Brutsaert (1982), the roughness length for momentum (z_{0m}) can be expressed as a fraction of h_c ($z_{0m} = 0.13 \cdot h_c$) and, following Campbell and Norman (1998), a similar approach can be used to estimate the displacement height d, defined as $d = 0.65 \cdot h_c$. Given this dependence, it is of particular importance to accurately define measurement height and surface type and to calculate canopy height. *Table 4.4* reports the measurement heights assumed for temperature, relative humidity, wind speed and ozone.

Table 4.4 - Measurement height values for different parameters

Symbol	Value	Description
z_{mT}	2 m	Measurement height for temperature and relative humidity[1]
z_{mw}	10 m	Measurement height for wind speed[1]
z_{mO3}	3 m	Measurement height for ozone[2]

[1] As reported in the ERA5 documentation

[2] Considering the approach adopted for estimating ozone values within the domain (described in *Chapter 3*), the height to which these values are referred is the same height at which the measurement stations collect ozone data. Ozone concentrations at monitoring stations are measured at 3 m.

4.4.1 - Thermodynamic variables

A variety of thermodynamic variables are needed in order to estimate energy and water fluxes and atmospheric stability indicators.

The saturated vapor pressure at air temperature T, $e_s(T)$, is obtained with the Tetens-Murray (1967) formula, reported in Eq. (2.12). Knowing $e_s(T)$, it is possible to calculate the actual vapor pressure, e(T), the slope of the Clausius-Clapeyron curve at increasing air temperature, Δ, the specific humidity, q, the air density, ρ, and the specific heat of air at constant pressure, c_p. The expressions used to estimate e(T) and q are reported in Eqs (2.17) and (2.16), while the formulas adopted to calculate the other parameters are described in set of equations Eq. (4.28) - Eq. (4.30).
The formulation applied to calculate the latent heat of vaporization λ, Eq. (4.31), is derived as regression from *Table A3* of Monteith & Unsworth (2014). The psychrometric constant γ is given by Eq. (4.32). The diffusivities of water (D_W) and ozone (D_{O3}) in air are calculated with the formulas proposed by Massman (1998), reported in Eqs. (4.33) and (4.34). The Schmidt numbers for water (Sc_W) and for ozone (Sc_{O3}) are calculated with Eq. (4.35) and Eq. (4.36), complying with Hicks et al. (1987).

All temperature values present in the following equations are expressed as absolute temperature (K).

$$\Delta\ [\mathrm{Pa \cdot K^{-1}}] = \begin{cases} e_s(T) \cdot \dfrac{17.269 \cdot 237.3}{(T - 36)^2} & \text{if } T > 273.15 \\ e_s(T) \cdot \dfrac{21.875 \cdot 265.5}{(T - 8.15)^2} & \text{if } T \leq 273.15 \end{cases} . \tag{4.28}$$

$$\rho\ [\mathrm{kg \cdot m^{-3}}] = \frac{P \cdot M_{dry}}{R \cdot T \cdot (1 + 0.61 \cdot q)} \cdot \frac{1}{1000} \tag{4.29}$$

$$c_p\ [\mathrm{J \cdot kg^{-1} \cdot K^{-1}}] = c_{p,std} \cdot (1 + 0.84 \cdot q) \tag{4.30}$$

$$\lambda\ [\mathrm{J \cdot kg^{-1}}] = -2733.33333 \cdot (T - 273.15) + 2501333.33333 \tag{4.31}$$

$$\gamma\ [\mathrm{Pa}\cdot\mathrm{K}^{-1}] = \frac{c_p \cdot P}{0.622} \tag{4.32}$$

$$D_W\ [\mathrm{cm}^2\cdot\mathrm{s}^{-1}] = D_{W,STP}\cdot\frac{101325}{P}\cdot\left(\frac{T}{273.15}\right)^{1.81} \tag{4.33}$$

$$D_{O_3}\ [\mathrm{cm}^2\cdot\mathrm{s}^{-1}] = D_{O_3,STP}\cdot\frac{101325}{P}\cdot\left(\frac{T}{273.15}\right)^{1.81} \tag{4.34}$$

$$Sc_W\ [\mathrm{adim}] = \frac{\nu}{D_W}\cdot 10^4 \tag{4.35}$$

$$Sc_{O_3}\ [\mathrm{adim}] = \frac{\nu}{D_{O_3}}\cdot 10^4 \tag{4.36}$$

In Eqs. (4.35) and (4.36), $\upsilon(T)$ is the kinematic viscosity of air (at air temperature T). This parameter has been determined by linearly interpolating the data from Monteith & Unsworth (2014).

4.4.2 - Energy fluxes and atmospheric stability

Net radiation (R_n) and sensible heat flux (H) are needed to calculate both atmospheric stability and evapotranspiration fluxes. In this sense, these parameters are crucial for accurately modelling the microclimate within the canopy and the interactions between the crop and the atmosphere.
R_n and H have been estimated by adopting the method proposed by Holtslag and Van Ulden (1983), which requires the calculation of the cloud cover index N, a parameter that can be estimated starting from shortwave radiation data by applying Eq. (4.37).

$$N\ [\mathrm{adim}] = \min\left(1, \sqrt[b_2]{\max\left(0, \frac{1}{b_1}\cdot\left(1-\frac{Q_{sw}}{990\cdot\sin(B)-30}\right)\right)}\right) \tag{4.37}$$

where Q_{sw} is the global short-wave radiation ($W\cdot m^{-2}$), B is the solar elevation angle (°) and b_1 (= 0.75) and b_2 (= 3.4) are empirical constants.

Following the approach described by Holtslag and Van Ulden (1983), the values of net radiation and sensible heat flux were obtained by applying Eq. (4.38) and Eq. (4.39). Before performing the calculations, it is necessary to define the different constants and parameters that appear in these two equations: α = 0.8 is a adimensional environment-dependent constant (Hanna and Chang, 1992), β = 20 $W\cdot m^{-2}$ is a constant that takes into account that during the night the heat flux is usually negative, $S = 1.5\cdot\exp(-0.060208041\cdot T)$ is an air temperature-based parameter, $c_1 = 5.31\cdot10^{-13}$ $W\cdot m^{-2}\cdot K^{-6}$ is an empirical constant, c_2 = 60 $W\cdot m^{-2}$ is a constant for mid-latitudes, $c_3 = 0.38\cdot[(1-\alpha)\cdot S+1)]/(S+1)$ is a parameter that indirectly depends on air temperature T, σ = 5.67 $W\cdot m^{-2}\cdot K^{-4}$ is the Stefan-Boltzmann constant, $G = 0.1\cdot R_n$ is the ground heat flux (which is assumed to be a fraction of net radiation; 0.1 is used for rural areas) and A, the albedo of wheat, is assumed to be 0.2 (this value has been obtained by averaging the values provided by Yeşilköy et al. (2015) from tillering to harvest).

$$R_n\,[W\cdot m^{-2}] = \frac{(1-A)\cdot Q_{sw} + c_1\cdot T^6 - \sigma\cdot T^4 + c_2\cdot N}{1+c_3} \tag{4.38}$$

$$H\,[W\cdot m^{-2}] = \begin{cases} -\alpha\cdot\beta & \text{if } Q_{sw} < 50\ \dfrac{W}{m^2} \\ \dfrac{1-\alpha+S}{1+S}\cdot(R_n - G) - \alpha\cdot\beta & \text{if } Q_{sw} \geq 50\ \dfrac{W}{m^2} \end{cases} \tag{4.39}$$

In this model, atmospheric stability is described with the Obukhov length L (Monin & Obukhov, 1954). However, the calculation of this parameter requires the friction velocity u* which, in turn, requires, in a recursive process, an information about atmospheric stability. To avoid an iterative process, the approach suggested by Hanna and Paine (1993) has been adopted: according to this method, it is possible to distinguish between atmospheric stability conditions considering the sensible heat flux value at a given time and friction velocity is calculated using empirical formulas. This approach requires the wind speed at z_{mw}, $u(z_{mw})$, and the sensible heat flux H.

If H < −1 (stable atmosphere):

$$u^*\,[m\cdot s^{-1}] = f_1\cdot\left(1+\sqrt{f_2}\right) \tag{4.40}$$

with

$$f_1 = \frac{0.5\cdot\kappa\cdot u(z_{mw})}{\log\left(\frac{z_{mw}-d}{z_{0m}}\right)} \tag{4.41}$$

$$f_2 = 1 - 4\cdot\frac{\left(4.7\cdot g\cdot z_{mw}\cdot\theta^*\cdot\log\left(\frac{z_{mw}-d}{z_{0m}}\right)\right)}{\kappa\cdot T\cdot u(z_{mw})^2} \tag{4.42}$$

$$\theta^*\,[m\cdot s^{-1}] = \min\left(0.09\cdot(1-0.5\cdot N^2), \frac{\kappa\cdot T\cdot u(z_{mw})^2}{18.8\cdot g\cdot z_{mw}\cdot\log\left(\frac{z_{mw}-d}{z_{0m}}\right)}\right) \tag{4.43}$$

If −1 ≤ H < 1 (neutral atmosphere):

$$u^*\,[m\cdot s^{-1}] = \frac{\kappa\cdot u(z_{mw})}{\log\left(\frac{z_{mw}-d}{z_{0m}}\right)} \tag{4.44}$$

If H ≥ 1 (unstable atmosphere):

$$u^* \, [m \cdot s^{-1}] = \frac{\kappa \cdot u(z_{mw})}{\log\left(\frac{z_{mw} - d}{z_{0m}}\right)} \cdot [1 + d_1 \cdot \log(1 + d_2 \cdot d_3)] \tag{4.45}$$

with

$$d_1 = \begin{cases} 0.128 + \dfrac{0.005}{\log\left(\frac{z_{mw} - d}{z_{0m}}\right)} & \text{if } \dfrac{z_{0m}}{z_{mw} - d} \leq 0.01 \\ 0.107 & \text{if } \dfrac{z_{0m}}{z_{mw} - d} > 0.01 \end{cases}. \tag{4.46}$$

$$d_2 = 1.95 + 32.6 \cdot \left(\frac{z_{0m}}{z_{mw} - d}\right)^{0.45} \tag{4.47}$$

$$d_3 = \frac{H}{c_p \cdot \rho} \cdot \frac{\kappa \cdot g \cdot (z_{mw} - d)}{T} \cdot \left(\frac{\log\left(\frac{z_{mw} - d}{z_{0m}}\right)}{\kappa \cdot u(z_{mw})}\right)^3 \tag{4.48}$$

Once estimated for a given hour, friction velocity is used in Eq. (4.49) to calculate the Obukhov length L, which is then employed in Eq. (4.50) to scale the wind speed from the measurement height z_{mw} to the top of the canopy, obtaining the value $u(h_c)$. Referring to the Monin-Obukhov Similarity Theory (Monin & Obukhov, 1954), this scaling operation can be done in all possible atmospheric conditions, by assuming a logarithmic wind profile modified according to the stability indicator L.

$$L \, [m] = \frac{-u^{*3}}{\kappa \cdot \frac{g}{T} \cdot \frac{H}{c_p \cdot \rho}} \tag{4.49}$$

$$u(h_c) \, [m \cdot s^{-1}] = \frac{u^*}{\kappa} \cdot \left[\ln\left(\frac{h_c - d}{z_{0m}}\right) - \Psi_m\left(\frac{h_c - d}{L}\right) + \Psi_m\left(\frac{z_{0m}}{L}\right)\right] \tag{4.50}$$

The stability function for momentum, $\Psi_m(\xi)$, in accordance with Bonan (2019), is given by Eq. (4.51).

$$\Psi_m(\xi) = \begin{cases} \ln\left[\dfrac{1 + x^2}{2} \cdot \left(\dfrac{1 + x}{2}\right)^2\right] - 2\,\mathrm{atan}(x) + \dfrac{\pi}{2} & \text{if } \xi < 0 \\ -5\xi & \text{if } \xi \geq 0 \end{cases}. \tag{4.51}$$

with $x \, [adim] = (1 - 16\xi)^{1/4}$

4.4.3 - Resistive network

The resistive network used to describe the ozone deposition pathways and water evaporation has been derived from Wesely (1989). In the following discussion, the resistances expressed at the level of a single leaf are indicated with lowercase symbols while the bulk resistances at the level of the entire canopy are designated with capital letters.
Adopting the methodology proposed by Bonan (2019), the atmospheric resistance for the transfer of a scalar (heat, water and ozone) between two heights z_1 and z_2 ($z_1 < z_2$), $R_{aH}(z_1, z_2)$, is given by Eq. (4.52). In the context of the application described in this *Chapter*, R_{aH} is calculated between the height $d+ z_{0m}$, where the wind speed is expected to be zero, and the measurement height of ozone and of air temperature and humidity (z_{mO3} and z_{mT}, respectively).

$$R_{aH}(z_1, z_2)\ [s \cdot m^{-1}] = \frac{1}{\kappa \cdot u^*} \cdot \left[\ln\left(\frac{z_2 - d}{z_1 - d}\right) - \Psi_H\left(\frac{z_2 - d}{L}\right) + \Psi_H\left(\frac{z_1 - d}{L}\right)\right] \quad (4.52)$$

where $\Psi_H(\xi)$ is the stability function for scalars, defined by Eq. (4.53).

$$\Psi_H(\xi) = \begin{cases} 2\ln\left(\frac{1 + y^2}{2}\right) & \text{if } \xi < 0 \\ -5\xi & \text{if } \xi \geq 0 \end{cases} \quad (4.53)$$

with $y\ [adim] = (1 - 16\xi)^{1/4}$

According to Hicks et al. (1987), the quasi-laminar resistance for heat transfer in the whole canopy, R_{bH}, can be determined by using Eq. (4.54). The quasi-laminar resistance for water (R_{bW}) and ozone (R_{bO3}) transfer within the quasi-laminar sublayer are then obtained by multiplying R_{bH} by the factor $(Sc/Pr)^{2/3}$, where Sc is, respectively, the Schmidt number for water (Eq. (4.35)) and ozone (Eq. (4.36)).

$$R_{bH}\ [s \cdot m^{-1}] = \frac{2}{\kappa \cdot u^*} \quad (4.54)$$

$$R_{bW}\ [s \cdot m^{-1}] = R_{bH} \cdot \left(\frac{Sc_W}{Pr}\right)^{\frac{2}{3}} \quad (4.55)$$

$$R_{bO_3}\ [s \cdot m^{-1}] = R_{bH} \cdot \left(\frac{Sc_{O_3}}{Pr}\right)^{\frac{2}{3}} \quad (4.56)$$

The in-canopy resistance for the transfer of scalars, R_{inc}, is defined as

$$R_{inc}\ [s \cdot m^{-1}] = \frac{14 \cdot LAI \cdot h_c}{u^*} \quad (4.57)$$

To determine the overall surface resistance to ozone deposition, $R_{surf,O3}$, calculated between the height $d + z_{0H}$ and $d + z_{0m}$, it is necessary to define the values of the soil resistance for water ($R_{soil,W}$) and for ozone ($R_{soil,O3}$). Both parameters have been set to 200 $s \cdot m^{-1}$.

$$R_{surf,O_3}\ [s \cdot m^{-1}] = \left(\frac{LAI}{r_{s,O_3}} + \frac{SAI}{r_{cut,O_3}} + \frac{1}{R_{inc} + R_{soil,O_3}}\right)^{-1} \quad (4.58)$$

where $r_{cut,O3}$, the cuticular resistance for ozone deposition on one leaf, is assumed to the constant value 2500 $s \cdot m^{-1}$ (LRTAP Convention, 2017) and $r_{s,O_3}[s \cdot m^{-1}] = \frac{1}{g_{act,O_3}}$ is the stomatal resistance for ozone uptake by one leaf that considers both sunlit and shaded LAI fractions. In order to obtain $r_{s,O3}$ in $s \cdot m^{-1}$, it is necessary to convert the ozone stomatal conductance value obtained with Eq. (4.20) from $mmol \cdot m^{-2} \cdot s^{-1}$ to $m \cdot s^{-1}$; this can be achieved by adopting the following general expression:

$$g_{stom}\ [m \cdot s^{-1}] = g_{stom}\ [mmol \cdot m^{-2} \cdot s^{-1}] \cdot 10^{-3} \cdot \frac{R \cdot T}{P} \quad (4.59)$$

Adopting the approach proposed by Emberson et al. (2000) for the development of the DO_3SE model, in the dual-sink big leaf dry deposition model the stomatal ozone flux has been referred only to one leaf in the upper canopy. To calculate the flux of ozone through the stomata of one uppermost leaf, it is necessary to determine the value of the leaf level boundary-layer resistance for ozone transfer (r_{bO3}). Referring to McNaughton and Van Den Hurk (1995), r_{bO3} can be estimated from the leaf level boundary-layer resistance for heat r_{bH}, defined in Eq. (4.60), by taking the product of this resistance and the ratio of the diffusivity of heat and ozone in air. Similarly, the boundary-layer resistance for water at leaf level (r_{bW}) is obtained by multiplying r_{bH} by the ratio between the diffusivity of heat and the diffusivity of water in air. The expressions used to estimate r_{bO3} and r_{bW} are reported in Eq. (4.61) and Eq. (4.62).

$$r_{bH}\ [s \cdot m^{-1}] = 150 \cdot \sqrt{\frac{L_d}{u(h_c)}} \quad (4.60)$$

$$r_{bO_3}\ [s \cdot m^{-1}] = \frac{D_{H,STP}}{D_{O_3,STP}} \cdot r_{bH} \quad (4.61)$$

$$r_{bW}\ [s \cdot m^{-1}] = \frac{D_{H,STP}}{D_{W,STP}} \cdot r_{bH} \quad (4.62)$$

4.4.4 – Stomatal ozone flux and POD_6

After having estimated the values assumed by the stomatal resistances included in the resistive network, it is possible to calculate the ozone concentration at the canopy height, $O_3(h_c)$, and the flux of ozone through the stomata of leaves. Eq. (4.63) can be considered a reasonable approximation of the ozone concentration at the upper surface of the boundary layer of a leaf located in the uppermost part of the canopy (Emberson et al., 2000).

$$O_3(h_c)\ [ppb_v] = O_3(z_{mO_3}) \cdot \left(1 - \frac{R_{aH}(h_c, z_{mO_3})}{R_{aH}(d + z_{0m}, z_{mO_3}) + R_{bO_3} + R_{surf,O_3}}\right) \quad (4.63)$$

Knowing the value assumed by $O_3(h_c)$ at a specific HOY (Hour-Of-Year), the hourly averaged ozone stomatal flux (F_{sO3}) for a leaf of unitary LAI positioned at top canopy is given by Eq. (4.64).

$$F_{sO_3}\ [ppb_v \cdot m\ PLA \cdot s^{-1}] = O_3(h_c)\ \cdot \frac{1}{r_{s,O_3}} \cdot \left(1 - \frac{r_{bO_3}}{r_{bO_3} + r_c}\right) \tag{4.64}$$

with $r_c\ [s \cdot m^{-1}] = \left(\frac{1}{r_{s,O_3}} + \frac{1}{r_{cut,O_3}}\right)^{-1}$

To convert $F_{s,O3}$ in nmol·m^{-2} PLA·s^{-1}, the value in ppb·m PLA·s^{-1} has to be multiplied by the air pressure P(Pa) and divided by the air temperature T (K) and the universal gas constant (J·mol^{-1}·K^{-1}):

$$F_{sO_3}\ [nmol \cdot m^{-2}\ PLA \cdot s^{-1}] = F_{sO_3}\ [ppb_v \cdot m\ PLA \cdot s^{-1}] \cdot \frac{P}{R \cdot T} \tag{4.65}$$

Stomatal ozone flux is critical for determining Phytotoxic Ozone Dose (POD), a parameter used in specific dose-effect relationships (LRTAP Convention, 2017) to estimate the effects of ozone on vegetation. The phytotoxic ozone dose for winter wheat can be defined as the cumulated ozone stomatal flux of a unitarian leaf above the instantaneous detoxification threshold Y of 6 nmol·m^{-2}·s^{-1} (LRTAP Convention, 2017) and is designated with the symbol POD_6. According to this definition, the POD_6 value at a given hour of the year t is given by Eq. (4.66).

$$POD_6\ [mmol \cdot m^{-2}\ PLA]\ = \sum_{i=0}^{t} \max\left(0, (F_{s,O_3,i} - 6) \cdot \frac{3600}{10^6}\right) \tag{4.66}$$

where $F_{sO3,i}$ (nmol·m^{-2} PLA·s^{-1}) is the average stomatal ozone flux for the i-th hour of the accumulation period and $3600 \cdot 10^{-6}$ is a factor used to convert nmol·s^{-1} to mmol·h^{-1}.

To estimate the damage caused by ozone to the vegetation present in a specific cell of the domain over the course of a year, the POD_6 metric has been calculated by summing all hourly averaged stomatal ozone fluxes for an uppermost leaf with LAI = 1 above the detoxification threshold of 6 nmol·m^{-2}·s^{-1} during the ozone accumulation period, determined considering the thermal time thresholds reported in *Table 4.2*. In other words, the ozone fluxes have been integrated over the accumulation period to obtain the total effective ozone dose experienced by the crop present in each cell of the discretized domain.

4.4.5 - Loss estimate

The LRTAP Convention (2017) identified a POD_6 critical level (CL) for winter wheat of 1.3 mmol $O_3 \cdot m^{-2}$ PLA, which corresponds to a 5% loss in grain yield, and provided a relationship between POD_6 and grain yield that can be applied to estimate the relative yield loss (RYL), expressed as a fraction of winter wheat yield not exposed to ozone (usually called attainable yield):

$$\mathrm{RYL}\ [\%] = \frac{\mathrm{Y_{act}}}{\mathrm{Y_{att}}} = 100.3 - 3.85 \cdot \mathrm{POD_6} \tag{4.67}$$

where Y_{att} is the attainable yield and Y_{act} is the actual yield.
Doing a simple conversion, Eq. (4.67) can be rewritten as:

$$\mathrm{RYL} = 1 - \mathrm{DRF} \cdot \mathrm{POD_6} \tag{4.68}$$

where DRF is the coefficient of the dose-response function identified for the species of interest. For winter wheat, DRF is set equal to 0.038.

Yield loss (YL), or damage (Zadoks, 1985), is defined as the difference between the attainable and the actual yield and, in the context of this research, represents the yield lost due to ozone damage.
In general, yield losses occur because the physiology of the growing crop is negatively affected by one or more extrinsic factors in a dynamic way over time as crop both grows (i.e., increases in biomass) and develops (i.e., passes through the different stages of its physiological development). Using the expression given in Eq. (4.68), the yield losses can be calculated by adopting Eq. (4.69).

$$\mathrm{YL} = \mathrm{Y_{att}} - \mathrm{Y_{act}} = \mathrm{Y_{act}} \cdot \frac{\mathrm{DRF} \cdot \mathrm{POD_6}}{1 - \mathrm{DRF} \cdot \mathrm{POD_6}} = \mathrm{Y_{act}} \cdot \frac{1 - \mathrm{RYL}}{\mathrm{RYL}} \tag{4.69}$$

The dual-sink big leaf dry deposition model, as described in this *Chapter*, allows to generate a yearly POD_6 map for the generic cropland area. Since there was no information on the exact wheat coverage within each grid node, the yield losses (YL) were calculated, cell by cell, under the assumption that winter wheat was uniformly distributed in the cropland area.

The definitions of relative yield loss and yield loss can also be expressed in terms of agricultural production, since to convert yield into production it is sufficient to multiply by the cultivated area (and vice versa). In particular, by expressing Eq. (4.69) in terms of quantity of harvest it is possible, once the relative yield loss due to ozone exposure and the actual harvested production are known, to determine the total quantity of harvest lost ($Prod_{lost}$) compared to that obtainable in ideal conditions:

$$\mathrm{Prod_{lost}}\ [\mathrm{kg}] = \mathrm{Prod_{att}} - \mathrm{Prod_{act}} = \mathrm{Prod_{act}} \cdot \frac{1 - \mathrm{RYL}}{\mathrm{RYL}} \tag{4.70}$$

where $Prod_{act}$ (kg) is the actual production (as reported in the statistics, and which therefore includes the impact of ozone) and $Prod_{att}$ (in kilograms) is the attainable production. This “ideal” production refers to wheat production under the current socio-economic conditions but without any ozone impact.

Having available data on the annual production $Prod_{act}$ (expressed in quintals) of winter wheat for the Lombardy region (I.Stat) and on the yearly average selling prices of soft wheat (SP_{sw}, in € per 100kg) at a national level (for Italy, Eurostat), by applying Eqs. (4.70) and (4.71) it is possible to determine the economic value of the production loss in €. Harvested production data for Lombardy and selling prices for wheat in Italy are reported in *Table 4.5*.

$$\mathrm{Rev_{lost}}\ [€] = \mathrm{Prod_{lost}}\ [\mathrm{q}] \cdot \mathrm{SP_{sw}}\ \left[\frac{€}{\mathrm{q}}\right] \tag{4.71}$$

This estimate requires the calculation of a single POD_6 value at regional level, calculated as the average of the POD_6 values at grid level.

Table 4.5 - Actual annual wheat production and selling prices per year

Year	Harvested production [quintals]	Selling price [€ per 100kg]
2015	3,200,777	19.47
2016	3,791,730	17.82
2017	3,633,062	18.77
2018	3,205,559	19.82
2019	3,032,106	19.94

4.4.6 - Water fluxes

To estimate the soil water content (main parameter of the *Soil Module*), it is necessary to determine the water losses due to evapotranspiration processes. Referring to the Penman and Monteith method (Monteith, 1965), the closure of the surface energy balance has been assumed. Following this approach, it is possible to estimate the fluxes related to transpiration of the canopy, evaporation from wet surfaces and evaporation from the soil below canopy.
The expression used to calculate the transpiration of the whole canopy, E_{can}, is reported in Eq. (4.72).

$$E_{can}\ [W \cdot m^{-2}] = \frac{\rho \cdot c_p \cdot \frac{\left(e_s\left(T_{z_{mT}}\right) - e\right)}{R_{aH}(d + z_{0m}, z_{mT}) + R_{bH}} + \Delta \cdot (R_n - G)}{\Delta + n \cdot \gamma \cdot \frac{R_{aH}(d + z_{0m}, z_{mT}) + R_{bW} + \frac{r_{s,W}}{LAI}}{R_{aH}(d + z_{0m}, z_{mT}) + R_{bH}}} \tag{4.72}$$

where e (Pa) is the vapor pressure at the height z_{mT}, $e_s(T_{zmT})$ is the saturated vapor pressure (Pa) calculated for the temperature at z_{mT}, R_n ($W \cdot m^{-2}$) is the net radiation, G ($W \cdot m^{-2}$) is the ground heat flux (assumed equal to 10% of R_n), R_{aH} ($s \cdot m^{-1}$) is the atmospheric resistance for scalars calculated from the height of momentum sink ($d + z_{0m}$) to the height of measurement of temperature and humidity (z_{mT}), R_{bH} ($s \cdot m^{-1}$) and R_{bW} ($s \cdot m^{-1}$) are the quasi-laminar resistances for heat and water transfer, $r_{s,W}$ ($s \cdot m^{-1}$) is the stomatal resistance for water (calculated as $r_{s,W} = 1/g_{s,W}$), LAI (m^2 leaf $\cdot$ m^{-2} soil) is the leaf area index of the crop and n is a parameter used to indicate whether the vegetation is amphistomatuous (n = 1) or hypostomatuous (n = 2). Since wheat is hypostomatuous, n was set to 2. The definition of the thermodynamic variables ρ (air density, $kg \cdot m^{-3}$), c_p (specific heat of air at constant pressure, $J \cdot kg^{-1} \cdot K^{-1}$), Δ (slope of the Clausius-Clapeyron curve, $Pa \cdot K^{-1}$) and γ (psychrometric constant, $Pa \cdot K^{-1}$) can be found in *Subsection 4.4.1*.

During and immediately after precipitation episodes, the amount of rain intercepted by the canopy (capped to 0.1·LAI, in accordance with Sellers et al., 1996) evaporates from the wet surfaces of the plant. Assuming that evaporation from wet surfaces (E_{wet}) occurs only during a rainfall event or within 1 hour after it, the parameter E_{wet} for HOY t is calculated, applying Eq. (4.73), only if precipitation at time t or at time t-1 is different from zero.

$$E_{wet}\ [W \cdot m^{-2}] = \frac{\rho \cdot c_p \cdot \frac{\left(e_s\left(T_{z_{mT}}\right) - e\right)}{R_{aH}(d + z_{0m}, z_{mT}) + R_{bH}} + \Delta \cdot (R_n - G)}{\Delta + n \cdot \gamma \cdot \frac{R_{aH}(d + z_{0m}, z_{mT}) + R_{bW}}{R_{aH}(d + z_{0m}, z_{mT}) + R_{bH}}} \tag{4.73}$$

The evaporation from the soil below canopy, E_{soil}, is assumed to occur only when the water available to the plant's roots (PAW) is above 50% and is calculated using the formulation reported in Eq. (4.74).

$$E_{soil}\ [W \cdot m^{-2}] = \frac{\rho \cdot c_p \cdot \frac{\left(e_s\left(T_{z_{mT}}\right) - e\right)}{R_{aH}(d + z_{0m}, z_{mT}) + R_{bH} + R_{inc}} + \Delta \cdot (R_{n,soil} - G)}{\Delta + n \cdot \gamma \cdot \frac{R_{aH}(d + z_{0m}, z_{mT}) + R_{bW} + R_{inc} + R_{soil,W}}{R_{aH}(d + z_{0m}, z_{mT}) + R_{bH} + R_{inc}}} \tag{4.74}$$

In Eq. (4.74), the parameter $R_{n,soil}$ ($W \cdot m^{-2}$) is the net radiation at the soil level below canopy, calculated as $R_{n,soil} = R_n \cdot \exp(-\kappa \cdot LAI)$, with κ coefficient of light extinction within the canopy, set to 0.65 (Williams et al., 1989). R_{inc} and $R_{soil,W}$ are, respectively, the aerodynamic resistance of the in-canopy transport of scalars and the soil resistance to water evaporation (both are expressed in $s \cdot m^{-1}$).

Finally, evaporation fluxes are converted to mm per hour, dividing by the latent heat of vaporization λ and multiplying by 3600:

$$\begin{aligned} \mathrm{E}\left[\mathrm{kg}_{\mathrm{H_2O}} \cdot \mathrm{m}^{-2} \cdot \mathrm{s}^{-1}\right] &= \mathrm{E}\left[\mathrm{W} \cdot \mathrm{m}^{-2}\right] \cdot \frac{1}{\lambda} \\ \mathrm{E}\left[\mathrm{mm} \cdot \mathrm{h}^{-1}\right] &= \mathrm{E}\left[\mathrm{kg}_{\mathrm{H_2O}} \cdot \mathrm{m}^{-2} \cdot \mathrm{s}^{-1}\right] \cdot 3600 \end{aligned} \tag{4.75}$$

4.5 - Soil Module

In the *Soil Module*, a water mass balance (in the form of a bucket model) is used to estimate the amount of water available in the soil for crop roots. The structure of the bucket model was defined adopting the approach proposed by Mintz & Walker (1993): to calculate the soil water content (which influences plant water stress and stomatal conductance), the model considers rain, canopy interception (i.e., the amount of precipitation intercepted by the canopy), crop transpiration and evaporation. This module ensures that water availability is updated dynamically, hour by hour, based on current and past conditions. Since the bucket model requires an initial condition related to soil water content, the soil is assumed to be at field capacity on January 1st at 00 UTC.

To correctly model the soil water availability to the roots of the crop, it is necessary to impose a constraint on the maximum amount of extractable water that can be stored in the soil. This parameter is strongly dependent on the soil type, as it is a function of the field capacity and wilting point of the soil. Field capacity corresponds to the superior limit of available water and is defined as the amount of soil moisture or water content held in soil after drainage of the water contained in the macropores by gravity action. The wilting point, also called the permanent wilting point, corresponds to the inferior limit of available water and may be defined as the amount of water that is held so tightly by the soil matrix that roots cannot absorb this water, and if the soil water content decreases to this or any lower point a plant wilts and can no longer recover its turgidity when placed in a saturated atmosphere for 12 hours

The maximum water holding capacity (MWHC), i.e. the maximum amount of water that soil may retain, can be estimated, once the volumetric water content at field capacity (θ_{FC}, in m^3 $H_2O \cdot m^{-3}$ soil) and the wilting point (θ_{WP}, in m^3 $H_2O \cdot m^{-3}$ soil) are defined, using Eq. (4.76).

$$\mathrm{MWHC}\,[\mathrm{mm}] = 1000 \cdot \mathrm{R_d} \cdot (\theta_{\mathrm{FC}} - \theta_{\mathrm{WP}}) \tag{4.76}$$

To take into account that, during a precipitation event, part of the rain falling towards the ground is intercepted by the crop canopy, it is necessary to define the storage capacity of the canopy, indicated with the symbol $S_{c,max}$. According to Sellers et al. (1996), this parameter can be estimated using the expression shown in Eq. (4.77).

$$\mathrm{S_{c,max}}\,[\mathrm{mm}] = 0.1 \cdot \mathrm{LAI} \tag{4.77}$$

Considering the processes that may occur at a certain hour of the year (precipitation, canopy interception and evaporation), the current amount of water stored on the canopy ($S_{c,i}$) can be calculated, as reported in Eq. (4.78), by making the balance between the amount of rainfall (p) and evaporation (E_{wet}) of the current hour and the water stored on the canopy in the previous hour (all values are expressed in mm).

$$S_{c,i}\ [\mathrm{mm}] = \min[S_{c,max}, \max(p + S_{c,i-1} - E_{wet}, 0)] \tag{4.78}$$

AWC_i (the available water content at hour i), i.e. the water that is available for the plants at a specific hour of the year, is estimated, as shown in Eq. (4.79), by imposing a balance between the hourly rainfall intake and evapotranspiration losses.

$$AWC_i\ [\mathrm{mm}] = W_{in} - E_{can} - E_{soil} + AWC_{i-1} \tag{4.79}$$

where W_{in}, calculated using Eq. (4.80), is the water that drips on the soil.

$$W_{in}\ [\mathrm{mm}] = \max\ (p + S_{c,i-1} - E_{wet} - S_{c,max}, 0) \tag{4.80}$$

AWC is initialized at MWHC on January 1st at 00 UTC.

Plant available water (PAW) is a percentage value used in the *Stomatal conductance Module* to calculate the function f_{PAW}. PAW is defined as reported in Eq. (4.81).

$$PAW_i\ [\%] = \frac{AWC_i}{MWHC} \tag{4.81}$$

5. Results and Discussion

This *Chapter* reports the results of the calculations described in *Chapter 4*, divided by year. For the years from 2017 to 2019 a comparison was made with the results of other studies in which the analyzed domain was included.
The maps displayed in the following figures show only the grid nodes corresponding to cropland area where wheat reached maturity, which were mostly located in the plain and valley floors.

5.1 - POD_6 Maps

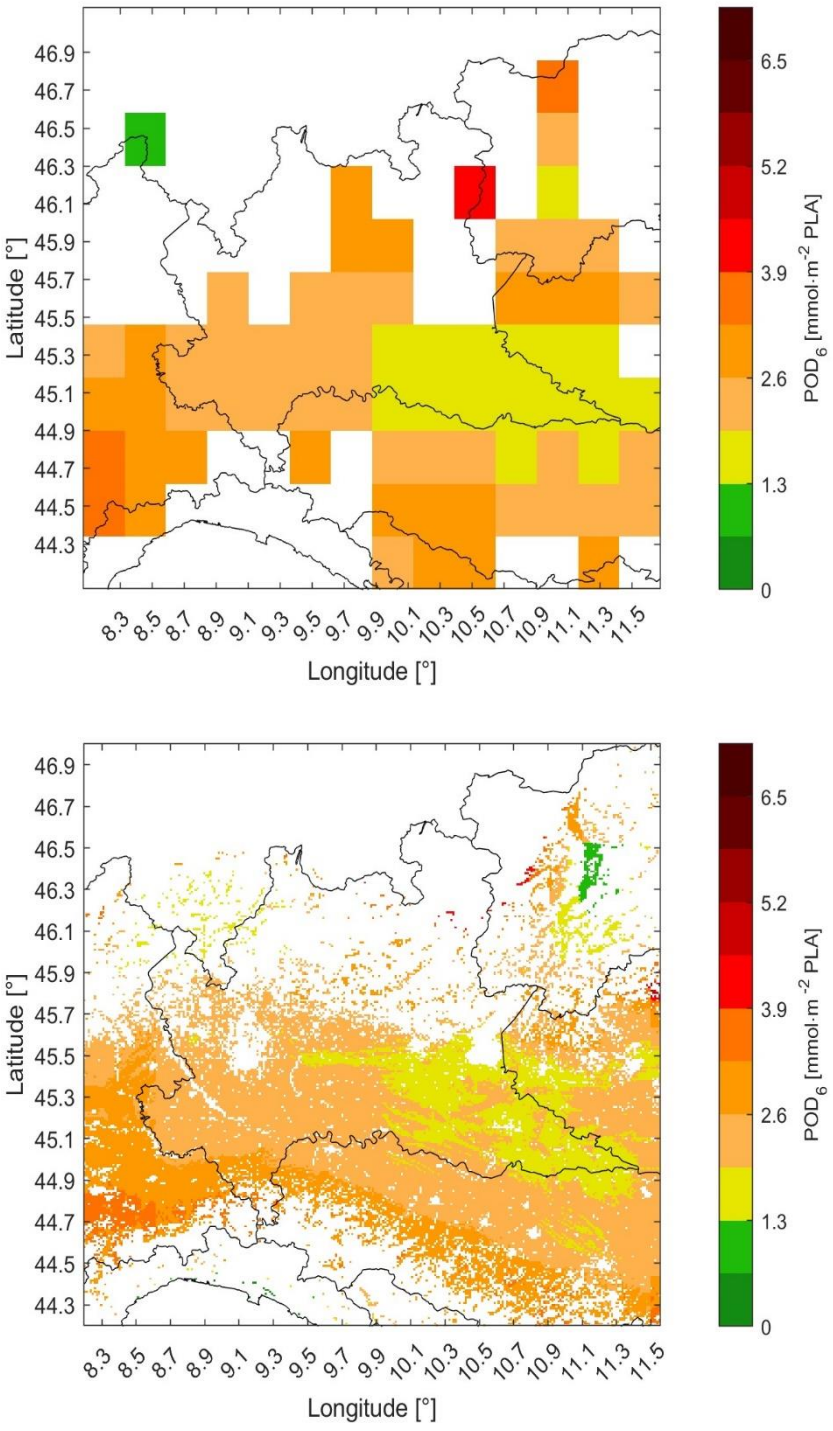

Figure 5.1 - POD_6 for year 2015 at 30×30 km² and 1×1 km² resolution

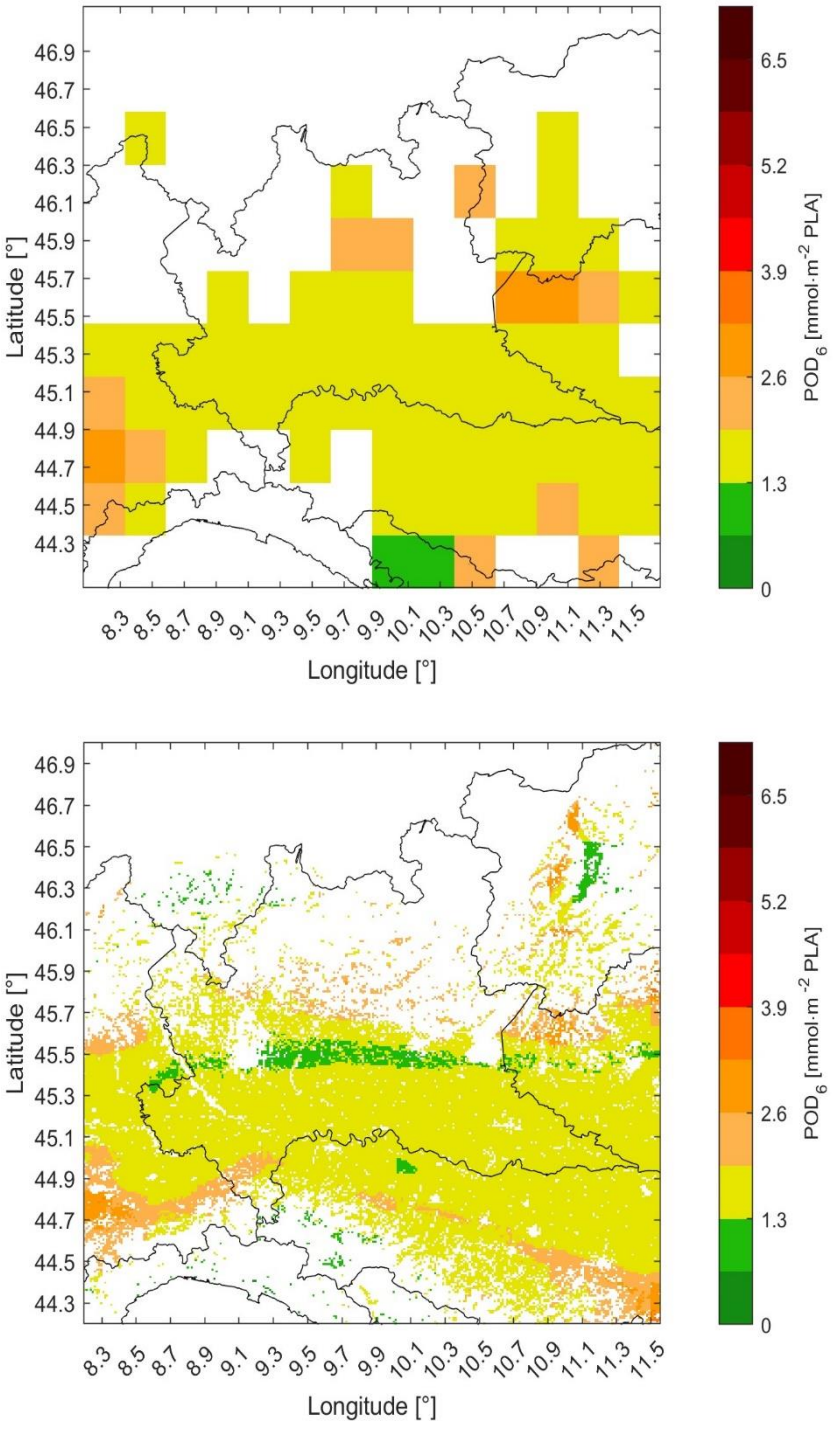

Figure 5.2 - POD_6 for year 2016 at 30×30 km^2 and 1×1 km^2 resolution

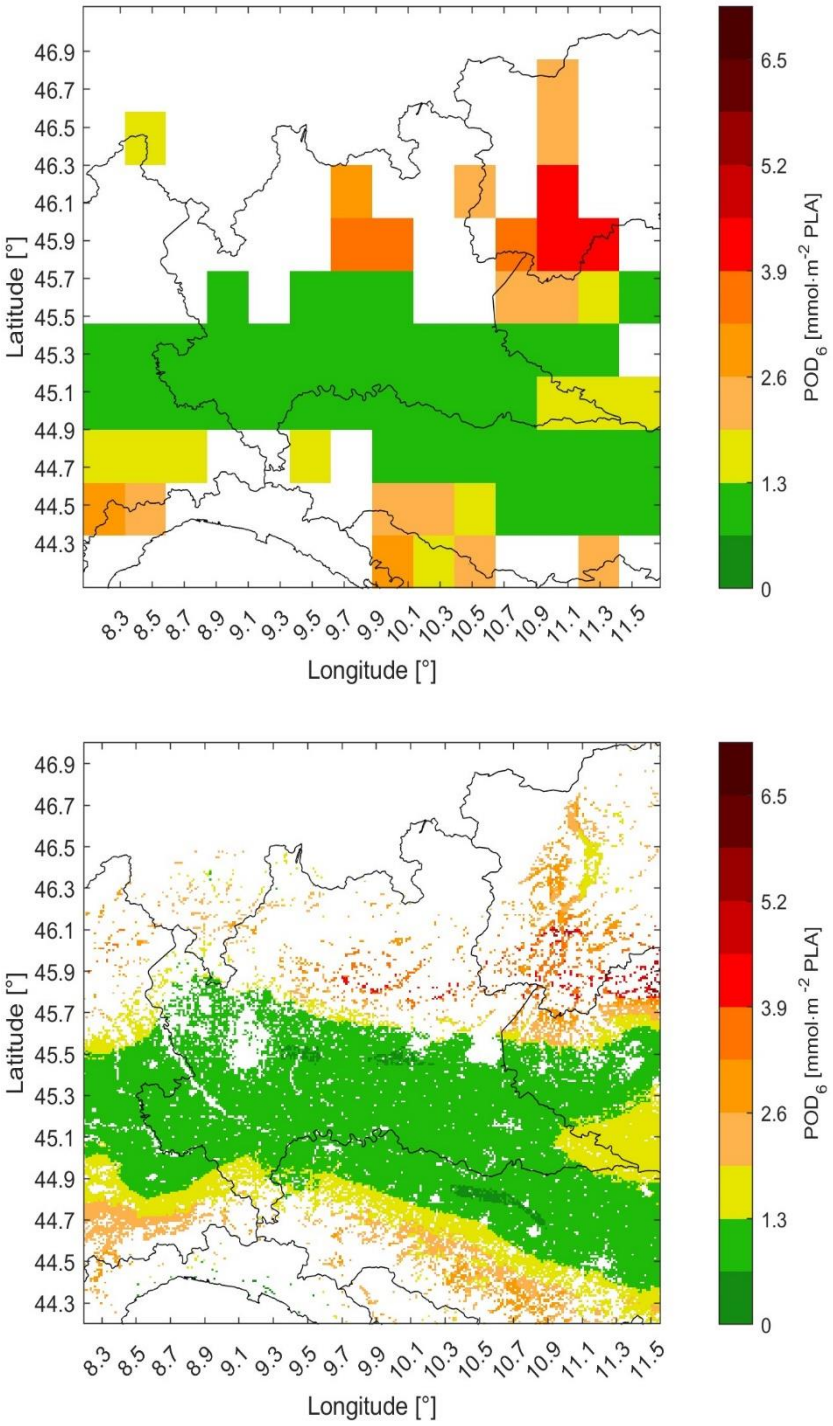

Figure 5.3 - POD_6 for year 2017 at 30×30 km² and 1×1 km² resolution

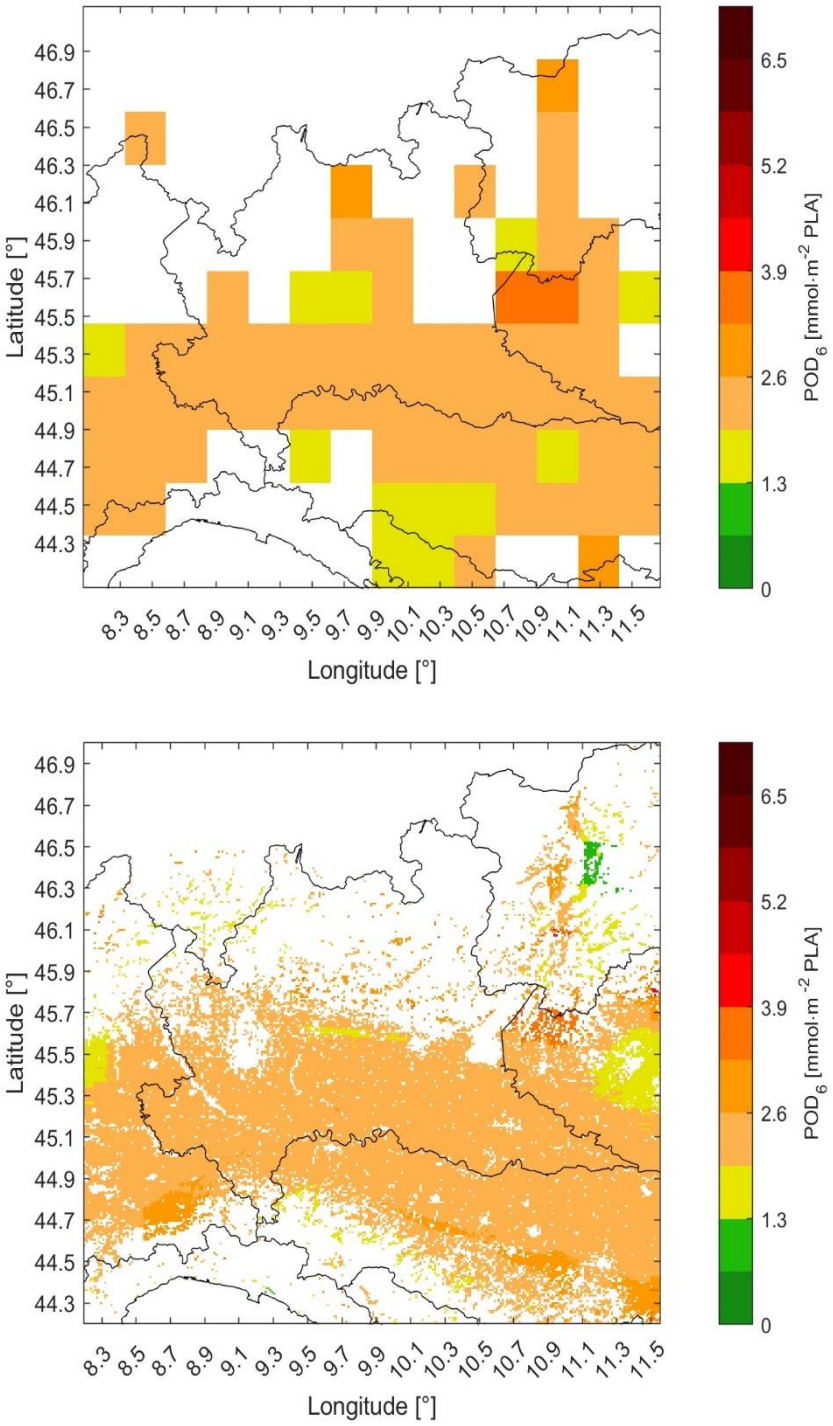

Figure 5.4 - POD_6 for year 2018 at 30×30 km^2 and 1×1 km^2 resolution

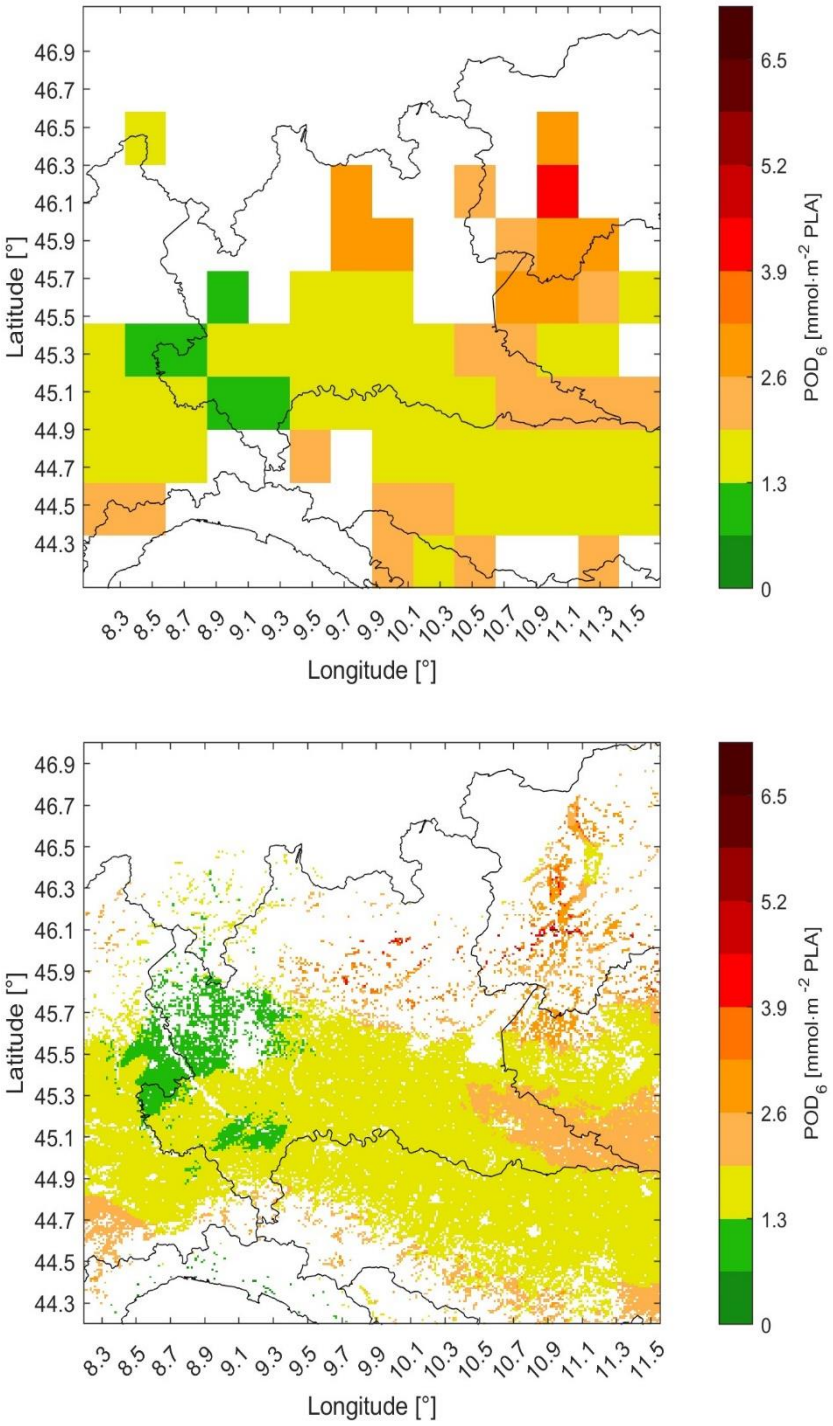

Figure 5.5 - POD_6 for year 2019 at 30×30 km^2 and 1×1 km^2 resolution

Guaita et al. (2023), who performed an ozone risk assessment for Lombardy for 2017 using mapped (with a Kriging with Trend Model) hourly data of meteorological variables and O_3 concentrations from regional monitoring networks, reported an average POD_6 value over the whole domain of 2.03±0.81 mmol·m^{-2} PLA for the analysis performed at a spatial resolution of 1×1 km^2. Compared to the results obtained in this study (average POD_6 for 2017 equal to 1.82±0.91 mmol·m^{-2} PLA at 1 km resolution), the approach based on the spatialization of observed data suggests greater damage to wheat.

Considering the results reported by Horálek et al. (2020), who calculated the POD_6 for wheat in 2018 with a resolution of 2×2 km^2 and obtained values mainly in the range 3 to 4 $mmol \cdot m^{-2}$ PLA for the domain of interest, the damage estimate obtained with the present study for the same year at 1×1 km^2 resolution is lower, with most POD_6 values between 1.95 and 2.6 $mmol \cdot m^{-2}$ PLA and a domain average of 2.24±0.41 $mmol \cdot m^{-2}$ PLA.

Schucht et al. (2021) assessed the O_3 risk for bread wheat across Europe with a spatial resolution of 2 km and estimated a POD_6 between 1.5 and 3 $mmol \cdot m^{-2}$ PLA for the year 2019. These results are quite in line with what was obtained using the ERA5 reanalysis product data as input, although the distribution of values obtained in this study tends to remain close to the lower limit of the range reported by Schucht et al. (2021), with an average POD_6 value for the entire domain of 1.95±0.65 $mmol \cdot m^{-2}$ PLA.

Table 5.1 - Space-averaged POD_6 ($mmol \cdot m^{-2}$ PLA) values at the two spatial resolutions

Year	30×30 km^2	1×1 km^2
2015	2.47±0.67	2.43±0.59
2016	1.70±0.41	1.67±0.39
2017	1.87±0.94	1.82±0.91
2018	2.13±0.44	2.24±0.41
2019	1.93±0.59	1.95±0.65

By comparing the maps presented in *Figures 5.1 - 5.5* with the average POD_6 values in *Table 5.1*, it can be observed that, aside from minor differences in predicted POD_6 values, the dose distribution remained generally consistent across the plain region of the domain. However, variations were evident in hilly or piedmont areas, where finer-scale elevation changes occur, and coarser resolution analyses failed to capture localized hotspots. This consideration highlights the importance of using high spatial resolution data for estimating ozone damage to vegetation, particularly in regions with complex orography. Higher resolution allows for the identification of critical areas in greater detail, which would not be possible with simulations conducted at coarser spatial resolutions.

5.2 - Yield reduction Maps

This *Section* shows the maps of yield reduction (YR) due to the damage caused by ozone compared to the ideal value (Y_{att}). YR was calculated as $\mathrm{YR}\,[\%] = (1 - \mathrm{RYL}) \cdot 100$, where RYL is the relative yield loss defined in Eq. (4.68).
Compared to POD_6 maps, the spatial distribution of the yield reduction is more immediate and easier to interpret and allows to have an immediate idea of the extent of the damage caused by the exposure of wheat to ozone.

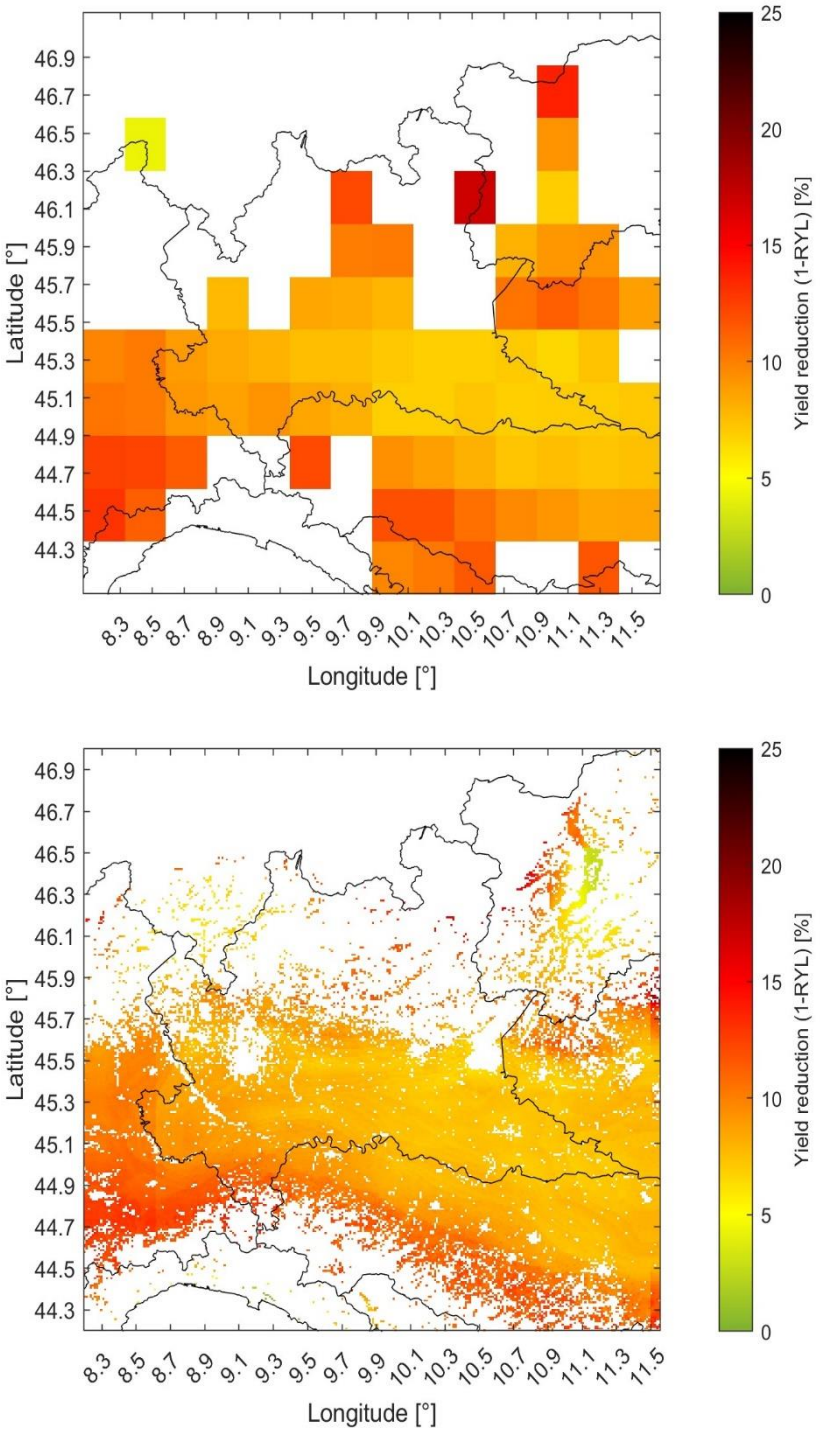

Figure 5.6 - Yield reduction maps for year 2015 (30×30 km² and 1×1 km²)

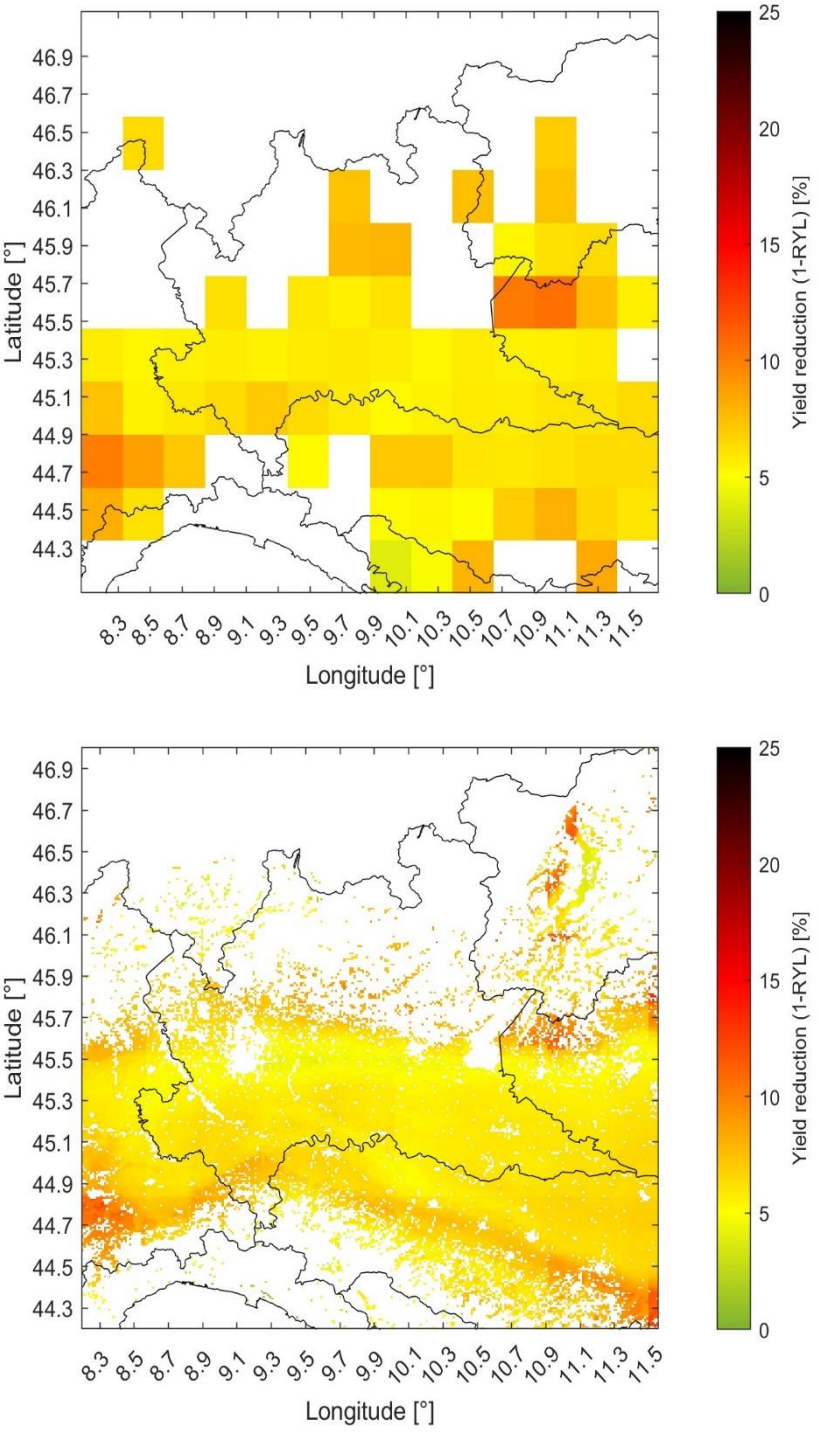

Figure 5.7 - Yield reduction maps for year 2016 (30×30 km² and 1×1 km²)

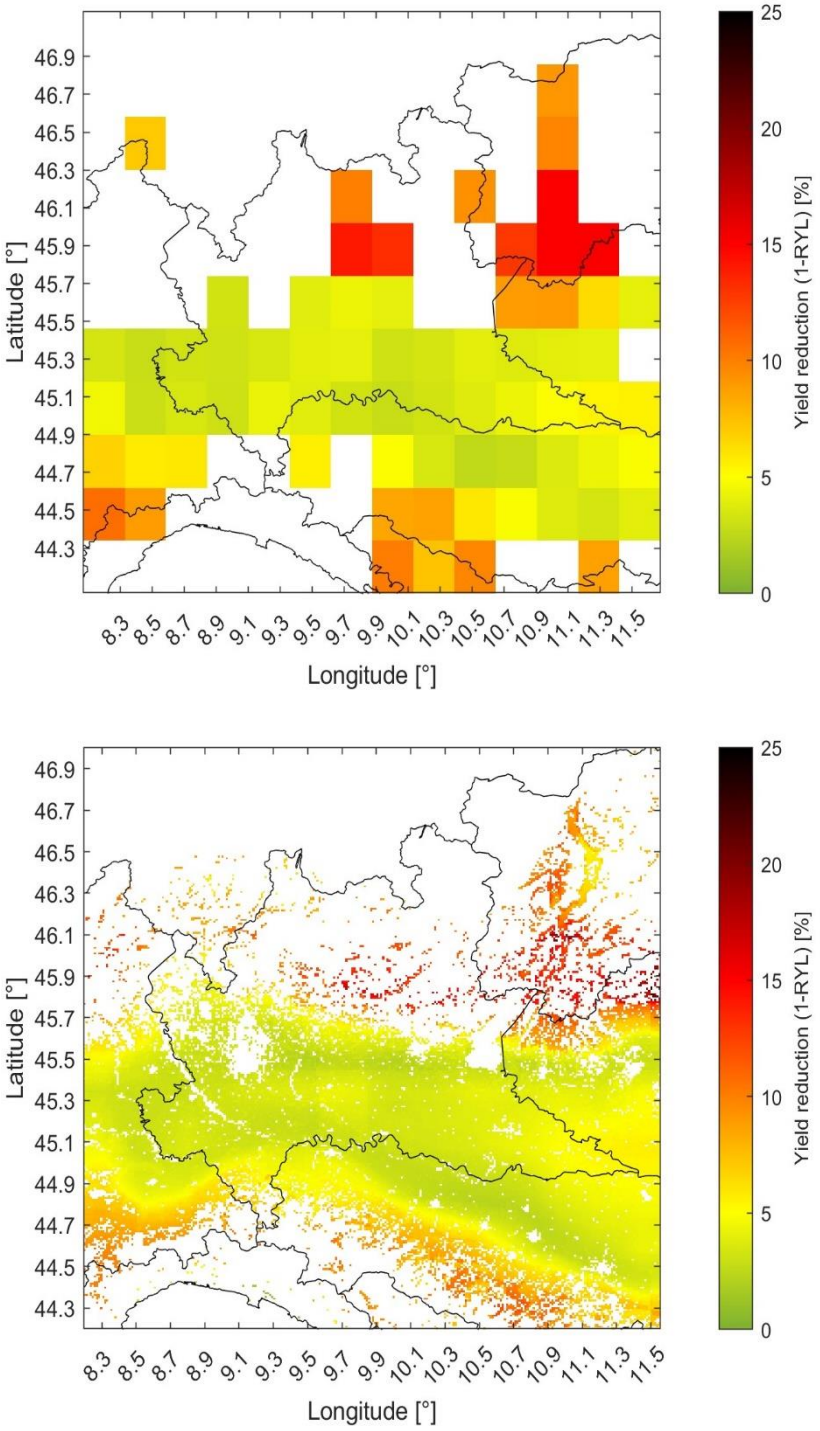

Figure 5.8 - Yield reduction maps for year 2017 (30×30 km² and 1×1 km²)

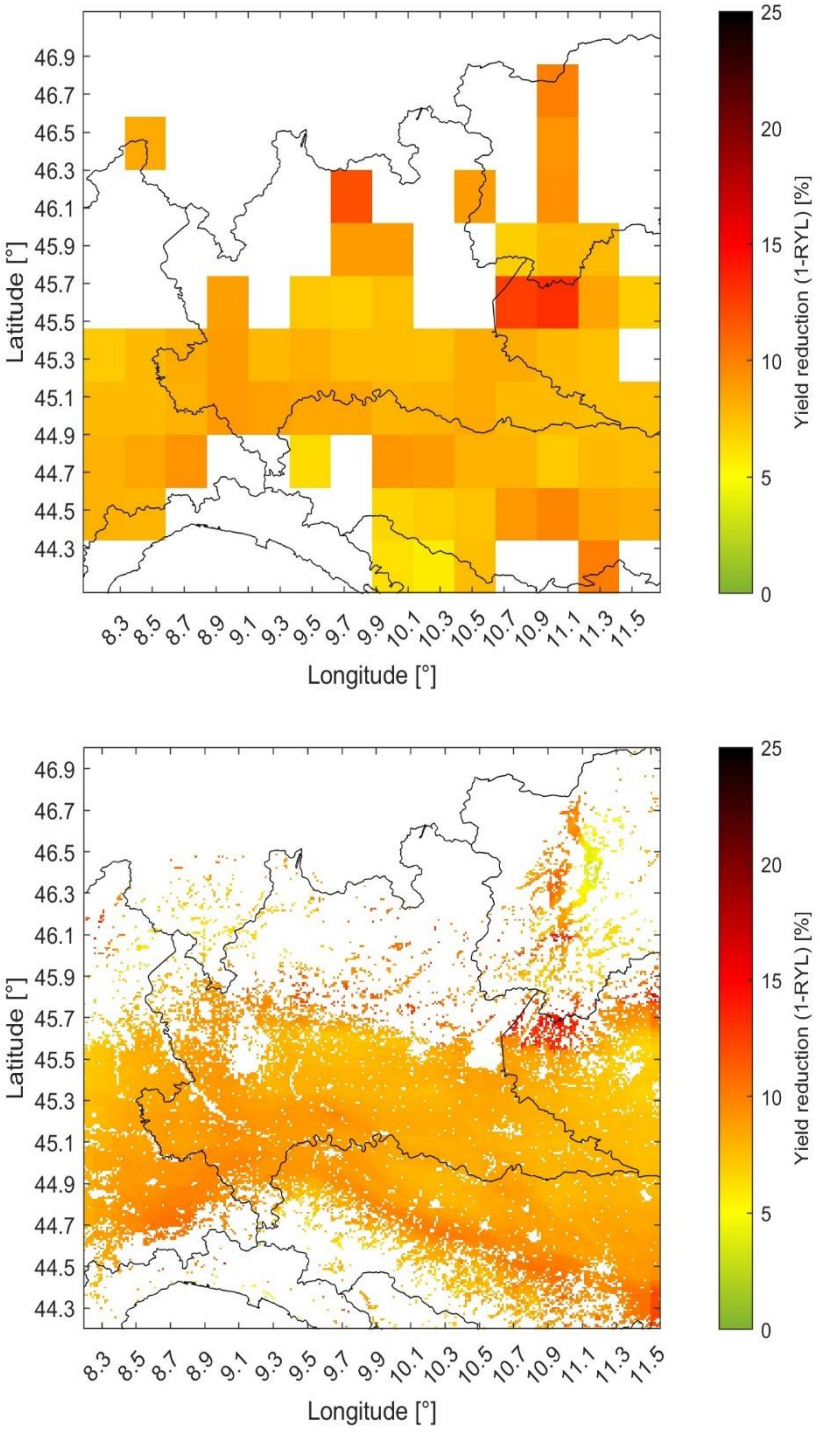

Figure 5.9 - Yield reduction maps for year 2018 (30×30 km² and 1×1 km²)

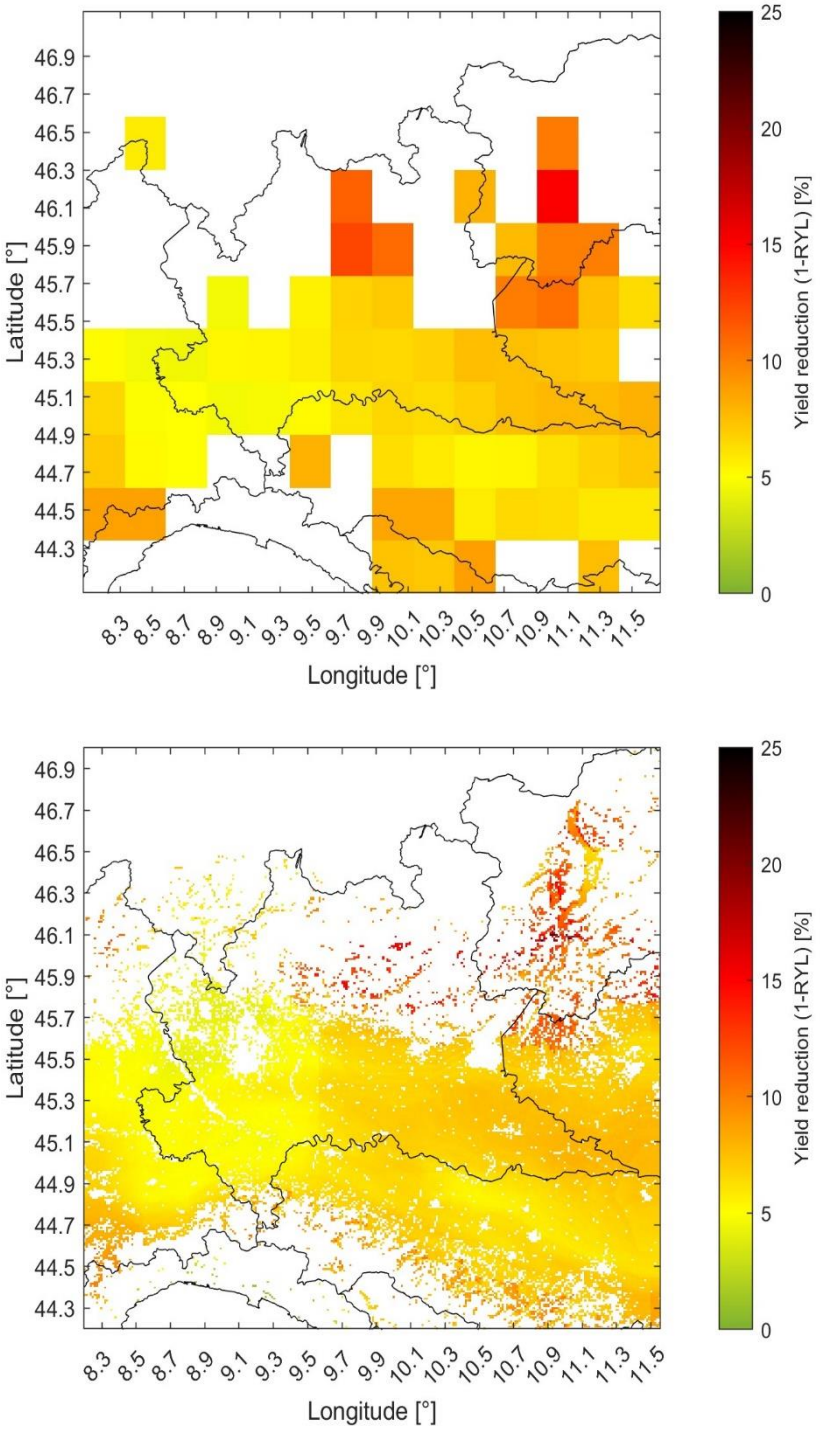

Figure 5.10 - Yield reduction maps for year 2019 (30×30 km² and 1×1 km²)

By analyzing the spatial distribution of YR values within the domain in the various years, it is possible to notice a recurring pattern: on average, the greatest damage is found in the lower part of the domain (corresponding to the hills close to the northern Apennines), in the pre-Alpine areas and in the valley floors, while in the plains the yield reduction values are lower on average. This altitude-related spatial pattern, particularly evident in the parts of the domain with complex orography, was also captured by Guaita et al. (2023) and can be explained by considering the tendency of ozone concentrations to increase with altitude (e.g., Loibl et al., 2004; Chevalier et al., 2007).

Table 5.2 – Annual mean values of meteorological parameters and O_3 at 1 km resolution for cropland grid nodes where winter wheat has reached maturity

Parameter	Year	Spatial annual average	Parameter	Year	Spatial annual average
Precipitation[1] [m]	2015	0.83	Temperature [°C]	2015	12.7
	2016	0.98		2016	12.3
	2017	0.82		2017	12.4
	2018	1.06		2018	12.6
	2019	1.15		2019	12.7
Global radiation[2] [W·m^{-2}]	2015	303			
	2016	300			
	2017	315			
	2018	297			
	2019	303			
Ozone [ppb]	2015	30.0	Relative humidity [%]	2015	72.2
	2016	28.7		2016	73.4
	2017	31.8		2017	69.2
	2018	29.9		2018	75.4
	2019	29.5		2019	72.4

[1] Average of the cumulative values cell by cell

[2] Average value considering only daytime hours

Stomata are essential regulatory structures in plant leaves that play a critical role in balancing water loss and photosynthetic performance. By opening, stomata facilitate the uptake of CO_2 for photosynthesis (but also of O_3), while their closure helps to reduce water loss through transpiration (therefore reducing the ozone uptake). Plants actively regulate stomatal aperture by adjusting the turgor pressure of guard cells, thereby mediating the rates of gas exchange between the leaf interior and the surrounding atmosphere.

Light is a key environmental factor influencing plant growth and development, as it is necessary for photosynthesis and the regulation of physiological processes. Therefore, the precise regulation of stomatal opening in response to light is crucial for plants. As reported by Driesen et al. (2020), light stimulates stomatal opening through two distinct pathways, one driven by blue light and the other by red light (absorbed by different photoreceptors, able to capture light at specific wavelengths). Both blue and red light are considered the primary drivers of stomatal opening, and stomata respond to increasing light intensity by opening, which in turn enhances photosynthetic activity. Light also accelerates transpiration by warming the leaf surface.

Temperature also plays a significant role in stomatal regulation. High temperatures stimulate stomatal opening as part of an adaptive response to facilitate evaporative cooling, thereby protecting the photosynthetic apparatus from heat stress. However, there is a trade-off between heat and drought stress, as high temperatures promote stomatal opening, while drought conditions trigger stomatal closure to conserve water. This interaction highlights the delicate balance between leaf cooling and water use efficiency under varying environmental conditions.
Lower relative humidity indicates drier air, which leads to stomatal closure as a mechanism to prevent excessive water loss. Stomata rapidly respond to air humidity, reducing stomatal conductance (g_s) under low RH to mitigate water loss and protect against desiccation. Thus, stomatal closure in response to lower RH is a crucial adaptive response to high evaporative demand.

Although complex, the influence of meteorological parameters on stomatal behavior, combined with the average annual O_3 concentration, provides a simplified yet plausible explanation for the temporal variability observed in the POD_6 and YR estimates. Factors such as solar radiation, temperature, relative humidity, and precipitation all significantly affect stomatal opening and closing, which in turn regulates ozone uptake by plants. By accounting for these environmental variables, it is possible to understand the variability in ozone exposure and its impact on crop health over the years.

In 2016, the average yield reduction was the smallest, at 6.35%. Analyzing the data, it is evident that, except for relative humidity, which remained at the five-year average, most parameters were unfavorable for high ozone uptake through the stomata. Specifically, 2016 had the lowest average temperature, relatively low radiation, minimal cumulative precipitation, and lower ozone concentrations compared to other years.

In 2017, the yield reduction was modest, with an average of 6.91% across the domain. This year was characterized by low rainfall, lower average temperatures, and reduced relative humidity, conditions that were not conducive to stomatal opening. Despite higher ozone concentrations, the limited stomatal flux resulted in relatively low POD_6 values and thus lower yield reductions compared to more critical years.

In 2018, most parameters were favorable for stomatal opening, except for solar radiation, which was the lowest in the five-year period. Given that light is the primary driver of stomatal opening, the reduced solar radiation likely explains why 2018 was not the most critical year in terms of damage.

The difference in yield reductions between 2015 (average YR = 9.23%) and 2019 (average YR = 7.42%) illustrates that a simplified approach based on annual averages of meteorological parameters and ozone concentrations cannot fully explain the observed damage. This is because ozone uptake through the stomata is a dynamic process, influenced by instantaneous meteorological conditions, and the analysis of annual averages lacks the resolution needed to capture this complexity. Furthermore, it is necessary to consider the meteorological parameters do not act independently of each other and therefore the opening of the stomata depends on the balance between different forcings that act differently moment by moment. Finally, the extent of the damage also depends on when the plant is most exposed to high ozone fluxes: if exposure occurs at the beginning of the growth period, the damage caused will influence the subsequent stages of development of the plant.

5.3 - Estimated economic loss

Table 5.3 shows the average values of POD_6 and reduction in yield (YR) year by year, together with the average ideal wheat production and the estimate of the average quantity of wheat not produced due to the negative effect of ozone and the corresponding economic loss, expressed in terms of reduction in revenues.

Table 5.3 - Estimates of ozone damage in terms of POD_6, reduction in yield and production compared to ideal conditions

Year	POD_6 [mmol·m^{-2} PLA]	YR [%]	$Prod_{att}$ [tonnes]	$Prod_{loss}$ [tonnes]	Rev_{lost} [000 €]
30×30 km^2					
2015	2.47±0.67	9.40±2.56	353,280	33,202	6,464
2016	1.70±0.41	6.46±1.56	405,353	26,180	4,665
2017	1.87±0.94	7.09±3.59	391,040	27,734	5,206
2018	2.13±0.44	8.08±1.68	348,716	28,160	5,581
2019	1.93±0.59	7.34±2.25	327,221	24,011	4,788
1×1 km^2					
2015	2.43±0.59	9.23±2.24	352,612	32,534	6,335
2016	1.67±0.39	6.35±1.46	404,876	25,703	4,580
2017	1.82±0.91	6.91±3.47	390,283	26,977	5,064
2018	2.24±0.41	8.51±1.56	350,355	29,799	5,906
2019	1.95±0.65	7.42±2.47	327,505	24,295	4,844

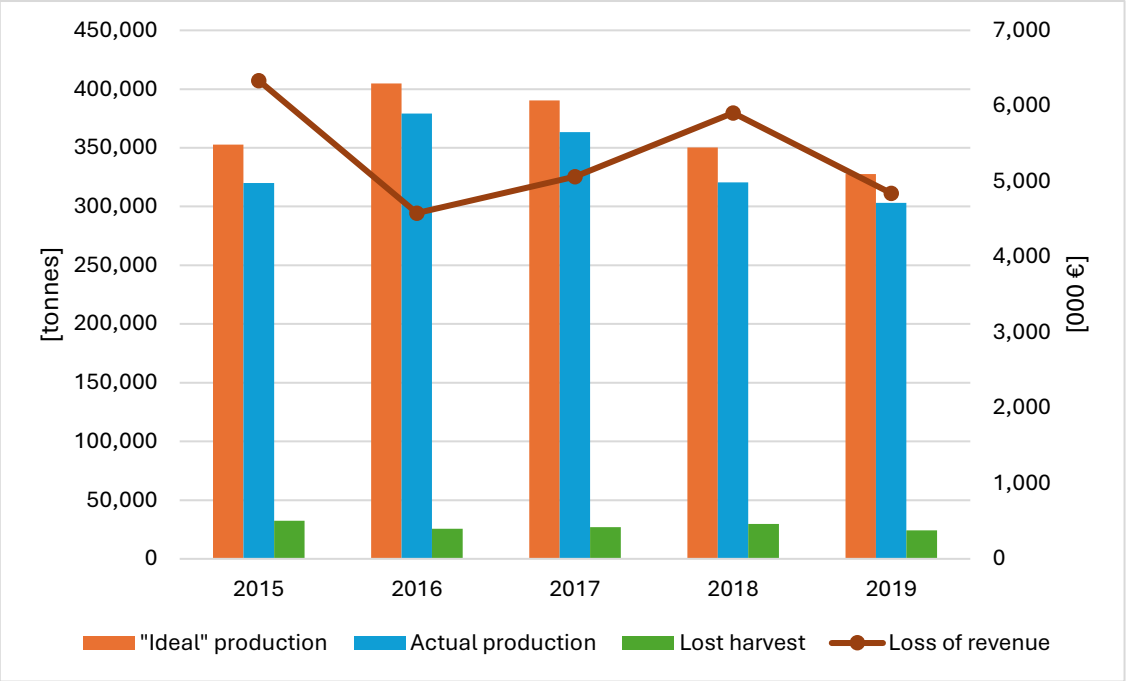

Figure 5.11 - Theoretical production in the absence of ozone damage, actual production and crop losses for the five-year period 2015-2019 (1 km resolution)

The monetary valuation of crop losses based on sales prices proposed in *Subsection 4.4.5* assumes that pollutant damage does not significantly affect crop prices. This approach is commonly used in European and non-European studies. However, as suggested by Schucht et al. (2021), it has limitations. First, reduced crop production could affect market prices, although predicting the direction and extent of this impact is difficult due to the global grain market. Second, production losses do not necessarily equate to economic damages, as resources could be redirected to other activities or adaptive measures could mitigate revenue losses.

In addition to these considerations, the approach based on the overall agricultural production data and the average POD_6 value for the entire domain introduces a further uncertainty: the POD_6 values for each grid cell that, according to the land use map, is intended for agricultural activity have been estimated assuming that only wheat is grown within that area, but this is not always true. Consequently, the average POD_6 value (and therefore damage) calculated for the entire domain could include cells that in reality are not used for wheat cultivation. The inclusion of these areas can lead to an overestimation (in the case of high POD_6) or an underestimation (if the POD_6 value is lower than the average for cells used exclusively for wheat) of the average damage. Obviously, the greater the number of cells in which wheat is not (exclusively) grown, the greater the uncertainty in the estimate of production and revenue losses.

Despite these considerations, it can still be stated that the results obtained in terms of economic damage are able to provide relevant information in the context of decision-making processes and to inform stakeholders and local communities on problems related to air pollution in general, and specifically on the processes that lead to the formation of ozone in the troposphere.

6. Conclusions

Ozone pollution poses a significant threat to vegetation, with its detrimental effects on crop yields, food security, and ecosystem health widely recognized. Since the Industrial Revolution, surface O_3 levels have increased dramatically, by approximately 60-100% (Vingarzan, 2004; Sitch et al., 2007), largely due to rising emissions of methane (CH_4), volatile organic compounds (VOCs), and nitrogen oxides (NO_X). Meteorological changes, such as higher temperatures, further exacerbate this issue by promoting ozone formation. The resulting increase in tropospheric O_3 is a growing concern for global crop yields, with lasting negative impacts on food security anticipated (Mills et al., 2018; Ainsworth et al., 2020). Extensive studies have highlighted the effectiveness of using the Phytotoxic Ozone Dose (POD_Y) in assessing ozone risk, especially for crops like wheat, where POD_Y has shown a strong correlation between O_3 exposure and observed reductions in grain yield (Pleijel et al., 2007).
Between 2018 and 2022, winter wheat (*Triticum aestivum*) accounted for an average of 16.5% of Lombardy's cereal cropland, making it the second most cultivated cereal after maize (ISTAT, 2023). Given its economic importance and sensitivity to ozone, winter wheat serves as an ideal model crop for O_3 risk assessment, particularly within the European context. This focus allows for a more targeted evaluation of ozone's impact on regional agriculture and food security.

The main limitation of studies conducted thus far to estimate ozone damage to winter wheat is the need to collect data for the parameters required to calculate POD_6 from monitoring stations within the region of interest, that must then be spatially interpolated using specific techniques (e.g., Kriging), or derived from regional climate models specifically designed for this purpose.
The difficulty in acquiring a large volume of measured data from ground-based sensors, due to the limited capacity of the data request systems provided by authorities (a consideration that applies at least in the case of Italy), and the uncertainty related to the spatial interpolation of observed data (particularly in areas with complex topography and regions with a limited number of monitoring stations), make damage estimation approaches based on measured data of limited applicability.
As for the use of regional climate models that include the simulation of chemical processes, their application is constrained by the availability of sufficient computational resources. Furthermore, the results obtained from these simulations are not publicly accessible.

The approach proposed in this study is based on the use of publicly and freely available reanalysis data. Compared to meteorological parameters measured by ground stations, reanalysis model data provide continuous spatial and temporal coverage for any domain, regardless of the availability of monitoring sensors within it. Additionally, unlike regional climate models, the values for parameters of interest are available globally with high temporal resolution and adequate spatial resolution for extended periods (ERA5 provides data from 1940 onwards), without the need for extensive computational resources. The limitation of using reanalysis data (specifically ERA5), which emerged during the study, relates to the representation and description of atmospheric chemical processes in the model, as the ozone values provided do not adequately reflect reality. However, it was demonstrated that by using ground-measured ozone concentrations and applying a Random Forest model, reliable estimates can be obtained using ERA5 meteorological parameters as inputs.
By applying a dual-sink big-leaf model to data for the period 2015-2019, this study was able to capture the extent of interannual variability in ozone damage to vegetation, with average POD_6 values for the entire domain ranging from 1.67 $mmol \cdot m^{-2}$ PLA to 2.43 $mmol \cdot m^{-2}$ PLA, corresponding to yield reductions of 6.4% and 9.2%, respectively. The use of higher spatial resolution data made it possible to capture the spatial distribution of damage in greater detail and to identify the presence of hotspots, points where the damage is significantly higher than the surrounding areas.

The economic losses calculated based on the POD_6 estimates reveal that ozone damage reduces wheat sales revenue by millions of euros each year. This finding highlights the need to mitigate the negative effects of ozone on vegetation by developing national and international strategies to reduce precursor emissions and develop ozone-tolerant crop varieties, especially as climate change exacerbates the problem.

Based on the results of this study, potential future developments are:

- The inclusion of other crops in the simulation to estimate the overall damage to agriculture, possible by providing adequate parameterization of stomatal conductance and plants' geometry.

- The development of adaptation and mitigation scenarios, such as modifying ozone values to simulate a reduction in precursor emissions or adjusting crop parameters to account for the reduced sensitivity of new varieties to ozone exposure.

- The application of the proposed approach to other regions, considering however the need to have reliable ozone values available and that the parameterizations could be different from those adopted in this study

References

Adam-Poupart A., Brand A., Fournier M., Jerrett M., Smargiassi A., Spatiotemporal modeling of ozone levels in Quebec (Canada): A comparison of Kriging land-use regression (LUR) and combined Bayesian maximum entropy–LUR approaches, Environ. Health Perspective, vol. 122, no. 9, pp. 970-976, 2014.
DOI: 10.1289/ehp.1306566

Agathokleous E., Feng Z., Oksanen E., Sicard P., Wang Q., Saitanis C.J., Araminiene V., Blande J. D., Hayes F., Calatayud V., Domingos M., Veresoglou S.D., Peñuelas J., Wardle D.A., Marco A.D., Li Z., Harmens H., Yuan X., Vitale M., Paoletti E., Ozone affects plant, insect, and soil microbial communities: A threat to terrestrial ecosystems and biodiversity, Sci. Adv., 6, eabc1176, 2020.
DOI: 10.1126/sciadv.abc1176

Ainsworth E.A, Lemonnier P., Wedow J.M., The influence of rising tropospheric carbon dioxide and ozone on plant productivity. Plant Biol (Stuttg), 2020.
DOI: 10.1111/plb.12973

Audran G., Marque S.R.A., Santelli M., Ozone, chemical reactivity and biological functions. Tetrahedron, 74 (43), pp.6221-6261, 2018.
DOI: 10.1016/j.tet.2018.09.023

Avnery S., Mauzerall D.L., Liu J., Horowitz L.W., Global crop yield reductions due to surface ozone exposure: 1. Year 2000 crop production losses and economic damage, Atmospheric Environment, Volume 45, Issue 13, Pages 2284-2296, 2011.
DOI: 10.1016/j.atmosenv.2010.11.045

Barnes J., Zheng Y., Lyons T., Plant Resistance to Ozone: The Role of Ascorbate. In: Omasa, K., Saji, H., Youssefian, S., Kondo, N. (eds) Air Pollution and Plant Biotechnology. Springer, Tokyo, 2002.
DOI: 10.1007/978-4-431-68388-9_12

Baruth B., Biavetti I., Bussay A., Ceglar A., De Sanctis G., Garcia Condado S., Karetsos S., Lecerf R., Lopez Lozano R., Nisini Scacchiafichi L., Panarello L., Seguini L., Toreti A., Van Den Berg M., Van Der Velde M., JRC MARS Bulletin Vol. 24 No 8 - Crop monitoring in Europe, August 2016: Winter cereals back to five-year average. EUR 24736 EN. Luxembourg (Luxembourg): Publications Office of the European Union; 2016. JRC104174.
https://publications.jrc.ec.europa.eu/repository/handle/JRC104174

Berman J.D., Breysse P.N., White R.H., Waugh D.W., Curriero F.C., Evaluating methods for spatial mapping: Applications for estimating ozone concentrations across the contiguous United States, Environ. Technol. Innov., vol. 3, pp. 1-10, 2015.
DOI: 10.1016/j.eti.2014.10.003

Biancofiore F., Verdecchia M., Di Carlo P., Tomassetti B., Aruffo E., Busilacchio M., Bianco S., Di Tommaso S., Colangeli C., Analysis of surface ozone using a recurrent neural network, Science of The Total Environment, Volume 514, Pages 379-387, 2015.
DOI: 10.1016/j.scitotenv.2015.01.106

Biswas D.K., Jiang G.M., Differential drought-induced modulation of ozone tolerance in winter wheat species, Journal of Experimental Botany, Volume 62, Issue 12, Pages 4153–4162, 2011.
DOI: 10.1093/jxb/err104

Bonan G., Climate Change and Terrestrial Ecosystem Modeling. Cambridge University Press, Boulder, 2019.
DOI: 10.1017/9781107339217

Borg H., Grimes D.W., Depth development of roots with time: An empirical description. Transactions of the ASAE Vol. 29 (1): 194-197, 1986.
DOI: 10.13031/2013.30125

Botti D., A phytoclimatic map of Europe. Cybergeo: European Journal of Geography, Environnement, Nature, Paysage, document 867, 2018.
DOI: 10.4000/cybergeo.29495

Broberg M.C., Daun S., Pleijel H., Ozone Induced Loss of Seed Protein Accumulation Is Larger in Soybean than in Wheat and Rice. Agronomy 10, 357, 2020.
DOI: 10.3390/agronomy10030357

Brutsaert W., Chapter 5: the surface roughness parameterization. In: Brutsaert, W. (Ed.), Evaporation into the Atmosphere. Springer, Dordrecht, pp. 113–116, 1982.
DOI: 10.1007/978-94-017-1497-6

Büker P., Morrissey T., Briolat A., Falk R., Simpson D., Tuovinen J.P., Alonso R., Barth S., Baumgarten M., Grulke N., Karlsson P. E., King J., Lagergren F., Matyssek R., Nunn A., Ogaya R., Peñuelas J., Rhea L., Schaub M., Uddling J., Werner W., Emberson L.D., DO_3SE modelling of soil moisture to determine ozone flux to forest trees, Atmos. Chem. Phys., 12, 5537–5562, 2012.
DOI: 10.5194/acp-12-5537-2012

Campbell G.S., Norman J.M., An Introduction to Environmental Biophysics, Second ed. Springer, New York, 1998.
DOI: 10.1007/978-1-4612-1626-1

Chevalier A., Gheusi F., Delmas R., Ordóñez C., Sarrat C., Zbinden R., Thouret V., Athier G., Cousin J.M., Influence of altitude on ozone levels and variability in the lower troposphere: a ground-based study for western Europe over the period 2001–2004. Atmos. Chem. Phys. 7, 4311–4326, 2007.
DOI: 10.5194/acp-7-4311-2007

Coates J., Mar K.A., Ojha N., Butler T.M., The influence of temperature on ozone production under varying NOx conditions – a modelling study, Atmos. Chem. Phys., 16, 11601–11615, 2016.
DOI: 10.5194/acp-16-11601-2016

Cox W.M., Chu S.H., Assessment of interannual ozone variation in urban areas from a climatological perspective, Atmospheric Environment, vol. 30, no. 14, pp. 2615–2625, 1996.
DOI: 10.1016/1352-2310(95)00346-0

Driesen E., Van den Ende W., De Proft M., Saeys W., Influence of Environmental Factors Light, CO_2, Temperature, and Relative Humidity on Stomatal Opening and Development: A Review. Agronomy, 10(12):1975, 2020.
DOI: 10.3390/agronomy10121975

Emberson L.D., Ashmore M.R., Cambridge H.M., Simpson D., Tuovinen J.P., Modelling stomatal ozone flux across Europe. Environ. Pollut. 109, 403–413, 2000.
DOI: 10.1016/s0269-7491(00)00043-9

Emberson L., Ashmore M.R., Murray F., Kuylenstierna J.C.I., Percy K.E., Izuta T., Zheng Y., Shimizu H., Sheu B.H., Liu C.P., Agrawal M., Wahid A., Abdel-Latif N.M., van Tienhoven M., de Bauer L.I., Domingos M., Impacts of Air Pollutants on Vegetation in Developing Countries. Water, Air, & Soil Pollution 130, 107–118, 2001.
DOI: 10.1023/A:1012251503358

Emberson L.D., Büker P., Ashmore M.R., Assessing the risk caused by ground level ozone to European forest trees: A case study in pine, beech and oak across different climate regions, Environmental Pollution, Volume 147, Issue 3, Pages 454-466, 2007.
DOI: 10.1016/j.envpol.2006.10.026

Emberson L.D., Pleijel H., Ainsworth E.A., van den Berg M., Ren W., Osborne S., Mills G., Pandey D., Dentener F., Büker P., Ewert F., Koeble R., Van Dingenen R., Ozone effects on crops and consideration in crop models, European Journal of Agronomy, Volume 100, Pages 19-34, 2018.
DOI: 10.1016/j.eja.2018.06.002

Emberson L., Effects of ozone on agriculture, forests and grasslands. Phil Trans R Soc A 378:20190327, 2020.
DOI: 10.1098/rsta.2019.0327

Eurostat, Selling prices of crop products (absolute prices) - annual price (from 2000 onwards).
DOI: 10.2908/APRI_AP_CRPOUTA

Fan J., McConkey B., Wang H., Janzen H., Root distribution by depth for temperate agricultural crops. Field Crop. Res. 189, 68–74, 2016.
DOI: 10.1016/j.fcr.2016.02.013

Feng Z., Kobayashi K., Wang X., Feng Z.W., A meta-analysis of responses of wheat yield formation to elevated ozone concentration. Chin. Sci. Bull. 54, 249–255, 2009.
DOI: 10.1007/s11434-008-0552-6

Feng Z., Pang J., Nouchi I., Kobayashi K., Yamakawa T., Zhu J., Apoplastic ascorbate contributes to the differential ozone sensitivity of two varieties of winter wheat under fully open-air field conditions. Environ Pollut 158:3539–3545, 2010.
DOI: 10.1016/j.envpol.2010.08.019

Foyer H.C., Kyndt T., Hancock D.R., Vitamin C in plants: novel concepts new perspectives and outstanding issues. Antioxid Redox Sign 32(7):463–485, 2020.
DOI: 10.1089/ars.2019.7819

Frei M., Tanaka J.P., Chen C., Wissuwa M., Mechanisms of ozone tolerance in rice: characterization of two QTLs affecting leaf bronzing by gene expression profiling and biochemical analyses. J Exp Bot 61:1405–1417, 2010.
DOI: 10.1093/jxb/erq007

Gerosa G., Marzuoli R., Monteleone B., Chiesa M., Finco A., Vertical ozone gradients above forests. Comparison of different calculation options with direct ozone measurements above a mature forest and consequences for ozone risk assessment. Forests 8(9), 337, 2017.
DOI: 10.3390/f8090337

Gillespie C., Stabler D., Tallentire E., Goumenaki E., Barnes J., Exposure to environmentally-relevant levels of ozone negatively influence pollen and fruit development. Environ Pollut 206:494–501, 2015.
DOI: 10.1016/j.envpol.2015.08.003

González-Fernández I., Bermejo V., Elvira S., de la Torre D., González A., Navarrete L., Alonso R., Modelling ozone stomatal flux of wheat under mediterranean conditions. Atmos. Environ. 67, 149–160, 2013.
DOI: 10.1016/j.atmosenv.2012.10.043

Goumenaki E., González-Fernández I., Barnes J.D., Ozone uptake at night is more damaging to plants than equivalent day-time flux. Planta 253, 75, 2021.
DOI: 10.1007/s00425-021-03580-w

Grulke N.E., Heath R.L., Ozone effects on plants in natural ecosystems. Plant Biol 22(S1):12–37, 2020.
DOI: DOI.org/10.1111/plb.12971

Guaita P.R., Marzuoli R., Gerosa G.A., A regional scale flux-based O3 risk assessment for winter wheat in northern Italy, and effects of different spatio-temporal resolutions, Environmental Pollution, Volume 333, 2023, 121860.
DOI: 10.1016/j.envpol.2023.121860

Guderian R., Air pollution by photochemical oxidants. Formation, transport, control and effects on plants. Ecological Studies, Vol. 52. Springer Verlag, Berlin, 1985.
DOI: 10.1007/978-3-642-70118-4

Hanna S.R., Chang J.C., Boundary-layer parameterizations for applied dispersion modeling over urban areas. Boundary-Layer Meteorol. 58, 229–259, 1992.
DOI: 10.1007/BF02033826

Hanna S.R., Paine R.J., Hybrid plume dispersion model (HPDM) development and evaluation. J. Appl. Meteorol. 28, 206–224, 1993.
DOI: 10.1175/1520-0450(1989)028<0206:HPDMDA>2.0.CO;2

Harmens H., Mills G., Ozone Pollution: Impacts on carbon sequestration in Europe. ICP Vegetation Report, 2012

Hayes F., Sharps K., Harmens H., Roberts I., Mills G., Tropospheric ozone pollution reduces the yield of African crops. J Agro Crop Sci. 2020; 206: 214–228.
DOI: 10.1111/jac.12376

Heck W.W., Clifton Taylor O., Tingey D.T., Assessment of Crop Loss from Air Pollutants. Elsevier Science Publishers Ltd, London,1988.
DOI: https://DOI.org/10.1007/978- 94-009-1367-7

Hicks B.B., Baldocchi D.D., Meyers T.P., Hosker Jr. R.P., Matt D.R., A preliminary multiple resistance routine for deriving dry deposition velocities from measured quantities. Water Air Soil Pollut 36, 311–330, 1987.
DOI: 10.1007/BF00229675

Holtslag A.A., Van Ulden A.P., A simple scheme for daytime estimates of the surface fluxes from routine weather data. J. Clim. Appl. Meteorol. 22, 517–529, 1983.
https://doi.org/10.1175/1520-0450(1983)022<0517:ASSFDE>2.0.CO;2

Horálek J., Schreiberová M., Vlasáková L., Marková J., Tognet F., Schneider P., Kurfürst P., Schovánková J., European air quality maps for 2018, PM10, PM2.5, Ozone, NO2 and NOx Spatial estimates and their uncertainties, Eionet Report - ETC/ATNI 2020/10, 2020.

Hoshika Y., De Marco A., Materassi A., Paoletti E., Light intensity affects ozone-induced stomatal sluggishness in snapbean. Water Air Soil Poll 227:419, 2016.
DOI: 10.1007/s11270-016-3127-1

Hoshika Y., Carrari E., Zhang L., Carriero, G., Pignatelli S., Fasano G., Materassi A., Testing a ratio of photosynthesis to O_3 uptake as an index for assessing O_3-induced foliar visible injury in poplar trees. Environ Sci Pollut Res 25, 8113–8124, 2018a.
DOI: 10.1007/s11356-017-9475-6

Hoshika Y., Moura B., Paoletti E., Ozone risk assessment in three oak species as affected by soil water availability, Environ Sci Pollut Res 25, 8125–8136, 2018b.
DOI: 10.1007/s11356-017-9786-7

I.Stat, Crops: Areas and production - overall data. Last access: September 2024
Link: http://dati.istat.it/Index.aspx?QueryId=37850&lang=en#

Jarvi P.G., The interpretation of the variations in leaf water potential and stomatal conductance found in canopies in the field. Philos. Trans. R. Soc. Lond. B Biol. Sci. 273, 593–610, 1976.
https://doi.org/10.1098/rstb.1976.0035

Jolivet Y., Bagard M., Cabané M., Vaultier M.N., Gandin A., Afif D., Dizengremel P., Le Thiec D., Deciphering the ozone-induced changes in cellular processes: a prerequisite for ozone risk assessment at the tree and forest levels. Annals of Forest Science 73, 923–943, 2016.
DOI: 10.1007/s13595-016-0580-3

Juarez E.K., Petersen M.R., A Comparison of Machine Learning Methods to Forecast Tropospheric Ozone Levels in Delhi. Atmosphere, 13, 46, 2022.
DOI: 10.3390/atmos13010046

Koblick D.C., 2024. Vectorized Solar Azimuth and Elevation Estimation, MATLAB Central File Exchange.
Link: https://www.mathworks.com/matlabcentral/fileexchange/23051-vectorized-solar-azimuth-and-elevation-estimation

Lefohn A.S., Malley C.S., Smith L., Wells B., Hazucha M., Simon H., Naik V., Mills G., Schultz M.G., Paoletti E., De Marco A., Xu X., Zhang L., Wang T., Neufeld H.S., Musselman R.C., Tarasick D., Brauer M., Feng Z., Tang H., Kobayashi K., Sicard P., Solberg S., Gerosa G., Tropospheric ozone assessment report: Global ozone metrics for climate change, human health, and crop/ecosystem research. Elementa (Wash D C), 2018.
DOI: 10.1525/elementa.279

Lesser V.M., Rawlings J.O., Spruill S.E., Somerville M.C., Ozone Effects on Agricultural Crops: Statistical Methodologies and Estimated Dose-Response Relationships. Crop Science, 30: 148-155, 1990.
DOI: 10.2135/cropsci1990.0011183X003000010033x

Loibl W., Bolhàr-Nordenkampf H.R., Herman F., Smidt S., Modelling critical levels of ozone for the forested area of Austria. Modifications of the AOT40 concept. Environ Sci Pollut Res Int, 11(3):171-80, 2004.
DOI: 10.1007/BF02979672

Loya N., Olmos Pineda I., Pinto D., Gómez-Adorno H., Alemán Y., Forecast of Air Quality Based on Ozone by Decision Trees and Neural Networks. In: Batyrshin, I., González Mendoza, M. (eds) Advances in Artificial Intelligence. MICAI 2012. Lecture Notes in Computer Science, vol 7629. Springer, Berlin, Heidelberg, 2013.
DOI: 10.1007/978-3-642-37807-2_9

Maranzano P., Algieri A., ARPALData: an R package for retrieving and analyzing air quality and weather data from ARPA Lombardia (Italy). Environ Ecol Stat 31, 187–218, 2024.
https://doi.org/10.1007/s10651-024-00599-6

Massman W.J., A review of the molecular diffusivities of H2O, CO2, CH4, CO, O3, SO2, NH3, N2O, NO, AND NO2 in air, O2 and N2 near STP. Atmos. Environ. 32, 1111–1127, 1998.

McNaughton K.G., Van Den Hurk B.J., A 'Lagrangian' revision of the resistors in the two-layer model for calculating the energy budget of a plant canopy. BoundaryLayer Meteorol. 74, 261–288, 1995.
https://doi.org/10.1007/BF00712121.

Mills G., Buse A., Gimeno B., Bermejo V., Holland M., Emberson L., Pleijel H., A synthesis of AOT40-based response functions and critical levels of ozone for agricultural and horticultural crops. Atmospheric Environment, 41(12), 2630-2643, 2007.
DOI: 10.1016/j.atmosenv.2006.11.016

Mills G., Wagg S., Harmens H., Ozone pollution: impacts on ecosystem services and biodiversity. Bangor, UK, NERC/Centre for Ecology & Hydrology, 104pp, eds. 2013.

Mills G., Pleijel H., Malley S.C., Sinha B., Cooper R.O., Schultz G.M., Neufeld S.H., Simpson D., Sharps K., Feng Z., Gerosa G., Harmens H., Kobayashi K., Saxena P., Paoletti E., Sinha V., Xu X., Tropospheric ozone assessment report: present-day tropospheric ozone distribution and trends relevant to vegetation. Elem Sci Anth 6:47, 2018.
DOI: 10.1525/elementa.302

Mintz Y., Walker G.K., Global fields of soil moisture and land surface evapotranspiration derived from observed precipitation and surface air temperature. J. Appl. Meteorol. 32, 1305–1334, 1993.
DOI: 10.1175/1520-0450(1993)032<1305:GFOSMA>2.0.CO;2

Monin A.S., Obukhov A.M., Osnovnye zakonomernosti turbulentnogo peremesivanija v prizemnom sloe atmosfery (Basic laws of turbulent mixing in the atmosphere near the ground). Trudy geofiz inst AN SSSR 151 (24), 163–187, 1954.

Monks P.S., Archibald A.T., Colette A., Cooper O., Coyle M., Derwent R., Fowler D., Granier C., Law K.S., Mills G.E., Stevenson D.S., Tarasova O., Thouret V., von Schneidemesser E., Sommariva R., Wild O., Williams M.L., Tropospheric ozone and its precursors from the urban to the global scale from air quality to short-lived climate forcer, Atmos. Chem. Phys., 15, 8889–8973, 2015.
DOI: 10.5194/acp-15-8889-2015

Monteith, J.L., 1965. Evaporation and Environment, vol. 19. Symposia of the Society for Experimental Biology, pp. 205–234.

Monteith J.L., Unsworth M.H., Principles of Environmental Physics, Fourth ed. Elsevier, Oxford, 2014.

Murray F.W., On the computation of saturation vapor pressure. J. Appl. Meteorol. 6, 203–204, 1967.
DOI: 10.1175/1520-0450(1967)006<0203:OTCOSV>2.0.CO;2

Naveen S., Upamanyu M.S., Chakki K., Chandan M., Hariprasad P., Air Quality Prediction Based on Decision Tree Using Machine Learning, 2023 International Conference on Smart Systems for applications in Electrical Sciences (ICSSES), Tumakuru, India, pp. 1-6, 2023.
DOI: 10.1109/ICSSES58299.2023.10200535

Noctor G, Reichheld J.P., Foyer C.H., ROS-related redox regulation and signaling in plants. Semin Cell Dev Biol., 2018.
DOI: 10.1016/j.semcdb.2017.07.013

Norman J.M., Simulation of microclimates. In: Hatfield, J.L., Thomason, I.J. (Eds.), Biometeorology in Integrated Pests Management. Academic Press, New York, pp. 65–99, 1982.

Ntagkas N., Wolteringa E.J., Marcelis L.F.M., Light regulates ascorbate in plants: an integrated view on physiology and biochemistry. Environ Exp Bot 147:271–280, 2018.
DOI: 10.1016/j.envexpbot.2017.10.009

Osborne S.A., Mills G., Hayes F., Ainsworth E.A., Büker P., Emberson L., Has the sensitivity of soybean cultivars to ozone pollution increased with time? An analysis of published dose–response data. Glob Change Biol, 22: 3097-3111, 2016.
DOI: https://DOI.org/10.1111/gcb.13318

Padu E., Kollist H., Tulva I., Oksanen E., Moldau H., Components of apoplastic ascorbate use in Betula pendula leaves exposed to CO_2 and O_3 enrichment. New Phytol 165:131–142, 2005.
DOI: 10.1111/j.1469-8137.2004.01220.x

Pignocchi C., Kiddle G., Hernandez I., Foster S.J., Asensi A., Taybi T., Barnes J.D., Foyer C.H., Ascorbate-oxidase-dependent changes in the redox state of the apoplast modulate gene transcription leading to modified hormone signaling and orchestration of defense processes in tobacco. Plant Physiol 141:423–435, 2006.
DOI: 10.1104/pp.106.078469

Pleijel H., Broberg M.C., Uddling J., Mills G., Current surface ozone concentrations significantly decrease wheat growth, yield and quality. Science of The Total Environment, Volumes 613–614, Pages 687-692, 2018.
DOI: 10.1016/j.scitotenv.2017.09.111

Pleijel H., Danielsson H., Broberg M.C., Benefits of the Phytotoxic Ozone Dose (POD) index in dose-response functions for wheat yield loss. Atmos. Environ. 268, 118797, 2022.
DOI: 10.1016/j.atmosenv.2021.118797

Sager J.C., Tibbits T.W., CHAPTER 1 - Radiation. In: Langhans, R.W., Tibbits, T.W. (Eds.), Plant Growth Chamber Handbook. North Central Regional Research Publication, pp. 1–30. No. 340, Iowa Agriculture and Home Economics Experiment Station Special Report No. 99, 1997.
https://www.controlledenvironments.org/growth-chamber-handbook/

Sanmartin M., Drogoudi P.D., Lyons T., Pateraki I., Barnes J., Kanellis A.K., Over-expression of ascorbate oxidase in the apoplast of transgenic tobacco results in altered ascorbate and glutathione redox states and increased sensitivity to ozone. Planta 216, 918–928, 2003.
DOI: 10.1007/s00425-002-0944-9

Schultz M.G., Schröder S., Lyapina O., Cooper O.R., Galbally I., Petropavlovskikh I., von Schneidemesser E., Tanimoto H., Elshorbany Y., Naja M., Seguel R.J., Dauert U., Eckhardt P., Feigenspan,S., Fiebig M., Hjellbrekke Anne-Gunn, Hong You-Deog, Kjeld P.C., Koide H., Lear G., Tarasick D., Ueno M., Wallasch M., Baumgardner D., Chuang Ming-Tung, Gillett R., Lee M., Molloy S., Moolla R., Wang T., Sharps K., Adame J.A., Ancellet G., Apadula F., Artaxo P., Barlasina M.E., Bogucka M., Bonasoni P., Chang L., Colomb A., Cuevas-Agulló E., Cupeiro M., Degorska A., Ding A., Fröhlich M., Frolova M., Gadhavi H., Gheusi F., Gilge S., Gonzalez M.Y., Gros V., Hamad S.H., Helmig D., Henriques D., Hermansen O., Holla R., Hueber J., Im U., Jaffe D.A., Komala N., Kubistin D., Lam Ka-Se, Laurila T., Lee H., Levy I., Mazzoleni C., Mazzoleni L.R., McClure-Begley A., Maznorizan M., Murovec M., Navarro-Comas M., Nicodim F., Parrish D., Read K.A., Reid N., Ries L., Saxena P., Schwab J.J., Scorgie Y., Senik I., Simmonds P., Sinha V., Skorokhod A.I., Spain G., Spangl W., Spoor R., Springston S.R., Steer K., Steinbacher M., Suharguniyawan E., Torre P., Trickl T., Weili L., Weller R., Xiaobin X., Xue L., Zhiqiang M., Tropospheric Ozone Assessment Report: Database and metrics data of global surface ozone observations. Elementa: Science of the Anthropocene 1, 5 58, 2017.
DOI: 10.1525/elementa.244

Schucht S., Tognet F., Létinois L., Wheat yield loss in 2019 in Europe due to ozone exposure, Eionet Report - ETC/ATNI 2021/17, 2021.

Sellers P.J., Randall D.A., Collatz G.J., Berry J.A., Field C.B., Dazlich D.A., Zhang C., Collelo G.D., Bounoua L., A revised land surface parametrization (SiB2) for atmospheric GCMs. Part I: model formulation. J. Clim. 9, 676–705, 1996.
DOI: 10.1175/1520-0442(1996)009<0676:ARLSPF>2.0.CO;2

Shi X., Zhao C., Jiang J.H., Wang C., Yang X., Yung Y.L., Spatial representativeness of PM 2.5 concentrations obtained using observations from network stations, J. Geophys. Res. Atmos., vol. 123, no. 6, pp. 3145-3158, 2018.
DOI: 10.1002/2017JD027913

Shindell D.T., Crop yield changes induced by emissions of individual climate-altering pollutants. Earth's Future, 4: 373-380, 2016.
DOI: 10.1002/2016EF000377

Singh A.A., Agrawal S.B., Tropospheric ozone pollution in India: effects on crop yield and product quality. Environ Sci Pollut Res 24, 4367–4382, 2017.
DOI: 10.1007/s11356-016-8178-8

Sitch S., Cox P., Collins W., Huntingford C., Indirect radiative forcing of climate change through ozone effects on the land-carbon sink, Nature, 448, 791-794, 2007.
DOI: 10.1038/nature06059

Tai A.P.K., Sadiq M., Pang J.Y.S., Yung D.H.Y., Feng Z., Impacts of Surface Ozone Pollution on Global Crop Yields: Comparing Different Ozone Exposure Metrics and Incorporating Co-effects of CO2. Frontiers in Sustainable Food Systems, vol. 5, 2021
DOI: 10.3389/fsufs.2021.534616

Tetens O., Über einige meteorologische Begrifle. Z. Geophys., vol. 6, 297-309, 1930.

Uddling J., Pleijel H., Karlsson P.E., Measuring and modelling leaf diffusive conductance in juvenile silver birch, Betula pendula. Trees (Berl.) 18, 686–695, 2004.
DOI: 10.1007/s00468-004-0353-8

Ueda Y., Siddique S., Frei M., A novel gene ozone-responsive apoplastic protein1 enhances cell death in ozone stress in rice. Plant Physiol 169(1):873–889, 2015.
DOI: 10.1104/pp.15.00956

UNECE Convention on Long-Range Transboundary Air Pollution (LRTAP), 2017. Chapter 3: Mapping critical levels for vegetation. LRTAP Convention Modelling and Mapping Manual. https://icpvegetation.ceh.ac.uk/, Last access: August 2024.

Vainonen J.P., Kangasjärvi J., Plant signalling in acute ozone exposure. Plant, cell & environment, 38(2), 240–252, 2015.
DOI: 10.1111/pce.12273

Vignudelli M., Gizzi P., Bollettino Fenologico. Alma Mater Studiorum Università di Bologna, 2017.

Vingarzan R., A Review of Surface Ozone Background Levels and Trends. Atmospheric Environment, 38, 3431-3442, 2004.
DOI: 10.1016/j.atmosenv.2004.03.030

Watanabe T., Izumi T., Matsuyama H., Accumulated phytotoxic ozone dose estimation for deciduous forest in Kanto, Japan in summer. Atmos. Environ. 176–185, 2016.
DOI: 10.1016/j.atmosenv.2016.01.016

Weiss A., Norman J.M., Partitioning solar radiation into direct and diffuse, visible and near-infrared components, Agricultural and Forest Meteorology, Volume 34, Issues 2–3, Pages 205-213, 1985.
DOI: 10.1016/0168-1923(85)90020-6

Wesely M.L., Parametrization of surface resistances to gaseous dry deposition in regional-scale numerical models. Atmos. Environ. 23, 1293–1304, 1989.
DOI: 10.1016/0004-6981(89)90153-4

Williams J.R., Jones C.A., Kiniry J.R., Spanel D.A., The EPIC Crop Growth Model. Transactions of the ASAE. Vol. 32 (2): 497-511, 1989.
https://doi.org/10.13031/2013.31032

Yendrek C.R., Koester R.P., Ainsworth E.A., A comparative analysis of transcriptomic, biochemical, and physiological responses to elevated ozone identifies species-specific mechanisms of resilience in legume crops, Journal of Experimental Botany, Volume 66, Issue 22, Pages 7101–7112, 2015.
DOI: 10.1093/jxb/erv404

Yeşilköy S., Bakanoğulları F., Şaylan L., Çaldağ B., Aslan T., Akataş N., Variation of albedo during the growing period of different winter wheat cultivars. Conference: 2nd International Conference/Symposium for Agriculture and Food 789–794, 2015.

Zadoks J. C., On the conceptual basis of crop loss assessment: the threshold theory. Annu. Rev. Phytopathol. 23: 455-473, 1985.
DOI: 10.1146/annurev.py.23.090185.002323

Zechmann B., Compartment-specific importance of ascorbate during environmental stress in plants. Antioxid Redox Sign 29(15):1488–1501, 2018.
DOI: 10.1089/ars.2017.7232

Zhang J., Tian H., Yang J., Pan S., Improving representation of crop growth and yield in the dynamic land ecosystem model and its application to China. J. Adv. Model. Earth Syst. 10, 1680–1707, 2018.
DOI: 10.1029/2017MS001253